UNIVERSITY OF OKLAHOMA

GRADUATE COLLEGE

A BOUNDING SURFACE MODEL FOR CYCLIC RESPONSE OF CEMENT-IMPROVED CLAYS

A DISSERTATION

SUBMITTED TO THE GRADUATE FACULTY

in partial fulfillment of the requirements for the

Degree of

DOCTOR OF PHILOSOPHY

By

ALLISON JUNE QUIROGA
Norman, Oklahoma
2018

A BOUNDING SURFACE MODEL FOR
CYCLIC RESPONSE OF CEMENT-IMPROVED CLAYS

A DISSERTATION APPROVED FOR THE
SCHOOL OF CIVIL ENGINEERING AND ENVIRONMENTAL SCIENCE

BY

_____
Dr. Kanthasamy Muraleetharan, Chair

_____
Dr. Amy Cerato

_____
Dr. Gerald Miller

_____
Dr. Naiyu Wang

_____
Dr. Victor Kaliakin

_____
Dr. Peter Attar

Acknowledgements

I would like to express my sincerest gratitude to Dr. Muraleetharan for his continued support and mentorship over the past eight years; and for his willingness to bring an unknown undergraduate into an ongoing research project. Dr. Muraleetharan's enthusiasm for working on novel problems in research and for teaching have always been inspiring and infectious.

I would also like to thank my committee members, Drs. Attar, Wang, Cerato, Miller, and Kaliakin. In particular, I would like to acknowledge the outstanding assistance Dr. Kaliakin provided in the completion of this research; and the years of guidance provided by Drs. Cerato and Miller, both in the laboratory and the classroom.

Additionally, I would like to acknowledge the assistance of all the current and former administrative staff in the Gallogly College of Engineering (GCoE) Dean's Office, School of Civil Engineering and Environmental Science (CEES), Graduate College, and GCoE Diversity & Inclusion Program and financial contributions made by the Terracon Foundation, ADSC-IAFD, Sid Richardson Memorial Fund, Hughes Centennial Fellowship program (funded through GCoE), Oklahoma Louis Stokes Alliance for Minority Participation Bridge to Doctorate Fellowhip program (funded through the National Science Foundation), and various other individual GCoE and CEES donors.

These acknowledgements would not be complete without an expression of my appreciation for unwavering support that has been offered by Josh Foster and my parents. Thank you for your patience, loving words of encouragement, and the innumerable big and little things you did to help me fulfill this goal.

Table of Contents

List of Tables

List of Figures

Abstract

The use of chemical stabilization of soft soils to achieve increased strength and decreased compressibility for subgrade and site improvement applications is a well-documented and accepted practice in geotechnical engineering. As use of cement mixing continues to grow in popularity and new applications are proposed, it is important for researchers and designers to have robust and reliable tools for the analysis and design of geotechnical systems utilizing this technology. The need for such tools becomes all the more important when the behavior of such systems has to be analyzed during seismic events. Computational modeling techniques (e.g., finite element or finite difference analysis programs) can be very useful in predicting the behavior of a proposed geotechnical system or structure under different loading conditions before its construction. However, the overall predictive capabilities of such tools are reliant on the algorithms which calculate the stress-strain responses of the individual elements of the model; i.e., the constitutive models.

This research details a bounding surface elastoplastic constitutive model which accounts for the effects of cementation through soil sensitivity and size and aspect ratio of the bounding surface. Destructuring of stabilized soil structure is tracked as a function of volumetric and deviatoric plastic strain accumulation. In order to predict plastic strain accumulation due to unloading and reloading/load-reversal events, the bounding surface concept is extended to incorporate a relocating projection center. Model predictions are compared with consolidation and conventional drained and undrained triaxial compression test results to demonstrate the predictive capability of the model for monotonic loading. A forecast of an undrained, stress-controlled, two-

way cyclic shear triaxial test is shown to demonstrate the model's ability to capture stress-strain phenomena associated with structure degradation due cyclic loading. The proposed model is able to adequately capture the general stress-strain behavior of normally consolidated and lightly overconsolidated soils in post-yield, under drained and undrained compression loading. Suggestions are made to improve the model predictions for soils in pre-yield and soils undergoing large strains. These suggestions include better methods for characterizing the initial sensitivity and its evolution and introducing a non-associative flow rule.

Chapter 1: Introduction

Geotechnical engineers are often faced with the challenge of working on sites with soft or marginal soils. As a result, many design methodologies for negating the soil's undesirable characteristics have been devised: loose soils may be compacted to a more desirable density; highly compressible soils may be pre-consolidated prior to construction; swelling soils may be isolated from sources of moisture or have moisture control implemented as part of the final design; and soft soils may be strengthened through use of chemical admixtures. Cement-improvement, i.e., chemical stabilization using cement as the bonding agent, is being used in a wide array of applications including subgrade strengthening, site remediation, excavation support, bridge abutment and embankment support, hydraulic cutoff, and deep foundation strengthening against lateral loading both on and offshore. This technology may also be used in remediation of existing structures through jet grouting.

As use of cement mixing continues to grow in popularity and novel applications are proposed, it is important for researchers and designers to have robust and reliable tools for the analysis and design of geotechnical systems utilizing this technology. The need for such tools becomes all the more important when the behavior of such systems has to be analyzed during seismic events. The behavior of natural soils and soil-structure interaction under dynamic loading are complex problems in and of themselves, so additional variables introduced by the inclusion of cement-mixed soils can make the design of such systems all the more complicated. Computational modeling techniques, e.g. finite element or finite difference analysis programs, can be very useful in predicting the behavior of a proposed geotechnical system or structure under different

loading conditions before its construction. However, the overall predictive capabilities of such tools is reliant on the algorithms which calculate the stress-strain response of the individual elements of the model; i.e., the constitutive models.

1.1 Motivation

A number of constitutive models have been proposed to describe the stress-strain behavior of artificially cemented clayey soils. Most of these models have been formulated for soils mixed with small amounts of cement additives (Xiao et al. 2016), and none have been specifically formulated to predict the behavior of cement-admixed clays subjected to cyclic loading. An essential aspect of cyclic modeling is the prediction of plastic strains during non-virgin loading (i.e., unloading and reloading/load-reversal). Most of the models proposed in the literature have the ability to predict plastic strains during reloading events, but none account for plastic strains during unloading or load-reversal events. This capability is crucial because:

- Cement-admixed clays do not behave elastically during unloading/load-reversal; the magnitude of pore water pressure and strain accumulation due to variable loading/unloading/load-reversal cycles which occur during seismic events will thus be best predicted if unloading/load-reversal is represented as an elastoplastic process, and
- Many researchers have characterized degradation of cemented-soil structure as a strain-dependent process. Predicting plastic strain accumulation during unloading/load-reversal events should allow better characterization of soil destructuring during cyclic loading.

1.2 Organization of dissertation

This dissertation is organized by chapters. A review of the literature pertaining to the stress-strain behavior of saturated clays under cyclic loading and cement-improved cohesive soils under both monotonic and cyclic loading is provided in Chapter 2. A discussion of the constitutive models formulated to predict the behavior of these soils will also be presented in Chapter 2. Chapter 3 puts forth the formulation of the proposed constitutive model, including the basic formulation of traditional plasticity and the bounding surface concept. A discussion of the implementation of the proposed model into a computer code is included in Chapter 4. A guide for the determination of the required model parameters, and sensitivity analysis of the parameters, is presented in Chapter 5. The proposed model is validated by comparing test results with model predictions in Chapter 6. Finally, conclusions and recommendations are provided in Chapter 7.

Chapter 2: Literature review

Before entering into a discussion of pertinent constitutive models currently available in the literature, it is appropriate to examine the stress-strain behaviors exhibited by cement-mixed clays and saturated clays under cyclic loading. Results of cyclic shear testing on cement-mixed, or artificially chemically improved, clays are of limited availability in the literature; however, some effort will be made to discuss important features observed in the limited dataset. A discussion of models formulated to predict the stress-strain behavior of naturally bonded/structured clays, soft rocks, and cyclically loaded clays will follow.

2.1 Overview of behavior of interest

2.1.1 Cyclic shearing of saturated clays

The stress-strain response of cyclically loaded cohesive soils is a subject which has been studied since the 1960's (Larew and Leonards 1962). The body of knowledge is quite extensive; interested readers should refer to the research report by Nieto Leal and Kaliakin (2013) for a comprehensive review of the seminal works on the subject. In their research, Nieto Leal and Kaliakin (2013; 2016) identify the following as some of the main features of the cyclic response of cohesive soils:

- A "cyclic threshold" stress or strain exists which can predict if a specimen will quickly reach an equilibrium state (characterized by no increase in inelastic strains, stiffness degradation, and excess pore water pressure [PWP] generation) or will experience large strains before reaching the equilibrium state or failure. This threshold is approximately 2/3 of the failure strength of the specimen in a

monotonic load test, but can be influenced by specimen properties such as overconsolidation ratio (OCR).

- For normally consolidated specimens, the generation of excess PWP causes a decrease in effective stresses during loading, which can be interpreted as an apparent overconsolidation.
- The rate and magnitude of strength and stiffness degradation of the specimen is dependent on the stress (or strain) levels, frequency of loading, and OCR.
- Excess PWP and inelastic strains develop more rapidly under two-way loading than for one-way (non-reversal) loading.
- There is a strong correlation between the generation of excess PWP and the relationship between the cyclic deviatoric stress (q_{cyclic}) and the threshold deviatoric stress ($q_{threshold}$), as depicted in Figure 2.1-1.
    - When q_{cyclic} falls under the threshold, the excess PWP strictly increases during loading and decreases during unloading (not shown).
    - If the q_{cyclic} exceeds the threshold by a relatively small amount, the excess PWP generation will increase during loading and decrease during unloading, but will not be of the same magnitude (see Figure 2.1-1a).
    - At an even higher value of q_{cyclic}, the excess PWP will initially decrease during unloading, but will ultimately increase before the beginning of the next loading increment (see Figure 2.1-1b).
    - For very high values of q_{cyclic}, the excess PWP will exhibit larger increases during unloading (see Figure 2.1-1c).

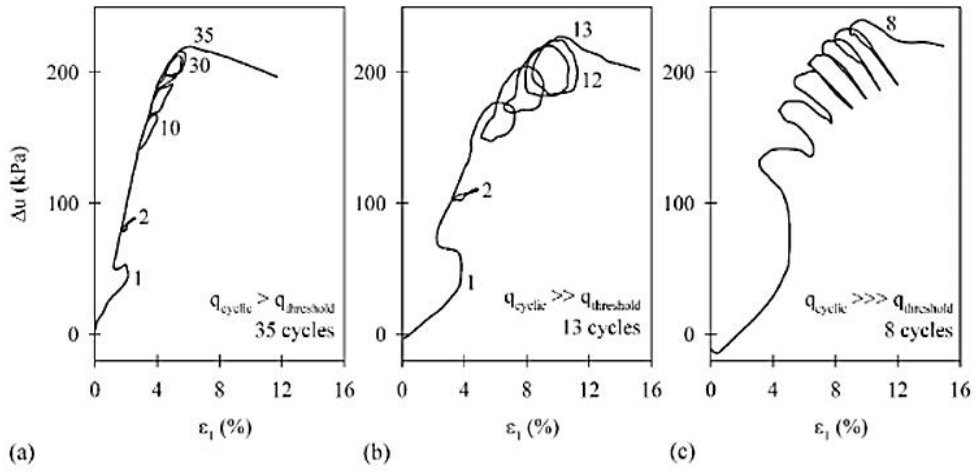

Figure 2.1-1: Strain-excess PWP curves for various cyclic deviatoric stresses in relation to threshold stress (Sheu 1984)

It is widely accepted that plastic deformations can occur during unloading phases of a cyclic loading test before the full reversal of the stress path. Although this is not explicitly outlined by Nieto-Leal and Kaliakin (2013), the above discussion of generation of excess PWP is inextricably related to the observed inelastic behavior. The consideration of plastic deformations during unloading phases is a key addition to the formulation of cyclic-loading specific models which will be discussed at length in Section 2.2.

2.1.2 Stress-strain behavior of cemented clays

Mixing cement into soil creates bonds between soil particles. Such bonds create an increase in shear strength and stiffness in the mixed specimens. But the differences in the stress-strain behavior are more nuanced and become more evident with increased bonding. The degree of bonding can allow a specimen to act similar to a naturally structured clay, a soft rock, or somewhere in between. The behavior of this geomaterial is, however, ruled by the strength and degradation of the cementitious bonds.

In consolidation tests, cement-mixing increases the yield stress and can affect the consolidation parameters. In Figure 2.1-2, the trend of increasing yield stress and increasing slope of the virgin compression line (λ) can be observed with increasing cement content. The virgin compression line of the cement-mixed soil may also exhibit nonlinearity, with the slope approaching the slope of the parent soil's virgin compression line. This has been considered evidence of the gradual destructuring, breaking of the cement bonds, during loading. Theoretically, the specimen will exhibit behavior similar to that of the parent clay after complete destructuring.

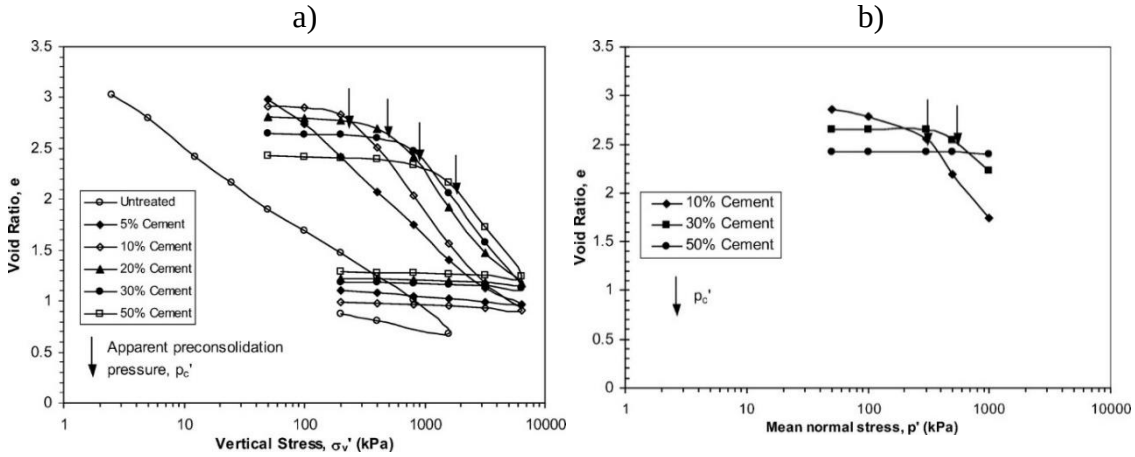

Figure 2.1-2: Effect of cementation on (a) oedometer and (b) isotropic consolidation results (Kamruzzaman et al. 2009)

Because of the increase in yield stress associated with cement-mixing, these soils are often said to have an "artificial" stress history. The concept of artificial stress history also has implications in monotonic shear results. Cemented clay specimens which have been created in the laboratory, and therefore have no stress history, will exhibit dilation and peak/residual behavior associated with overconsolidated clays at relatively low confining stresses; however, identical specimens will exhibit a lesser tendency toward dilation behavior at higher confining stresses. These effects can be

observed in both undrained and drained triaxial compression tests as shown in Figure 2.1-3, Figure 2.1-4, and Figure 2.1-5.

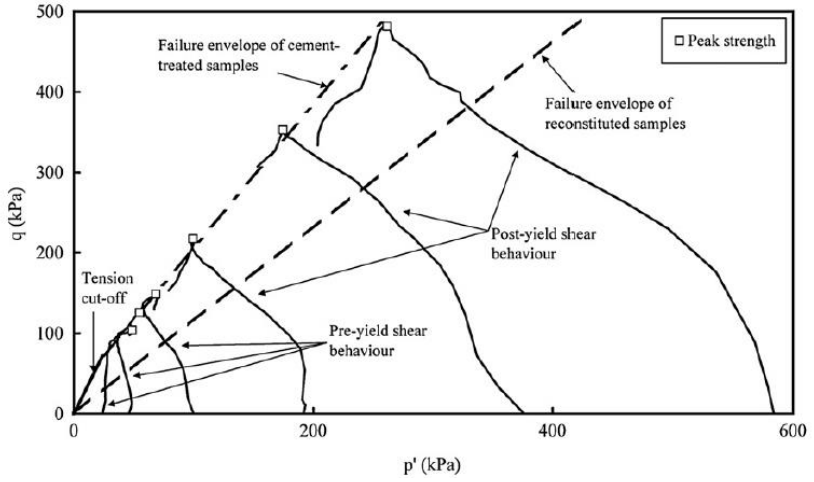

Figure 2.1-3: Effective stress path results from CIUC tests on cement-improved clay samples (Chiu et al. 2009)

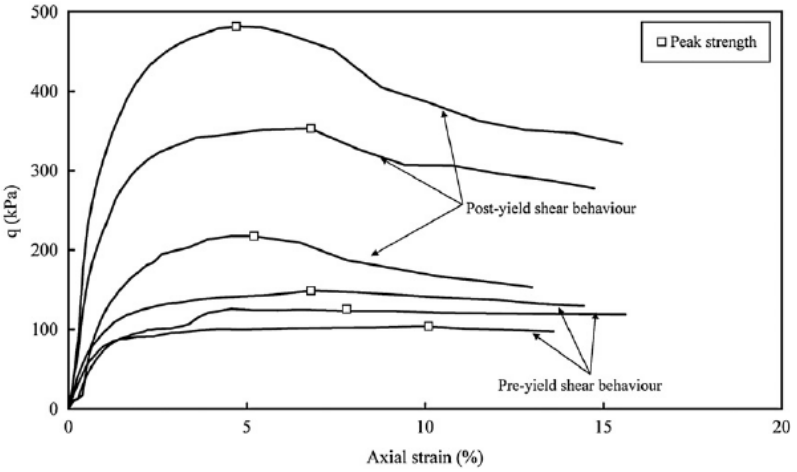

Figure 2.1-4: CIUC test results on cemented-improved clay specimens with varying confining pressures (Chiu et al. 2009)

It is notable that the peak/residual strength behavior is evident in most of the results and becomes more prominent as the confining stresses increase. This decrease in strength has been taken by many researchers as evidence of breakdown of the cementitious bonds within the sample during loading. The terms ‘pre-yield shear behavior’ and ‘post-yield shear behavior’ used to categorize testing results in

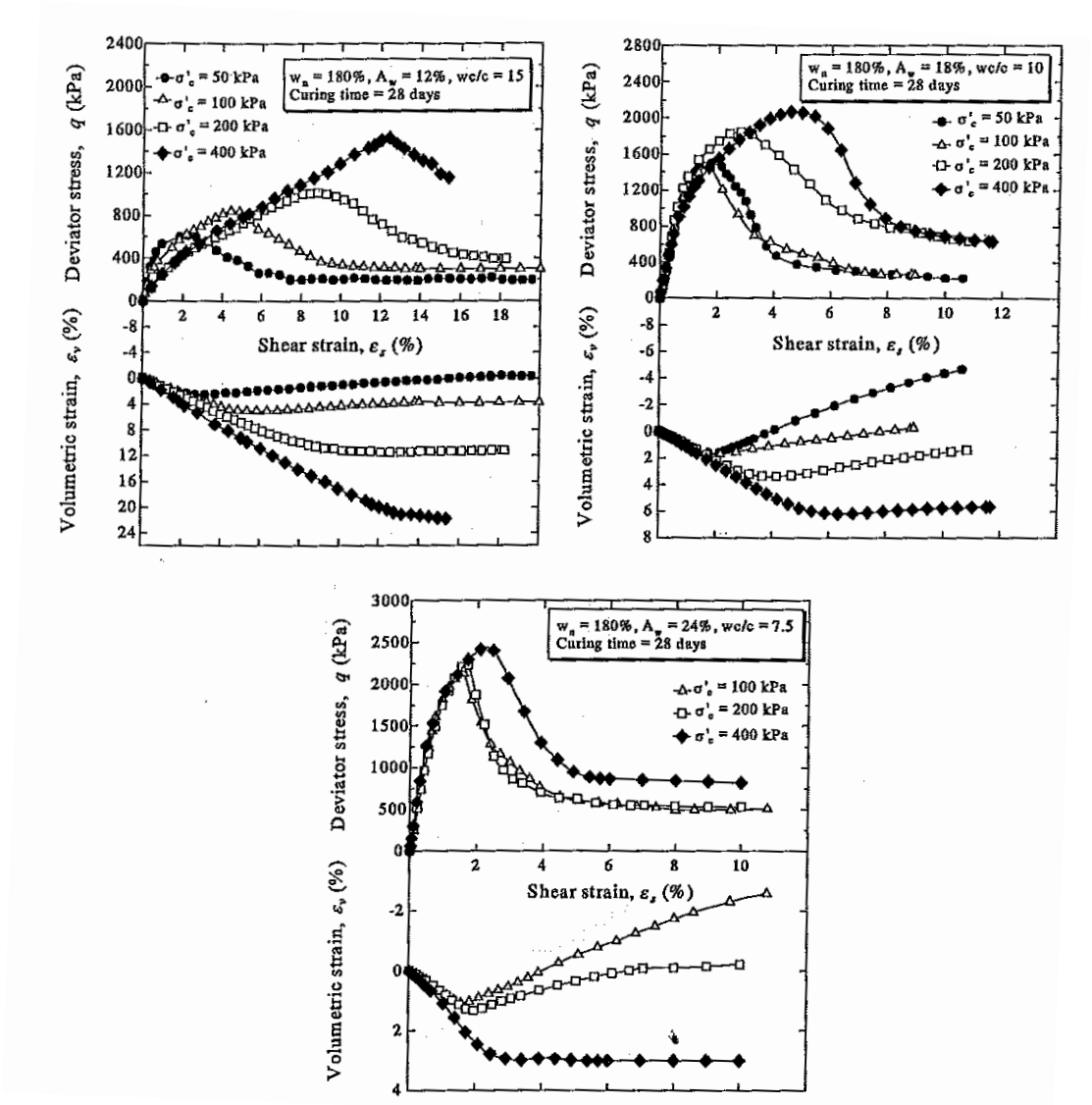

Figure 2.1-5: CIDC test results with varying cement content, total water to cement ratio, and confining stress (Miura et al. 2001)

Figure 2.1-3 and Figure 2.1-4 indicate the important role the imposed stresses will have in the degree of destructuring; if the stresses imposed are low in comparison to the strength of the cementitious bonds, very little destructuring will occur within the specimen. This relationship can also be noted in the deviatoric stress (q) – strain (ε) shown in Figure 2.1-5. The results for specimens with cement content, A_w = 12%, clearly show the influence of the confining pressure: the specimens with smaller confining pressures exhibit their peak strength at smaller strains (i.e., they act more like a brittle material). Decreased brittleness can be explained by the increased destructuring that results from the increased confining pressure. One may also note that the influence of confining pressure decreases with increased bonding/bond strength.

Much of the published literature on the cyclic behavior of cement-improved cohesive soils has focused on pavement applications, where the imposed stresses are generally very small (Abu-Farsakh et al. 2015; Ardah et al. 2017; da Fonseca et al. 2013; Panico and da Fonseca 2016). Such studies focused on the accumulation of permanent strains and evolution of shear stiffness with increasing load cycles. Figure 2.1-6 shows the results of a series of drained cyclic triaxial loading tests on unimproved and improved specimens with 3, 5, and 7% cement contents (Panico and da Fonseca 2016). In order to remain in the elastic zone, the axial load imposed was cycled between 10 and 20% of the ultimate deviatoric stress of the specimen type. Figure 2.1-6a and Figure 2.1-6b show that, for cemented specimens, a threshold exists after which the rate of axial strain accumulation increases dramatically, indicating a loss of structure in the specimens. Additionally, Figure 2.1-6c and Figure 2.1-6d show that the cemented specimens exhibit dilation, similar to the behavior of overconsolidated clays, after

reaching the threshold; the observation of dilation behavior reinforces the concept of cement-improvement causing an artificial stress history. Figure 2.1-7 shows the degradation of the secant shear modulus is related to the number of loading cycles and to the level of imposed deviatoric stresses (Sharma and Fahey 2003). Arrows in Figure 2.1-7a indicate a deviatoric yield stress, separating zones of almost-constant and rapidly decreasing shear stiffness. Sharma and Fahey (2003) note that with increasing numbers of cycles, this yield stress becomes more difficult to define. Subramaniam and Banerjee (2014) characterized the degradation of the shear modulus for cement-admixed soils tested at larger shear strain amplitudes.

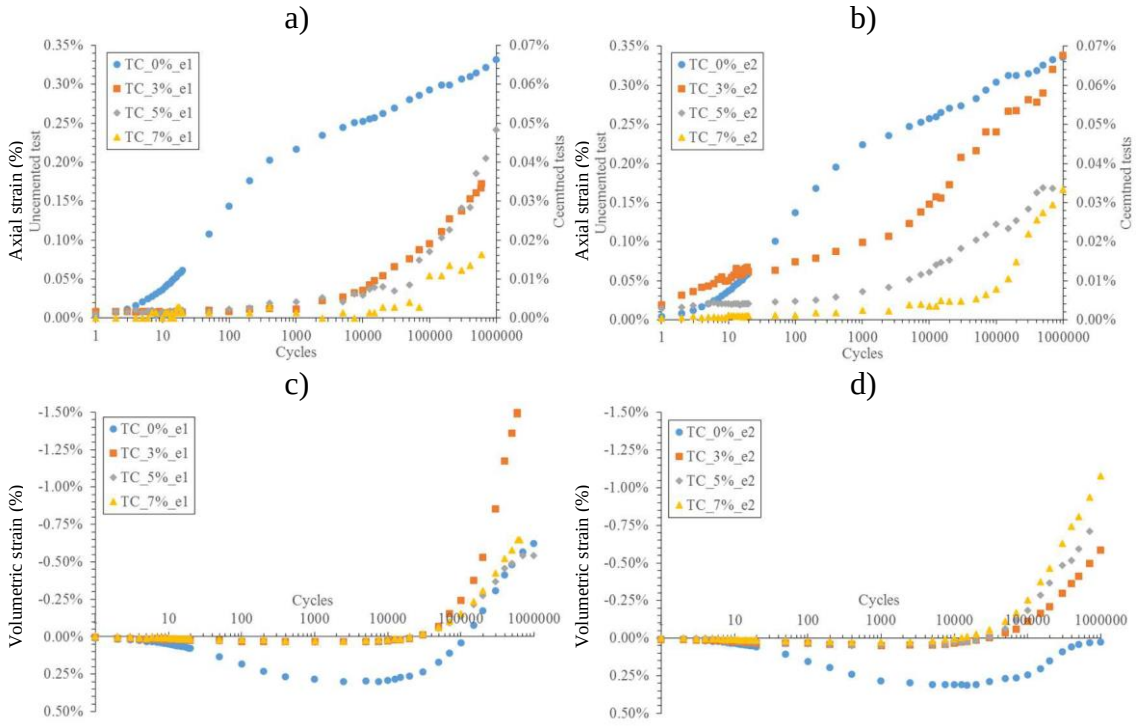

Figure 2.1-6: Evolution of the accumulated deformation with number of cycles (a) & (b) axial deformation, (c) & (d) volumetric deformation for samples with e_0 = 0.6 & 0.75, respectively (Panico and da Fonseca 2016)

Stress-strain behavior of an individual specimen has been shown to be influenced by a number of factors including: cement content, total water-to-cement ratio, initial void ratio, curing conditions and curing time (Miura et al. 2001). Although the behavior of a cement-mixed specimen cannot be characterized directly by the cement content, it will be prudent to describe the degree of cementation with a single value. A discussion of such a bond parameter, as well as other modeling techniques, will be discussed in Section 2.3.

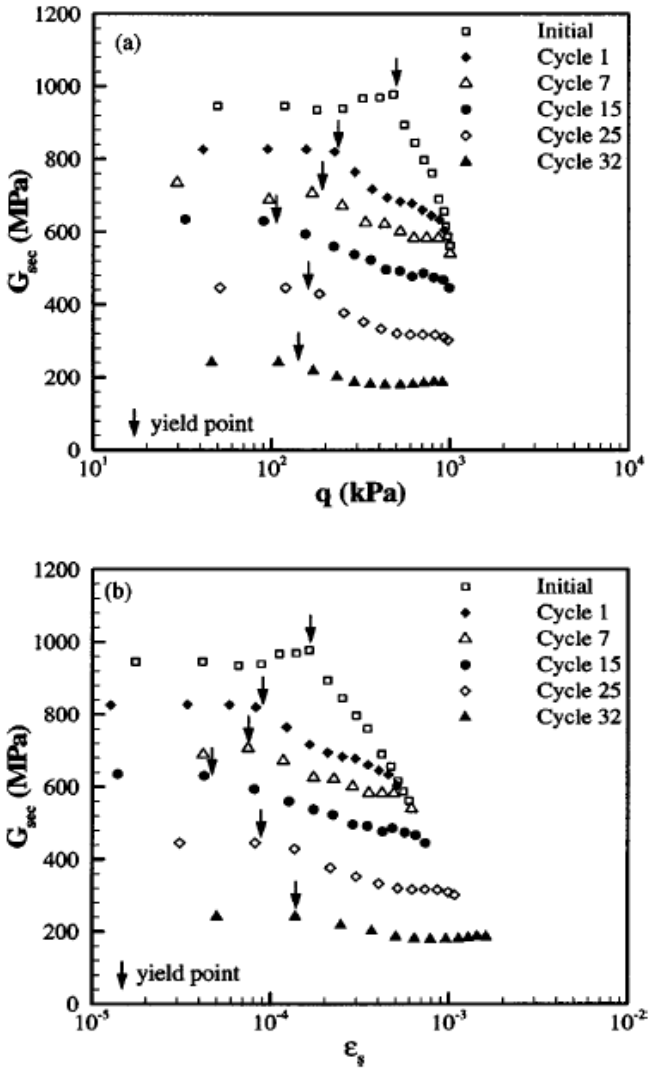

Figure 2.1-7: Variation of secant shear modulus with (a) deviatoric stress and (b) shear strain amplitude for various loading cycles (Sharma and Fahey 2003)

2.2 Models for cyclic shear loading of saturated clays

An essential aspect of cyclic modeling of cohesive soils is the prediction of plastic strains during non-virgin loading (i.e., during reloading and load-reversal). Many authors have noted that constitutive models which include multi-surface or bounding surface plasticity theories may provide adequate predictions of cyclic shear response through predicting plastic strains during reloading events. However, this is in fact the barest necessity in making such predictions (Cambou and Hicher 2010); a model should also be capable of predicting plastic strains during unloading events in order to be fully capable of predicting cyclic behavior. Some authors have sought to include this capability by proposing use of a distinct plastic modulus for virgin loading, unloading, and reloading stages (Hong et al. 2014; Wathugala and Desai 1993).

Another set of models created to describe the behavior of cyclically loaded materials implement variations on the Masing rule (Masing 1926). The original rule, formulated for one-dimensional loading, has been shown to be applicable to a great number of materials with few modifications (Montáns 2000). In fact, it has been shown that Mroz type multi-surface kinematic hardening models will ensure the Masing rule, including characteristic closed and stabilized hysteresis loops for the first or second loading cycle (Montáns 2000; Navarro et al. 2005).

Researchers have adopted the bounding surface plasticity theory on top of the Masing rule to address variable hardening during increased loading cycles. A number of constitutive models utilizing the extended Masing rule and bounding surface plasticity have been proposed to describe the behavior of cohesive soils under cyclic loads. This family of models is characterized by a translating projection center and bounding

surface which undergoes isotropic and kinematic hardening (Hu and Liu 2015; Li and Meissner 2002). Figure 2.2-1 demonstrates the evolution of the bounding and loading surfaces and relocation of the projection center, as formulated by Li and Meissner (2002). Figure 2.2-1a shows isotropic consolidation loading along the p'-axis with the projection center at the origin O. In Figure 2.2-1b, the projection center has translated to point x upon the change of direction of the total stress path (TSP). A loading surface (f_1) will undergo isotropic hardening during the current loading event, indicated by arrow XA. The bounding surface (F_1) and loading surface (f_1) are homologous and tangential at the projection center. When the TSP direction is changed at the end of the loading event, the projection center translates to point A, the point of the stress path reversal, as demonstrated in Figure 2.2-1c. In addition to the translation of the protection center, the bounding surface (F_1) undergoes kinematic hardening such that the new bounding surface (F_2) is now tangential to the loading surface (f_1) at A. Following the update of the bounding surface, the loading surface is replaced with a new loading surface (f_2) to describe the loading taking place during the current loading event, signified by arrow AB.

Relocation of the projection center for bounding surface models has also been adopted in the absence of kinematic hardening of the bounding surface. Seidalinov and Taiebat (2014) and Nieto Leal (2016), among others, present formulations which utilize rotational hardening of the bounding surface and a changing projection center to predict the induced anisotropy and hysteresis behavior of cyclically loaded clays. Noting the reliance of the bounding surface on Lode angle, Nieto Leal (2016) proposed an extended radial mapping scheme to ensure correctness of the Lode angle used to

determine the similarity ratio and image values of the stress invariants, when the projection center may not be located on the I-axis (in I-J space) or the origin of the π-plane. Additionally, Nieto Leal (2016) incorporated a degradation term into the shape hardening equation to emulate the decrease in soil stiffness under increasing number of loading cycles.

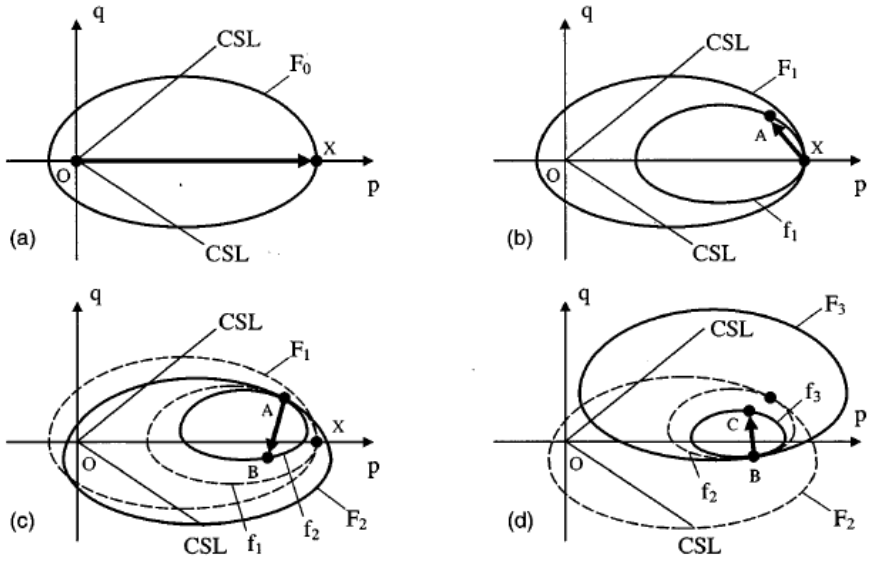

Figure 2.2-1: "Movement of bounding and loading surfaces in stress space: (a) virgin loading, (b), (c), and (d) non-virgin loading" (Li and Meissner 2002)

2.3 Elastoplastic models for bonded/structured geomaterials

A number of constitutive models for naturally structured, naturally bonded and artificially bonded cohesive geomaterials have been proposed by researchers. Many aim to modify existing models for remolded cohesive soils. Many of these new models account for increased strength, apparent cohesion, increased void ratios, and destructuring.

In many of these models the yield surface is assumed to have the same shape as that of the parent soil, but the size is increased to account for higher strength (Arroyo et

al. 2011; Arroyo et al. 2012; Asaoka et al. 2000; Horpibulsuk et al. 2010; Lee et al. 2004; Nova et al. 2003; Suebsuk et al. 2011; Yu et al. 2007). This increase in yield surface size is defined by the initial isotropic yield strength of the bonded specimen (i.e., p'_0 or I_o). Asaoka et al. (2000), Taiebat et al. (2010), and Baudet and Stallebrass (2004) account for the difference in size of the yield surface by employing a similarity ratio between the remolded and bonded surfaces (e.g., sensitivity, as discussed in Subsection 2.3.2); conversely, several other authors account for the influence of bonding on the size of the yield surface through a defined structure strength parameter, often defined on the positive p' axis (Arroyo et al. 2012; Horpibulsuk et al. 2010; Nguyen et al. 2014; Nova et al. 2003; Suebsuk et al. 2010; Suebsuk et al. 2011; Yu et al. 2007). One common method is to define a parameter, p'_c, which is the direct contribution of the structure to the isotropic compression strength as shown in Figure 2.3-1 (Yu et al. 2007).

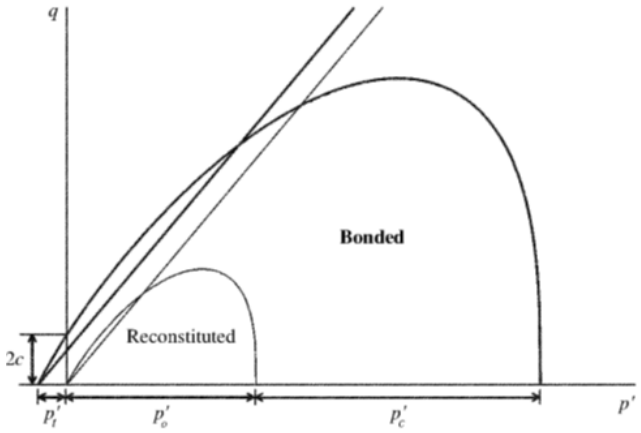

Figure 2.3-1: Yield surface proposed in Clay and Sand Model (Yu et al. 2007)

2.3.1 Yield and plastic potential surfaces

In general, the yield surface is translated to the left along the p' axis in order to simulate the tensile capacity created through cement mixing. Arroyo et al. (2011), Nova

et al. (2003), and Yu et al. (2007) define p'_t, the value of the bonded yield surface intercept in tension, as a decreasing function of the similarity ratio and p'_c, the difference between the bonded and reconstituted yield surface intercepts in compression as shown in Figure 2.3-1. Horpibulsuk et al. (2010), Suebsuk et al. (2010), and Suebsuk et al. (2011) define the translation of the yield surface with respect to the bonding cohesion parameter, C, which defines the intercept of the translated critical state line (CSL) with the q axis as shown in Figure 2.3-2. In order to account for this translation, the authors introduce a modified mean effective stress for structured clays:

$$\bar{p}' = p' + C/M \qquad \textbf{2.3-1}$$

In this family of models, the authors use $\bar{p}'$ in place of p' in the Modified Cam Clay yield surface function, which results in a tension zone in the initial yield surface and translation of the yield surface during loading. Notable exceptions to the trend to include tension zones within initial yield surfaces are Asaoka et al. (2000), who ostensibly do not account for cohesion, and Xiao et al. (2016), who account for cohesion in the formulation of the bounding surface equation.

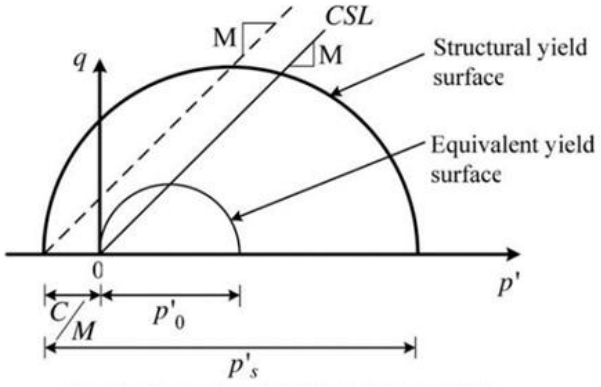

Figure 2.3-2: Yield surface proposed in Structured Cam Clay model (Horpibulsuk et al. 2010)

As previously stated, not all of the proposed models for structured/bonded soils utilize the same shape for the yield surface as used in similar models for remolded soils. Building upon the work of Suebsuk et al. (2010), Nguyen et al. (2014) and Nguyen et al. (2017) redefine modified mean effective stress in order to better fit the failure envelope of cemented clays observed in the literature. The authors contend that the failure envelope should account for destructuring due to the influence of mean effective stress, as shown in Figure 2.3-3. As such, the authors state that the modified mean effective stress should take the form:

$$\bar{p}' = p' + \frac{C\left(1+\frac{p_d'}{C+\beta}\right)\exp\left(\frac{-p_d'}{C+\beta}\right)}{M} \qquad \textbf{2.3-2}$$

where p'_d is the mean effective stress inducing degradation (i.e. crushing) of the cementitious bonds, and β is a fitted rate parameter. If this $\bar{p}'$ is used in place of p' in the Modified Cam Clay yield surface function, as proposed by Horpibulsuk et al. (2010), the yield surface will not retain its elliptical shape for C>0.

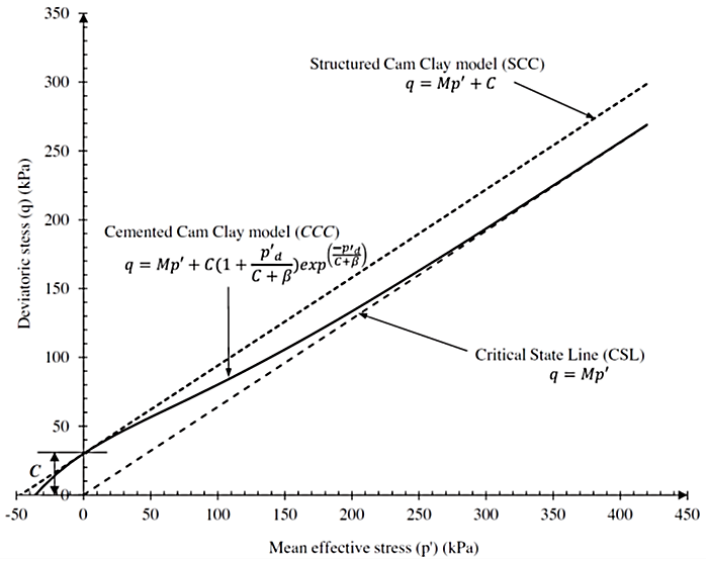

Figure 2.3-3: Failure envelope proposed in Cemented Cam Clay model (Nguyen et al. 2014)

Researchers such as Kasama et al. (2000) and Xiao et al. (2016) proposed yield surfaces formulated specifically to take the influence of bonding into account when defining the shape of the yield surface. The authors derive yield surfaces from a modified external energy equation. Kasama et al. (2000) propose the following relationship:

$$dW_{in} = \bar{p}'\sqrt{((d\nu^p)^2 + X d\nu^p d\varepsilon^p + (M d\varepsilon^p)^2)} - p'_r d\nu^p \quad \textbf{2.3-3}$$

in which $\bar{p'} = p' + p'_r$, where p_r' is a term signifying the additional strength due to bonds [similar to Nova et al. (2003), Horpibulsuk et al. (2010), and others discussed previously], and $X d\nu^p d\varepsilon^p$ is a generalized soil dilatancy coupling term, where

$$X = (c - 2)\eta^* \quad \textbf{2.3-4}$$

and c is a fitted parameter affecting the shape of the surface. The resulting yield function will be a pinched ellipse, whose shape and size are determined by the parameter c and the value of p'_r (the intercept on the negative p′ axis), respectively.

Xiao et al. (2016) stated that the degree and effect of cementation can be defined by the sensitivity, S, and the cohesion intercept of a Mohr-Coulomb failure surface, C. The authors proposed a "Mohr-Coulomb generalization" of the Modified Cam Clay flow rule, i.e.

$$dW_{in} = p' d\varepsilon_v^p + q d\varepsilon_s^p = \sqrt{\left(p' d\varepsilon_v^p\right)^2 + \left((C + Mp') d\varepsilon_s^p\right)^2} \quad \textbf{2.3-5}$$

to define the yield surface (associated flow rule is assumed). This formulation allows the shape of the yield surface (specifically, aspect ratio and cohesion intercept) to be directly affected by changes in the cohesion (bond) parameter. Figure 2.3-4 shows the evolution of the proposed yield surface due to isotropic compression. One will note that

as the cohesion intercept (C) decreases, the aspect ratio of yield surface in p'-q space decreases (i.e. the surface becomes wider in relation to its height).

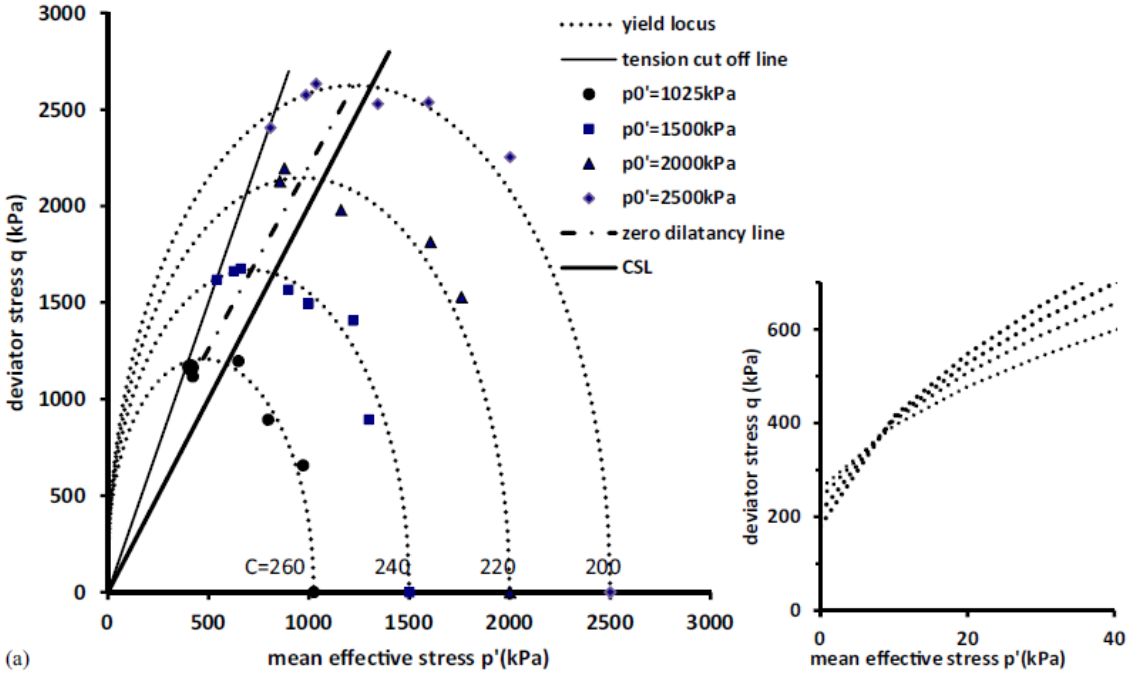

Figure 2.3-4: Evolution of the yield locus in p'- q space (Xiao et al. 2016)

Although allowing the shape (and/or aspect ratio) of the yield surface to change during loading is not a feature common to improved soil models, Xiao et al. (2016) are not the only authors to build such a capability into their formulations. In their modification of the SANICLAY model, Taiebat et al. (2010) define the slope of the critical state line (M) of the structured surface as a function of a structuration factor (S_f) and the final critical state line slope (M*); i.e.,

$$M = S_f M^* \qquad \textbf{2.3-6}$$

In the Sydney Soil Model, Liu et al. (2010) define M for a structured soil as:

$$M = \frac{M^*}{1 + \mu \ln(p'_s/p'_e)} \qquad \textbf{2.3-7}$$

where p'_s and p'_e represent the intercepts of the structured and reference yield surfaces with the positive p' axis, respectively; M* is the final (reference) state CSL slope; and μ

is a model parameter indicating the influence of soil structure on the shape of the yield surface.

Where Xiao et al. (2016) derived an expression for a plastic potential and then adopted an associative flow rule to determine the yield surface, some researchers implemented non-associative plastic potentials, also derived from the energy equation. Suebsuk et al. (2010) and Suebsuk et al. (2011) use the stress-dilatancy relationship introduced by McDowell and Hau (2003), and coincidentally the same expression used for X by Kasama et al. (2000). Therefore the yield surface of Kasama et al. (2000) is the same as the plastic potential of Suebsuk et al. (2010) and Suebsuk et al. (2011). Nguyen et al. (2014) introduce a new expression for the soil dilatancy coupling term (X) in the Kasama et al. (2000) generalized energy equation; i.e.,

$$X = \left(2\frac{\alpha + 1}{A} - 2\right)\eta^* \qquad \textbf{2.3-8}$$

$$A = 1 - \frac{p'_d C}{M(C + \beta)^2}\exp\left(\frac{-p'_d}{C + \beta}\right) \qquad \textbf{2.3-9}$$

One will note that this expression resembles the form of that used by Kasama et al. (2000), where $2\frac{\alpha+1}{A}$ stands in for the shape parameter c in Equation 2.3-4. α is coupling parameter and one may recall that C, β, and p'_d are parameters associated with the influence and degradation of cementation. Nguyen et al. (2017) further modify the X term in the Kasama et al. (2000) generalized energy equation to relate the size of the yield surface (via p'_0) to the effects of cement-improvement (represented by the second half of Equation 2.3-2). In order to create a model appropriate for artificially cemented sands and clays, Yu et al. (2007) propose a modified flow rule derived from minimum energy considerations for particle sliding (Rowe 1963; Rowe 1962), based on the

critical state friction angle and cohesion intercept. The cohesion intercept is assumed to decrease with increasing degradation, hence changing the shape of the surface during loading.

2.3.2 Destructuring and its implications on isotropic compression curves

With structure diminishing during loading, the isotropic compression curve cannot be assumed bilinear in void ratio (or specific volume) vs. $\ln(p')$ space. Defining the structured compression line (SCL) is, therefore, another important modeling consideration in the formulation of constitutive models for structured geomaterials. In the simplest case, Lee et al. (2004) define the SCL as a third order polynomial, $e(p')$, calibrated to fit experimental data. Liu and Carter (2000) introduced the hypothesis that the SCL was equivalent to the intrinsic compression line (ICL) plus additional void ratio due to structure for any mean effective stress:

$$e = e^* + \Delta e_i \left(\frac{p'_{y,i}}{p'}\right)^b, \text{ when } p' \geq p'_{y,i} \qquad \textbf{2.3-10}$$

where e^*, Δe_i, and $p'_{y,i}$ are defined graphically in Figure 2.3-5, and b is a rate variable. This method has been used in the constitutive models by Liu et al. (2006), Horpibulsuk et al. (2010), Suebsuk et al. (2010), and Suebsuk et al. (2011). Rouainia and Muir Wood (2000), Baudet and Stallebrass (2004), and Xiao et al. (2016) define the SCL in relation to the ICL and current degree of structure, such that:

$$p' = rp'_{ref} \qquad \textbf{2.3-11}$$

for a given specific volume, where p' is the mean effective stress on the SCL, and the p'_{ref} is the corresponding stress on the ICL. Baudet and Stallebrass (2004) and Xiao et al. (2016) utilize Cotecchia and Chandler's sensitivity framework (2000), for which the parameter r in Equation 2.3-11 is replaced by sensitivity, the ratio of the mean effective

stresses (p′) corresponding to equivalent specific volumes (v) on the isotropic compression curves of intact and fully remolded cement-mixed clays (i.e. $S = \frac{p'_0}{p'_{0u}}$), shown in Figure 2.3-6.

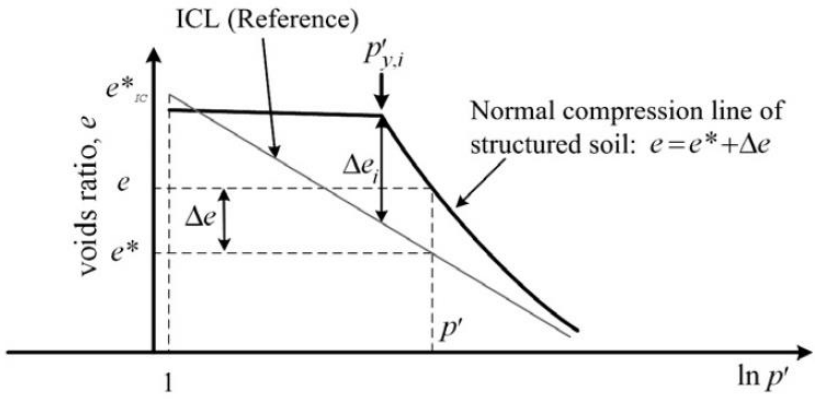

Figure 2.3-5: Structured Compression Line (SCL) proposed by Liu and Carter (2000)

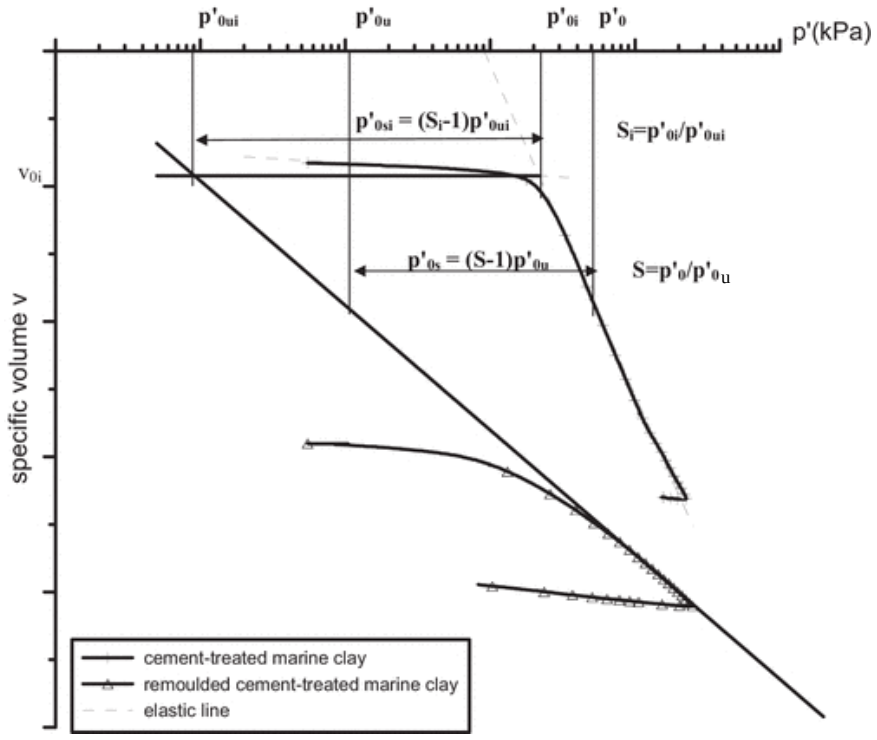

Figure 2.3-6: Determination of sensitivity from isotropic compression curves of cement-mixed clay in intact and remolded states (Xiao et al. 2016)

Representing the decrease in structure during loading is important for capturing the softening behavior exhibited by cemented clays. Many researchers model the decrease in structure as an exponential function of some damage variable. Asaoka et al. (2000), Lee et al. (2004), Suebsuk et al. (2010), and Suebsuk et al. (2011) define the damage variable as a function of the plastic deviatoric strain; Baudet and Stallebrass (2004), Arroyo et al. (2012), Nova et al. (2003), Yu et al. (2007), and Taiebat et al. (2010) define the damage variable as a combination of plastic deviatoric and volumetric strain. Alternatively, Liu et al. (2006), Horpibulsuk et al. (2010), and Nguyen et al. (2014) propose that degradation of the structure is an exponential function of mean effective stress. These formulations assume that crushing of the inter-particle bonds is the predominant mechanism of destructuring. Liu et al. (2006) and Horpibulsuk et al. (2010) only calculate the effect of crushing when the stress point is on the critical state line, but the specimen has not reached critical state (i.e., the modified effective stress state travels up or down the critical state line). This crushing is built directly into the shape of the failure envelope of the Nguyen et al. (2014) model. Nguyen et al. (2017) built upon the earlier work of Nguyen et al. (2014) by stating that the effect of cementation, noted as the second term in Equation 2.3-2, will degrade with increasing plastic deviatoric strain, as discussed above. Xiao et al. (2016) state that destructuring is caused by work done against the cement structure during plastic loading. The derivation of the degradation-work relationship relies on the common assumption that the load carried by the cementitious bonds is the total load minus the strength of the parent soil at the same specific volume, again building off of the sensitivity framework of Cotecchia and Chandler (2000). The resulting degradation equation takes the form:

$$dS = \frac{-\alpha \upsilon S}{p'_0}\left\{p' d\varepsilon_v^p + q d\varepsilon_s^p - \sqrt{\left(p'_u d\varepsilon_v^p\right)^2 + \left(M p'_u d\varepsilon_s^p\right)^2}\right\} \quad \textbf{2.3-12}$$

where p'_u is the mean effective stress on the corresponding unstructured soil yield surface, S is the sensitivity, and α is a rate parameter. This formulation can account for the crushing caused by large confining stresses, while also incorporating the damage caused by deviatoric strains, which may be left out for stress paths with little change in p′.

2.3.3 Artificial stress history and accumulated plastic strain

As discussed in Subsection 2.1.2, the cement mixing process creates an artificial stress history within the specimen due to the strength of the bonds. Many authors recognize that cement improved specimens develop plastic strains during loading, even while the stress point is inside the yield surface. Some authors have applied multi-surface plasticity (Baudet and Stallebrass 2004) and bounding surface plasticity (González et al. 2011; Rouainia and Muir Wood 2000; Suebsuk et al. 2011; Xiao et al. 2016) to better predict the stress-strain behavior of specimens at relatively low confining stresses.

2.4 Other models for bonded/structured geomaterials

2.4.1 Micromechanical models

Micromechanical models, described by the Discrete Element Method (DEM), are a popular way of describing the interactions of granular materials. At their most basic form, these models take local forces and movements and translate them into stresses and strains on both the local and macro-scale levels through the energy balance principle. Recently, Discrete Element Methods have been used to study bonded materials. Such models idealize the contributions of inter-particle bonding with varying

complexity. A recent model by Obermayr et al. (2013) describe such bonds as Timoshenko beam elements connecting the centers of individual sand particles. A simpler formulation, the NS2D model proposed by Jiang et al. (2007), states that bonded contacts can carry tensile forces, as well as higher normal and shear stresses in compression than unbonded contacts. Once bond strengths are exceeded, the contacts are considered unbonded and classical friction laws are reinstated for model calculations.

Zhang et al. (2013) propose a micromechanically informed model for cement mixed clay. Cementation in the specimen is represented by additional inter-cluster bonding, characterized by additional cohesion in shear sliding and higher strength in normal compression. The yield surface, hardening function, and stress/dilatancy equation are defined with respect to the inter-cluster cohesion and inter-cluster friction angle, which decrease with damage accumulated during loading.

2.4.2 Disturbed state concept models

Desai and Toth (1996) described a bonded soil system as a combination of the behaviors of two reference states: the relatively intact and fully adjusted states, corresponding to bonded and remolded states, respectively. The overall incremental stress is a linear combination of the incremental stress of each of the reference states. The reference states may be described by any appropriate model (e.g., linear elastic or elastoplastic). The contribution of each reference state to the overall behavior is controlled by the disturbance variable, D, which is a function of the direction of the plastic deviatoric strain increment. Similarly, Vatsala et al. (2001) described a bonded system as having two parts: the soil skeleton and cementitious bonds. The stiffness

matrices of each system are added to find the stiffness matrix of the combined system. Vatsala et al. (2001) propose an elastoplastic formulation with a square shaped yield surface in q-p' space and associated flow rule for the bonds and use the Modified Cam Clay model to describe the stress-strain relationships of the unbonded soil skeleton.

Liu et al. (2016) proposed a binary-medium disturbed state model in which the bonded (i.e. intact) and remolded elements are modeled as a brittle bond and a frictional plastic slider, respectively. The elastic portions of both element types are modeled as springs. The incremental stress-strain behavior of the element is a combination of the bonded and frictional element behaviors, dictated by the homogenization theory and disturbed state concept. Ouria (2017) uses the disturbed state concept to characterize the virgin compression behavior (λ) of structured soils as a combination of the initially structured (λ_{RI}) and fully remolded (λ_{FA}) states where the value of the disturbance variable is controlled by the ratio of the current and yield mean effective stresses. Ouria (2017) proposes a hybrid disturbed state concept and elastoplastic model by integrating the formulation for λ into the Modified Cam Clay model (Roscoe and Burland 1968).

2.5 Damage models for quasi-brittle geomaterials

The stress-strain behavior of quasi-brittle geomaterials (e.g., some types of rock, concrete, etc.) is related to the creation of micro- and meso-cracks, opening and closing of these cracks, and frictional sliding between the crack surfaces. Damage models, based on thermodynamic formulations, have been proposed by many authors, including Halm and Dragon (1998), Desmorat et al. (2007), and Lanoye et al. (2013). Anisotropy and frictional sliding are not always factored into the formulation of such damage models, but are required to provide good approximations of behavior under complex

loading paths, such as torsion (Lanoye et al. 2013). In isotropic models, and some anisotropic models, the damage is denoted by a scalar parameter (Desmorat et al. 2007; Lanoye et al. 2013). In the Halm and Dragon (1998) family of models, anisotropic damage is tracked as a second-order tensor which can be represented more simply as a set of three positive eigenvalues and three orthogonal eigenvectors. As micro-cracks are opened during loading, the Young's and shear moduli are decreased. The uniaxial effect, considered by Halm and Dragon (1998) and Lanoye et al. (2013), describes the recovery of these moduli when the appropriate micro-cracks are closed during loading. Accounting for such behavior results in better approximations of loading/unloading cycles.

Chapter 3: Model formulation

Constitutive modeling of cyclic loading of cohesive soils and monotonic loading of cement-mixed cohesive soils have been very thoroughly researched independently. However, few models have been developed to address cyclic loading of cement-mixed cohesive soils. Degradation of cementitious bonds has been documented to be a result of both crushing due to confining stress and accumulated plastic strain during shear. Xiao et al. (2016) proposed a straightforward formulation which harnesses the effects of cementation through parameters that are directly observable in their initial states; i.e., sensitivity and the cohesion intercept. The model of Xiao et al. (2016) is used as a starting point for the formulation of a new single-surface bounding surface model based on the concepts put forth by Dafalias (1986), Dafalias and Herrmann (1986), and Kaliakin and Dafalias (1989). However, the Xiao et al. (2016) formulation has several weaknesses which will make it difficult to implement into a finite element program, namely: a) the formulation relies on triaxial stress invariants, and b) the bounding surface (see Figure 2.3-4) is not a continuous closed surface. In order to rectify these shortcomings and extend the model to incorporate the bounding surface concept with radial mapping rule (Dafalias 1986), an earlier iteration of the proposed model attempted to emulate the non-elliptical, cohesion intercept defined Xiao et al. (2016) bounding surface with a single-ellipse, Lode angle dependent, surface defined through a generalized cohesion intercept. This initial formulation exhibited significant predictive shortcomings, especially when the soil approaches the fully remolded state (i.e., $S \approx 1$). The final form of the proposed model utilizes a single-ellipse surface (Kaliakin and Dafalias 1989) with a modification to allow the aspect ratio (relationship of height:

width) of the surface to vary as a function of soil structure. In outlining the proposed model, the formulation for elastoplastic theory in general stress invariant space will first be presented. Then the formulation of the Xiao et al. (2016) model will be presented along with its generalization to dependence on the direct stress invariants I, J, and Lode angle (θ). The full formulation of the proposed model will be discussed in Section 3.5 and the Nieto Leal (2016) projection center relocation procedure, including Lode angle correction, adopted herein will be discussed in Subsection 3.5.4

3.1 Definitions of stress and strain invariants

Before putting forth a discussion of the theories underlying the existing and proposed models, it is necessary to define the stress and strain invariants which will be used. Triaxial stress invariants, the mean effective stress (p′) and deviatoric stress (q), are defined as:

$$p' = \frac{\sigma'_1 + 2\sigma'_3}{3} = \frac{\sigma'_{11} + \sigma'_{22} + \sigma'_{33}}{3} = \frac{\delta_{ij}\sigma'_{ij}}{3} \quad \textbf{3.1-1}$$

$$q = \sigma'_1 - \sigma'_3 = \left(3/2\, s_{ij}s_{ij}\right)^{1/2} \quad \textbf{3.1-2}$$

where δ_{ij} is the Kronecker delta and s_{ij} is the deviatoric stress tensor.

The direct stress invariants are defined, and related to the triaxial stress invariants, by:

$$I = \delta_{ij}\sigma'_{ij} = 3p' \quad \textbf{3.1-3}$$

$$J = \left(1/2\, s_{ij}s_{ij}\right)^{1/2};\ J^2 = \frac{q^2}{3} \quad \textbf{3.1-4}$$

$$T = \left(1/3\, s_{ij}s_{jk}s_{ki}\right)^{1/3} \quad \textbf{3.1-5}$$

$$\frac{-\pi}{6} \le \theta = \frac{1}{3}\sin^{-1}\left[\frac{3\sqrt{3}}{2}\left(\frac{T}{J}\right)^3\right] \le \frac{\pi}{6} \quad \textbf{3.1-6}$$

The stress gradients of the direct stress invariants are:

$$\frac{\partial \mathrm{I}}{\partial \sigma_{ij}} = \delta_{ij} \qquad \textbf{3.1-7}$$

$$\frac{\partial \mathrm{J}}{\partial \sigma_{ij}} = \frac{s_{ij}}{2\mathrm{J}} \qquad \textbf{3.1-8}$$

$$\frac{\partial \theta}{\partial \sigma_{ij}} = \frac{\sqrt{3}}{2\mathrm{J}\cos 3\theta}\left[\frac{s_{ik}s_{kj}}{\mathrm{J}^2} - 3\left(\frac{T}{\mathrm{J}}\right)^3 \frac{s_{ij}}{2\mathrm{J}} - \frac{2}{3}\delta_{ij}\right] \qquad \textbf{3.1-9}$$

Assuming infinitesimal strains, the strain tensor invariants, volumentric (ε_v) and deviatoric (ε_s) strain, are defined as:

$$\varepsilon_v = \varepsilon_{11} + \varepsilon_{22} + \varepsilon_{33} = \delta_{ij}\varepsilon_{ij} \qquad \textbf{3.1-10}$$

$$\varepsilon_s = {}^{2}/_{3}\,(\varepsilon_1 - \varepsilon_3) = \left({}^{2}/_{3}\, e_{ij}e_{ij}\right)^{1/2} \qquad \textbf{3.1-11}$$

where e_{ij} is the deviatoric strain tensor.

3.2 General formulation of plasticity in direct stress invariant space

The proposed model is built upon the general rate independent elastoplasticity framework utilizing the bounding surface and radial mapping concepts for isotropic materials, as outlined by Dafalias (1986) and Dafalias and Herrmann (1986). The bounding surface concept is an extension of traditional plasticity, therefore it is necessary to cover the basics of plasticity before moving on to a discussion of the bounding surface concept (Dafalias 1986).

The general, rate-independent elastoplasticity formulation is characterized by a yield surface in stress space defined by

$$f(\sigma_{ij},\, q_n) = 0 \qquad \textbf{3.2-1}$$

where q_n indicates the set of plastic internal variables. The total strain rate is taken as the sum of elastic and plastic parts, following the form:

$$\dot{\varepsilon}_{ij} = \dot{\varepsilon}^{e}_{ij} + \dot{\varepsilon}^{p}_{ij} \quad \textbf{3.2-2}$$

where the e and p superscripts designate elastic and plastic portions, respectively, and the superposed dot designates a material time derivative or rate. The elastic, plastic, and total strain rates are related to the stress rate, σ_{ij}, by the following (Dafalias and Herrmann 1986):

$$\dot{\varepsilon}^{e}_{ij} = C_{ijkl}\dot{\sigma}_{kl} \; ; \; \dot{\sigma}_{ij} = E_{ijkl}\dot{\varepsilon}^{e}_{kl} \quad \textbf{3.2-3}$$

$$\dot{\varepsilon}^{p}_{ij} = \langle L \rangle R_{ij} \quad \textbf{3.2-4}$$

$$\dot{q}_{n} = \langle L \rangle r_{n} \quad \textbf{3.2-5}$$

$$\dot{\varepsilon}_{ij} = D^{-1}_{ijkl}\dot{\sigma}_{kl} \quad \textbf{3.2-6}$$

$$D_{ijkl} = E_{ijkl} - \bar{h}(L)B^{-1}P_{ij}Q_{ij} \quad \textbf{3.2-7}$$

$$Q_{kl} = E_{klrs}L_{rs} \; ; \; P_{ij} = E_{ijab}R_{ab} \quad \textbf{3.2-8}$$

$$B = K_{p} + L_{ab}E_{abcd}R_{cd} \quad \textbf{3.2-9}$$

$$L = \frac{1}{K_{p}}L_{ij}\dot{\sigma}_{ij} = \frac{1}{B}Q_{kl}\dot{\varepsilon}_{kl} \quad \textbf{3.2-10}$$

where L_{ij} is the stress gradient of $f(\sigma_{ij}, q_{n})$, R_{ij}, and r_{n} are the directions of $\dot{\varepsilon}^{p}_{ij}$, and $\dot{q}_{n}$, respectively, L denotes the loading index, and K_{p} indicates the plastic modulus. The Macauley brackets define the function $\langle x \rangle = \bar{h}(x)x$, where $\bar{h}(x)$ is the Heaviside step function. From this set of equations it may be noted that plastic strains will only be predicted when the loading index is positive, i.e. the stress increment is pointed in the outward direction with respect to the yield surface. The magnitude of the plastic strain is influenced by the magnitude of the stress/strain increment and plastic modulus.

In classical plasticity, the stress state remains inside or on the yield surface. Plastic strains are predicted only when the stress state lies on the yield surface. Utilizing

the consistency condition ($\dot{f} = 0$), and Equations 3.2-5 and 3.2-10, the plastic modulus can be shown to be:

$$K_p = -\frac{\partial f}{\partial q_n} r_n \qquad \textbf{3.2-11}$$

when the stress state is located on the yield surface.

It should be noted that the elastic compliance and elastic modulus are fourth order tensors which, for the case of elastic isotropy, take the following forms:

$$C_{ijkl} = \frac{2G - 3K}{18KG}\delta_{ij}\delta_{kl} + \frac{1}{4G}\left(\delta_{ik}\delta_{jl} - \delta_{il}\delta_{jk}\right) \qquad \textbf{3.2-12}$$

$$E_{ijkl} = K\delta_{ij}\delta_{kl} + G\left(\delta_{ik}\delta_{jl} + \delta_{il}\delta_{jk} - \frac{2}{3}\delta_{ij}\delta_{kl}\right) \qquad \textbf{3.2-13}$$

where G and K are the elastic shear and bulk moduli, respectively.

3.3 Bounding surface concept and formulation in direct stress invariant space

Researchers have noted that the classical plasticity formulation has significant limitations in the prediction of stress-strain behavior of elastoplastic materials undergoing reloading events (i.e., loading events where the stress states reside inside the yield surface). The ability to predict plastic strains for reloading events was identified as an important modeling necessity, especially for models predicting the behavior of overconsolidated cohesive soils. Many models have been proposed utilizing multisurface (Hashiguchi 1977; Mroz 1966; Mroz 1967) and bounding surface (Dafalias 1975; Dafalias and Popov 1977) plasticity to accomplish this.

In bounding surface plasticity, the yield surface of classical plasticity is replaced by loading and bounding surfaces. The loading surface is an implied surface, which is defined by the current stress state. The bounding surface defines the set of states at

which yielding occurs. Loading and bounding surfaces are homologous, with the bounding surface defined by a set of "image" stress states

$$F(\bar{\sigma}_{ij},\ q_n) = 0 \qquad \textbf{3.3-1}$$

The center of homology for the loading and bounding surfaces is the projection center, denoted by α_{ij} in Figure 3.3-1. According to the radial mapping rule, the "image" stress states is defined by

$$\bar{\sigma}_{ij} = b(\sigma_{ij} - \alpha_{ij}) + \alpha_{ij} \qquad \textbf{3.3-2}$$

where b is the similarity ratio between the loading and bounding surfaces, and a bar over a value denotes its association with the bounding surface (Dafalias 1986).

Plastic strain accumulation is predicted by defining the plastic modulus for stress states falling inside the bounding surface. In order to predict increasing rates of plastic strain accumulation as the stress state approaches the bounding surface, the actual plastic modulus is taken as a function of the relative sizes of the loading and bounding surfaces with a minimum value of the image plastic modulus. Utilizing the radial mapping rule, this takes the form (Dafalias 1986):

$$K_p = \bar{K}_p + \hat{H}\frac{\delta}{\langle r - s\delta\rangle} = \bar{K}_p + \hat{H}\left\langle\frac{b}{b-1} - s\right\rangle^{-1} \qquad \textbf{3.3-3}$$

$$\bar{K}_p = -\frac{\partial F}{\partial q_n} r_n \qquad \textbf{3.3-4}$$

where (δ - r) and r are distances between the projection center, and the current and image stress states, respectively, as shown in Figure 3.3-1. The model parameter s determines the size of the elastic nucleus; and b is the aforementioned similarity ratio. The scalar shape hardening function, $\hat{H}$, combines the general form proposed by

Kaliakin and Dafalias (1989) for the single-surface bounding surface model with the improved shape hardening function proposed by Nieto-Leal and Kaliakin (2014); i.e.,

$$\widehat{H} = \frac{1 + e_{in}}{\lambda - \kappa} p_{atm}[h(\theta) z^m + h_0(1 - z^m)] \left[9(F_{,\bar{I}})^2 + \frac{1}{3}\left(F_{,\bar{J}}\right)^2 \right] f \qquad \textbf{3.3-5}$$

$$f = \frac{1}{2}\left[a + sgn(n_I)|n_I|^{1/w}\right]\left(\frac{I}{I_0}\right) \qquad \textbf{3.3-6}$$

$$h(\theta) = \frac{2k_h}{1 + k_h - (1 - k_h)\sin 3\theta} h_c \qquad \textbf{3.3-7}$$

where λ and κ are the negative of the slope of the virgin compression and recompression lines respectively, in void ratio (e) vs. $\ln(I)$ space, e_{in} is the initial void ratio, p_{atm} is the atmospheric pressure, n_I is the unit outward normal to the bounding surface in the I-direction in isotropic invariant stress space, and z is a value weighting the current and maximum possible values of J; i.e., (J/J_{max}); h_x, a, and w are fitted material parameters. The x subscript stands in place for c, e, and 0 which denote values associated with triaxial compression, triaxial extension, and in the vicinity of the I-axis, respectively. The notation k_h denotes the ratio h_e/h_c.

With the definition of the bounding surface, the loading index is redefined as:

$$L = \frac{1}{K_p} L_{ij} \dot{\sigma}_{ij} = \frac{1}{\bar{K}_p} \bar{L}_{ij} \dot{\bar{\sigma}}_{ij} \qquad \textbf{3.3-8}$$

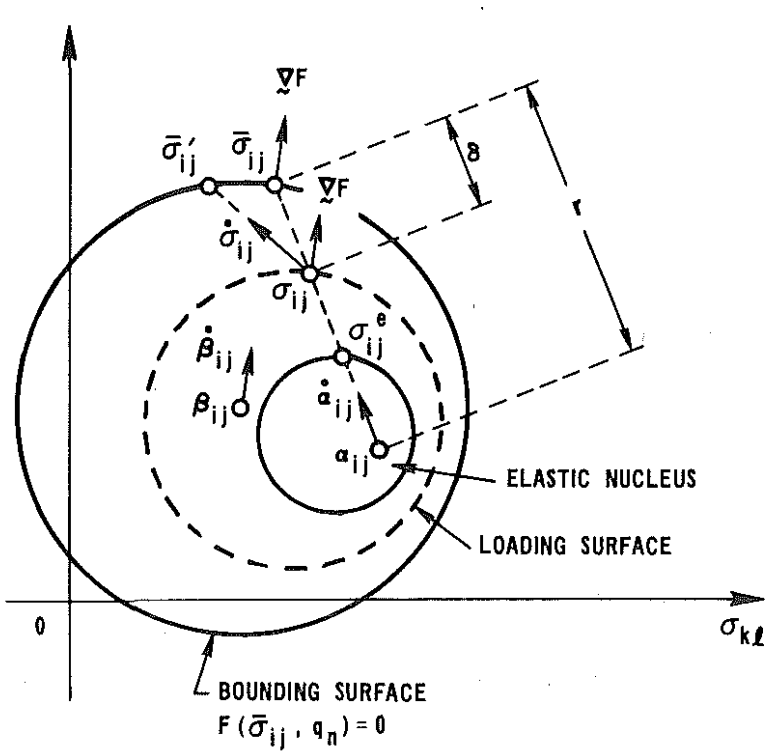

Figure 3.3-1: Schematic of bounding surface and radial mapping concepts (Dafalias 1986)

3.4 Generalization of Xiao et al. (2016) model to direct invariant stress space

The proposed model is based on, and in some cases directly adopts portions of, the Xiao et al. (2016) bounding surface Cam Clay model for cement-admixed clays. Therefore it is reasonable to present the Xiao et al. (2016) formulation, and the steps taken to generalize it into direct stress invariant space. Xiao et al. (2016) put forth a "Mohr-Coulomb generalization of the Cam-clay" model in which the effect of cementation is tracked through sensitivity (Cotecchia and Chandler 2000) and the cohesion intercept, and destructuring is taken as an effect of plastic work against the cement structure due to plastic strain accumulation. Xiao et al. (2016) predicate their extension of the Cam Clay model on the Mohr-Coulomb failure criterion, taken as

$$q = Mp' + C \qquad \textbf{3.4-1}$$

in triaxial stress space, where M is the slope of the critical state line (CSL) and C is the cohesion intercept. In order to generalize the Xiao et al. (2016) formulation from triaxial stress invariant space to direct stress invariant space, relationships outlined in Equations 3.1-3 and 3.1-4 are utilized to define

$$J = NI + D \tag{3.4-2}$$

$$N = M/3\sqrt{3}\ ;\ D = C/\sqrt{3} \tag{3.4-3}$$

where N is the slope of the CSL and D is the cohesion intercept in I-J space.

3.4.1 Equation of the bounding surface

Xiao et al. (2016) built cohesion into the Modified Cam Clay (Roscoe and Burland 1968) model beginning with the flow rule

$$dW_p = p'd\varepsilon_v^p + qd\varepsilon_s^p = \sqrt{\left(p'd\varepsilon_v^p\right)^2 + \left(Mp'd\varepsilon_s^p\right)^2} \Longrightarrow \sqrt{\left(p'd\varepsilon_v^p\right)^2 + \left\{(Mp' + C)d\varepsilon_s^p\right\}^2} \tag{3.4-4}$$

which may be rearranged and integrated to become a non-elliptical plastic potential surface. An associative flow rule is assumed. The yield surface thus takes the form

$$f = g = (p'_0 - p')\left(M^2p' + \frac{C^2}{p'_0}\right) + 2MCp'\ln\left(\frac{p'_0}{p'}\right) - q^2 = 0 \tag{3.4-5}$$

which may be restated as

$$f = g = (I_0 - I)\left(N^2I + \frac{D^2}{I_0}\right) + 2NDI\ln\left(\frac{I_0}{I}\right) - J^2 = 0 \tag{3.4-6}$$

using Equations 3.1-3, 3.1-4, and 3.4-3, where p'_0 and I_0 are the effective isotropic compression yield stress in triaxial and direct invariant stress space, respectively.

3.4.2 Hardening and destructuring

In addition to the isotropic yield stress, the cohesion intercept (C, D) and sensitivity (S) are hardening parameters used to track the effect of the cement structure. Xiao et al. (2016) adopted the Cotecchia and Chandler (2000) definition of sensitivity; i.e., the ratio of the effective isotropic compression yield stress for structured and remolded specimens for a given specific volume or void ratio ($S = p'_{0,intact}/p'_{0,remolded} = I_{0,intact}/I_{0,remolded}$) for stresses equal, or greater than, the yield stress, illustrated in Figure 2.3-6. Xiao et al. (2016), building upon the work of Xiao and Lee (2014), stated that the hardening parameters are related to volumetric and deviatoric plastic strains by:

$$dp'_0 = -\frac{\delta\lambda_u \nu}{S(\lambda_u - \kappa_s)}\left\{Sp'd\varepsilon_v^p + Sqd\varepsilon_s^p - \sqrt{\left(p'd\varepsilon_v^p\right)^2 + \left(Mp'd\varepsilon_s^p\right)^2}\right\} + \frac{\nu p'_0}{\lambda_u - \kappa_s} d\varepsilon_v^p \quad \textbf{3.4-7}$$

$$dS = -\frac{\delta\nu}{p'_0}\left\{Sp'd\varepsilon_v^p + Sqd\varepsilon_s^p - \sqrt{\left(p'd\varepsilon_v^p\right)^2 + \left(Mp'd\varepsilon_s^p\right)^2}\right\} \quad \textbf{3.4-8}$$

$$\frac{C}{C_i} = \left(\frac{S-1}{S_i-1}\right)^{\zeta} \quad \textbf{3.4-9}$$

where δ and ζ are model parameters related to the rate of destructuring, λ_u and κ_s are the slopes of the virgin compression and rebound lines on the isotropic compression curves in e vs. $\ln(p')$ space of fully remolded and intact specimens, respectively, and the i subscript denotes an initial value of the parameter.

Using the previously mentioned stress space relationships, and allowing for specification of different destructuring rates due to volumetric and deviatoric plastic strain accumulation, these hardening and destructuring relationships can be rewritten as:

$$dI_0 = -\frac{\lambda_u(1+e_{in})}{S(\lambda_u-\kappa_s)}\left\{\delta S I d\varepsilon_v^p + 3\sqrt{3}\pi S J d\varepsilon_s^p - \sqrt{\left(\delta I d\varepsilon_v^p\right)^2 + \left(3\sqrt{3}\pi N I d\varepsilon_s^p\right)^2}\right\} + \frac{1+e_{in}}{\lambda_u-\kappa_s} I_0 d\varepsilon_v^p \quad \textbf{3.4-10}$$

$$dS = -\frac{1+e_{in}}{I_0}\left\{\delta S I d\varepsilon_v^p + 3\sqrt{3}\pi S J d\varepsilon_s^p - \sqrt{\left(\delta I d\varepsilon_v^p\right)^2 + \left(3\sqrt{3}\pi N I d\varepsilon_s^p\right)^2}\right\} \quad \textbf{3.4-11}$$

$$\frac{D}{D_i} = \frac{C}{C_i} \quad \textbf{3.4-12}$$

where δ and π are model parameters related to the rate of destructuring due to volumetric and deviatoric plastic strains, respectively.

3.4.3 A single-ellipse emulation of the bounding surface

In an earlier formulation of the model, an attempt was made to emulate the Xiao et al. (2016) bounding surface by defining a bounding surface composed of a single ellipse, characterized directly by the cohesion intercept (0, D), isotropic yield stress (I_0, 0), and ellipse center (I_o/R, 0):

$$F(\bar{I}, \bar{J}, \theta, q_n) = \left(\frac{\bar{I}}{I_0} - 1\right)\left(R\frac{\bar{I}}{I_0} + (R-2)\right) + \frac{\bar{J}^2(R-2)}{D^2} = 0 \quad \textbf{3.4-13}$$

where the D and N are functions of the Lode angle, and the value of D decreases as a function of soil destructuring (i.e., governed by Equations 3.4-9, 3.4-11, and 3.4-12).

In the formulations put forth by Dafalias and Herrmann (1986) and Kaliakin and Dafalias (1989), the R value is a constant model parameter; this formulation required that the R value take a variable form in order for the surface to imitate the shape of the Xiao et al. (2016) bounding surface. A study of various cohesion ratios (I_0/D), CSL slopes (N), and best-fit R values showed a unique relationship (see Figure 3.4-1) best characterized by the trend line

$$R_{fitted} = \left(\frac{I_0}{D}N\right)^{-1.88} + 2 \qquad \textbf{3.4-14}$$

Figure 3.4-2 illustrates the form of the bounding surface and variable R value compared with the generalized Xiao et al. (2016) bounding surface (Equation 3.4-6).

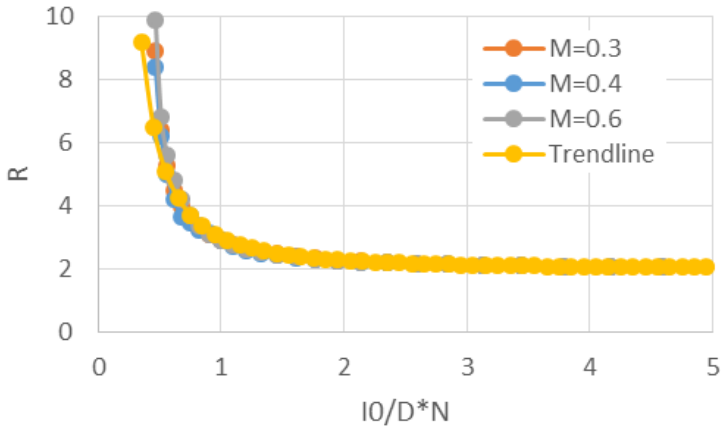

Figure 3.4-1: Fitted R-parameter with cohesion ratio and slope of the critical state line for unimproved soil

A consequence of the R parameter taking a variable form was the definition of an implied CSL, demarcated as the line connecting the origin and tallest point of the bounding surface (I_0/R, J_{max}). This value was characterized by:

$$N_{implied} = \frac{DR}{I_0}\left[1 - \frac{1}{(R-1)^2}\right]^{-1/2} \qquad \textbf{3.4-15}$$

Although this model formulation was able to capture the trends in stress-strain behavior, a number of issues became evident during the process of validating the model by comparing monotonic triaxial test results and predictions. First, the model over-predicted the deviatoric strength of normally consolidated specimens tested under undrained triaxial compression. In the Dafalias and Herrmann (1986) and Kaliakin and Dafalias (1989) bounding surface models, the R shape parameter(s) would be calibrated using normally consolidated triaxial test results and therefore control the predicted deviatoric strength. With the value of the R parameter being internally controlled, the

user does not retain the ability to control this behavior through proper parameter calibration. Second, the reliance of the bounding surface on D caused issues when S = 1, its theoretical minimum. Through Equations 3.4-9, 3.4-12, and 3.4-15 one may observe that when the soil becomes "fully-remolded" (i.e., S = 1) the values of D, $N_{implied} = 0$. A comparison of the predictive capabilities of this iteration of the model and the final proposed model will be briefly presented in Section 6.2.

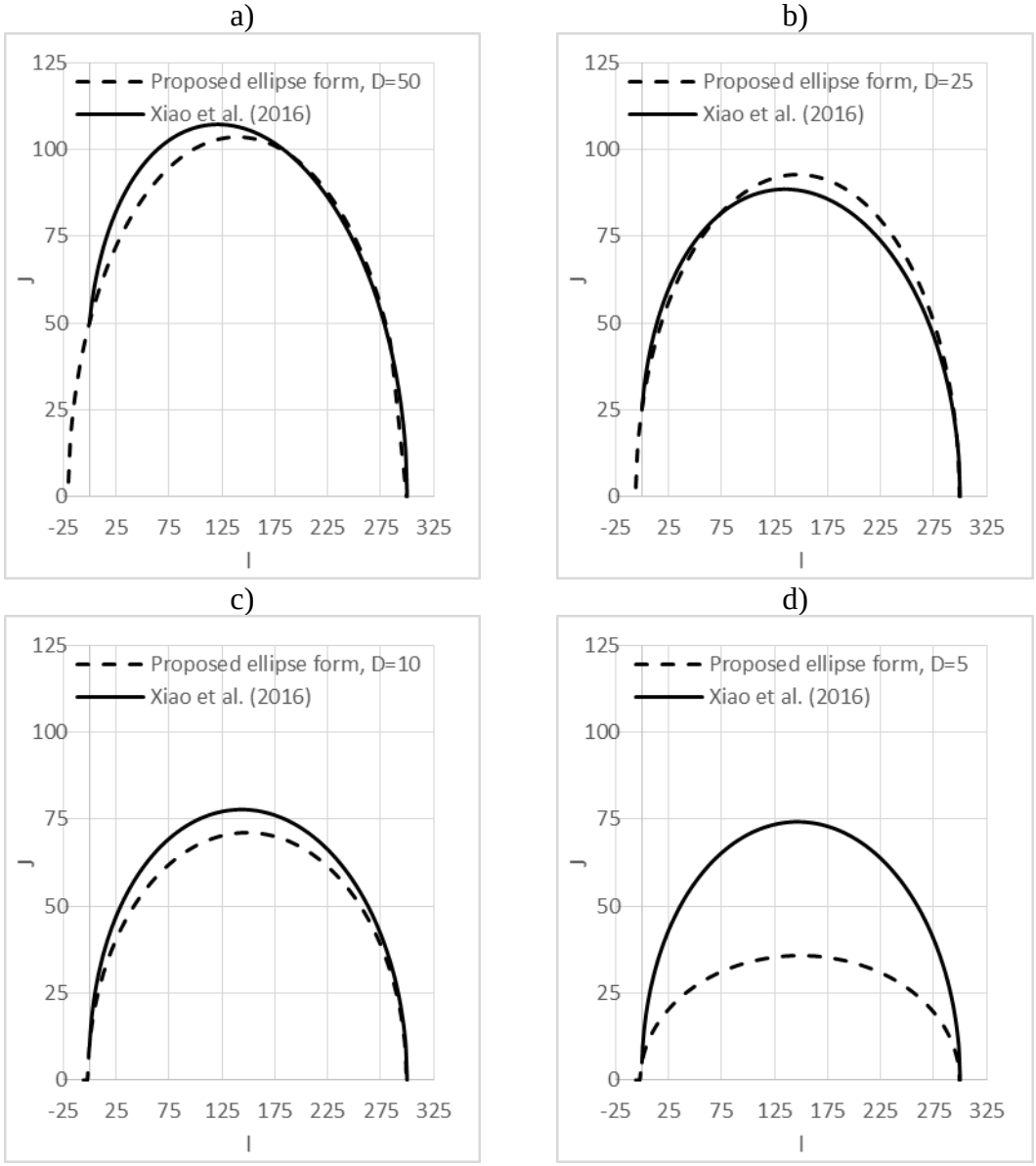

Figure 3.4-2: Prior proposed bounding surface compared with the Xiao et al. (2016) yield surface with $I_0 = 300$, M=2.45, various values of D

3.5 Formulation of the final proposed model

A single-elliptical surface bounding surface model, utilizing the radial mapping rule and an arbitrarily defined projection center, is proposed. The effects of soil structure are integrated through the sensitivity put forth by Xiao and Lee (2014) and Xiao et al. (2016). The evolution of the bounding surface is described by destructuring and aspect ratio change rules adapted from Xiao et al. (2016) and Liu et al. (2010), respectively. Including a modified Liu et al. (2010) aspect ratio change rule is the major difference from the earlier version of the model discussed in Section 3.4. The projection center is arbitrarily defined in order to facilitate easy extension to cyclic loading, further discussed in Subsection 3.5.4.

3.5.1 Continuation of general bounding surface formulation

Taking the projection center (formerly denoted as α_{ij}, but henceforth denoted as σ_{ij}^{pc}) as an arbitrarily defined point in stress invariant space, along with Equation 3.3-2, leads to the following expressions:

$$\bar{I} = b(I - I_{PC}) + I_{PC} \quad \textbf{3.5-1}$$

$$\bar{J} = b(J - J_{PC}) + J_{PC} \quad \textbf{3.5-2}$$

$$\bar{s}_{ij} = b\left(s_{ij} - s_{ij}^{PC}\right) + s_{ij}^{PC} \quad \textbf{3.5-3}$$

where the super/sub-script PC denotes a value associated with the projection center. A discussion of the procedure for determining the appropriate Lode angle (θ) for a situation in which the projection center does not coincide with the I axis is presented in Subsection 3.5.4.

Following the example of Dafalias and Herrmann (1986), for a bounding surface defined in direct stress invariant space, $F(\bar{I}, \bar{J}, \theta, q_n)$, Equations 3.1-3 to 3.1-9 and 3.1-1 to are used to define

$$L_{ij} = F_{,\bar{I}}\,\delta_{ij} + F_{,\bar{J}}\frac{\bar{s}_{ij}}{2\bar{J}} + F_{,\theta}\frac{\sqrt{3}}{2\bar{J}\cos(3\theta)}\left[\frac{\bar{s}_{ik}\bar{s}_{kj}}{\bar{J}^2} - 3\left(\frac{\bar{S}}{\bar{J}}\right)^3\frac{\bar{s}_{ij}}{2\bar{J}} - \frac{2}{3}\delta_{ij}\right] \quad \textbf{3.5-4}$$

$$Q_{ij} = 3KF_{,\bar{I}}\,\delta_{ij} + GF_{,\bar{J}}\frac{\bar{s}_{ij}}{\bar{J}} + GF_{,\theta}\frac{\sqrt{3}}{\bar{J}\cos(3\theta)}\left[\frac{\bar{s}_{ir}\bar{s}_{rj}}{\bar{J}^2} - 3\left(\frac{\bar{S}}{\bar{J}}\right)^3\frac{\bar{s}_{ij}}{2\bar{J}} - \frac{2}{3}\delta_{ij}\right] \quad \textbf{3.5-5}$$

$$B = K_p + 9KF_{,\bar{I}}\,U_{,\bar{I}} + G\left[F_{,\bar{J}}\,U_{,\bar{J}} + \frac{F_{,\theta}U_{,\theta}}{\bar{J}^2}\right] \quad \textbf{3.5-6}$$

$$L = \frac{1}{K_p}\left[F_{,\bar{I}}\,\dot{I} + F_{,\bar{J}}\,\dot{J} + \frac{1}{b}F_{,\theta}\,\dot{\theta}\right] = \frac{1}{\bar{K}_p}\left[F_{,\bar{I}}\,\dot{\bar{I}} + F_{,\bar{J}}\,\dot{\bar{J}} + F_{,\theta}\,\dot{\theta}\right] \quad \textbf{3.5-7}$$

for this formulation. R_{ij} and P_{ij} are found by substituting U for F in Equations 3.5-4 and 3.5-5, respectively. An associative flow rule is assumed, therefore $F(\bar{I}, \bar{J}, \theta, q_n) = U(\bar{I}, \bar{J}, \theta, q_n) = 0$. The partial derivatives of the bounding surface required for the full expression of these equations are provided in Appendix A.

3.5.2 Specific form of the bounding surface

This formulation expands upon the Kaliakin and Dafalias (1989) Lode angle dependent, single-ellipse bounding surface by allowing the aspect ratio of the surface to evolve with degradation of the soil structure. The surface is defined by the isotropic yield stress (I_0, 0), ellipse center (I_o/R, 0), and the peak of the surface (I_o/R, NI_o/R):

$$F(\bar{I}, \bar{J}, \theta, q_n) = (\bar{I} - I_0)\left(\bar{I} + \frac{R-2}{R}I_0\right) + (R-1)^2\left(\frac{\bar{J}}{N}\right)^2 = 0 \quad \textbf{3.5-8}$$

where N depends on the Lode angle according to:

$$N(\theta) = N_c g_N(\theta);$$
$$g_N(\theta) = \left[\frac{2k_N{}^4}{1+k_N{}^4-(1-k_N{}^4)\sin(3\theta)}\right]^{1/4} \quad \textbf{3.5-9}$$

and $k_N = M_e^*/M_c^*$, as proposed by Sheng et al. (2000).

The Liu et al. (2010) equation for the variable slope of the critical state line (Equation 2.3-7) is modified to characterize the relationship between the structured and reference states via the sensitivity framework. Variability in the value of N is integrated into the formulation via the calculation of the critical state line in triaxial compression

$$N_c = \frac{N_c^*}{1-\mu \ln S} \quad \textbf{3.5-10}$$

where N_c^* is the large-strain slope of the critical state line in triaxial compression in direct stress invariant space and μ is a model parameter that dictates the magnitude of the variability in the aspect ratio.

3.5.3 Hardening and destructuring

The dependence of destructuring on both volumetric and shear plastic strains makes the hardening and destructuring formulation proposed by Xiao et al. (2016) well suited for capturing stress-strain behavior under a wide range of load paths and conditions. The generalized relationships presented in Equations 3.4-10 and 3.4-11 are adopted in this formulation. From this set of equations, the set of internal variables, q_n, are taken as the plastic volumetric and deviatoric strains.

Expanding upon Equation 3.3-4, and using Equation 3.2-5 and the consistency condition ($\dot{F} = 0$), the image plastic modulus takes the form:

$$\bar{K}_p = -3\frac{\partial F}{\partial \varepsilon_v^p} F_{,\bar{I}} - \frac{1}{\sqrt{3}}\frac{\partial F}{\partial \varepsilon_s^p}\sqrt{F_{,\bar{J}}^2 + \left(\frac{F_{,\theta}}{\bar{J}}\right)^2} \quad \textbf{3.5-11}$$

$$\frac{\partial F}{\partial \varepsilon_v^p} = \frac{\partial F}{\partial I_0}\frac{\partial I_0}{\partial \varepsilon_v^p} + \left(\frac{\partial F}{\partial N}\frac{\partial N}{\partial S}\right)\frac{\partial S}{\partial \varepsilon_v^p} \quad \textbf{3.5-12}$$

$$\frac{\partial F}{\partial \varepsilon_s^p} = \frac{\partial F}{\partial I_0}\frac{\partial I_0}{\partial \varepsilon_s^p} + \left(\frac{\partial F}{\partial N}\frac{\partial N}{\partial S}\right)\frac{\partial S}{\partial \varepsilon_s^p} \quad \textbf{3.5-13}$$

The partial derivatives of the isotropic compression stress and sensitivity with respect to the volumetric and deviatoric plastic strains may be taken from the total derivatives

presented in Equations 3.4-10 and 3.4-11. Following the lower limit formulation utilized in Equations 27a and 27b of Dafalias and Herrmann (1986), the partial derivatives may be taken as:

$$\frac{\partial I_0}{\partial \varepsilon_v^p} = \frac{1+e_{in}}{S(\lambda_u - \kappa_s)}\{S[\langle I_0 - I_l\rangle + I_l] - \delta\lambda_u(S-1)[\langle I - I_l\rangle + I_l]\} \quad \textbf{3.5-14}$$

$$\frac{\partial I_0}{\partial \varepsilon_s^p} = \frac{-3\sqrt{3}\pi\lambda_u(1+e_{in})}{S(\lambda_u - \kappa_s)}\{SJ - N[\langle I - I_l\rangle + I_l]\} \quad \textbf{3.5-15}$$

$$\frac{\partial S}{\partial \varepsilon_v^p} = -\delta(1+e_{in})(S-1)\frac{[\langle I - I_l\rangle + I_l]}{[\langle I_0 - I_l\rangle + I_l]} \quad \textbf{3.5-16}$$

$$\frac{\partial S}{\partial \varepsilon_s^p} = \frac{-3\sqrt{3}\pi\lambda_u(1+e_{in})}{[\langle I_0 - I_l\rangle + I_l]}\{SJ - N[\langle I - I_l\rangle + I_l]\} \quad \textbf{3.5-17}$$

The functional forms of the actual plastic modulus and shape hardening functions adopted in this formulation are presented as Equations 3.3-3 through 3.3-7, where the z parameter will be calculated based on the variable slope of the CSL, $z = JR/(NI_0)$. The partial derivatives of the bounding surface and bounding surface parameters required for the full expression of these equations are provided in Appendix A.

3.5.4 Bounding surface extension to cyclic loading

As discussed in Section 2.2, relocating the projection center when the direction of the stress path reverses (tested by a change in the sign of the loading index L) is one method in modeling the hysteresis behavior of cyclically loaded soils. Determination of image stresses and stress invariants (i.e., projection of the current stress state onto the bounding surface) in the I-J plane follows neatly from Equations 3.5-1 and 3.5-2. However, allowing the projection center to be defined as any stress state falling inside, or on, the bounding surface may result in a projection center stress state having a non-zero deviatoric component (i.e., $s_{ij}^{PC} \neq 0;\ J_{PC} \neq 0$). Figure 3.5-1b demonstrates the inadvertent effect that the calculation of the image Lode angle ($\bar{\theta}$), based on the image

deviatoric stress tensor ($\bar{s}_{ij}$) via Equations 3.1-4 through 3.1-6, may not be the same value of the Lode angle associated with the actual deviatoric stress tensor (Nieto Leal 2016). The Lode angle dependence of the bounding surface equation requires that the "image" Lode angle being used is correct and consistent with the Lode angle for the actual state of stress (Nieto Leal 2016).

In order to ensure the actual and image Lode angles are consistent, the Nieto Leal (2016) procedure for correcting image Lode angle is adopted in this formulation. The Lode angle correcting radial mapping procedure is given as follows:

1. Calculate the stress invariants, I_{PC} and J_{PC}, and deviatoric stress tensor, s_{ij}^{PC}, associated with the projection center.
2. Solve for "local" similarity ratio, b_L, by considering the explicit expression for the bounding surface (with the assumption that the bounding surface is temporarily independent of the Lode angle). The image stresses affiliated with the current stress state are defined by the equivalencies provided in Equations 3.5-1 and 3.5-2, where b is replaced by the "local" similarity ratio, b_L. A closed form solution for the similarity ratio is provided in Appendix B.
3. The center of the loading surface in deviatoric stress space, s_{ij}^{C}, will be taken as:

$$s_{ij}^{C} = s_{ij}^{PC} - \frac{1}{b_L} s_{ij}^{PC} = \left(1 - \frac{1}{b_L}\right) s_{ij}^{C} \qquad \textbf{3.5-18}$$

4. Intermediate values of the stress invariants, J_L and T_L, and correct Lode angle, θ_L, are calculated using the intermediate deviatoric stress tensor in Equations 3.1-4, 3.1-5, and 3.1-6:

$$s_{ij}^{L} = s_{ij} - s_{ij}^{C} \qquad \textbf{3.5-19}$$

5. Using the correct Lode angle, θ_L, determine the correct similarity ratio, b, by solving the bounding surface equation with the image stresses defined by Equations 3.5-1 and 3.5-2.

This corrected Lode angle should be used for all instances of the Lode angle occurring in the present formulation; however, it is important to note that instances of the image deviatoric stress tensor, $\bar{s}_{ij}$, in the present formulation refers to the value given by the equivalency in Equation 3.5-3, using the correct similarity ratio determined in step 5, and not any intermediate value of the deviatoric stress tensor calculated in the Lode angle correction procedure.

As the projection center must not be located outside the bounding surface, it is prudent to employ a law to describe the evolution of the projection center during a single loading event (the sum of the loading increments between two sequential stress reversals or the beginning/conclusion of loading). The Nieto Leal (2016) isotropic hardening based evolution rule, Equation 3.5-20, is adopted.

$$\dot{\sigma}'^{PC}_{ij} = \left(\dot{I}_0/I_0\right)\sigma'^{PC}_{ij} \qquad \textbf{3.5-20}$$

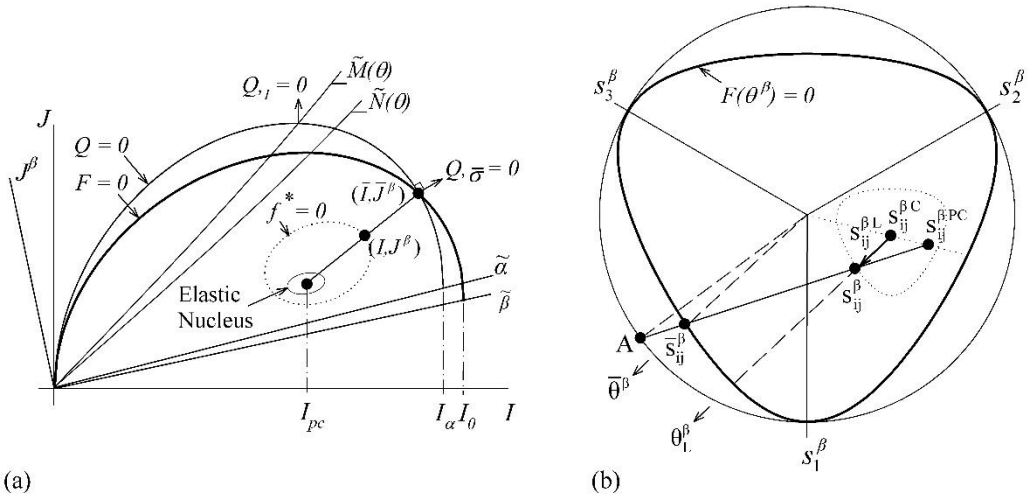

Figure 3.5-1: Definitions for the radial mapping rule in (a) invariant stress space, and (b) in the octahedral plane of deviatoric stress space (Nieto Leal 2016)

Chapter 4: Numerical implementation

In order to numerically implement the model proposed in Section 3.5 in a manner which is easily accessible to geotechnical engineering professionals and researchers, an algorithm was written to complete the numerical evaluation of the model. The algorithm, BONDCLAY, was created by editing an existing Fortran 77 set of subroutines for the numerical evaluation of the bounding surface model for isotropic cohesive soils (Dafalias and Herrmann 1986), CLAY. The numerical implementation scheme utilized in this code is outlined by Herrmann et al. (1987) and, as it is directly adopted for the new algorithm, is presented in this chapter for completeness.

4.1 General statements on the utility of BONDCLAY algorithm

The BONDCLAY algorithm "solves" the stress-strain relationship for a single element (i.e., a single point) over a single increment. When incorporated into a finite element (FE) program, the FE program will call the BONDCLAY algorithm to solve the general incremental relationship:

$$\{\Delta\sigma\}_{N,K} = [\bar{D}]_{N,K-1}\{\Delta\varepsilon\}_{N,K} + \{\Delta\sigma_0\}_{N,K-1} \qquad \textbf{4.1-1}$$

for each spatial integration point, where K is a given iteration for a particular solution step N, and $\{\Delta\sigma_0\}$ is a stress correction vector used exclusively in the global solution. For implementation into a computer program, it is convenient to express the second order stress, σ_{ij}, and strain, ε_{ij}, tensors and fourth order stiffness tensor, D, as 6x1 ($\{\sigma\}$, $\{\varepsilon\}$), and 6x6 matrices ([D]), respectively. It should also be noted that since the proposed model is highly non-linear and history dependent, global (on the increment solution scale) and local (inside an incremental solution) iteration are important for the calculation of accurate predictions.

4.2 Numerical implementation

Many of the equations presented in Chapter 3 are rate relationships. Although this model is rate-independent, it is easier for discussion purposes to think of global increments as time-steps, Δt_N. To solve the stress-strain relationship over (time)step N, 4.1-1 is integrated over the range of the (time)step:

$$\int_{t_{N-1}}^{t_N} \{\dot{\sigma}\}_{N,K} dt = \int_{t_{N-1}}^{t_N} [D]_{N,K-1} \{\dot{\varepsilon}\}_{N,K} dt \qquad \textbf{4.2-1}$$

where the strain rate is approximated by $\{\dot{\varepsilon}\} = \{\Delta\varepsilon\}/\Delta t_N$. By integrating the left-hand side, Equation 4.2-1 can be shown to equal Equation 4.1-1, if $[\overline{D}]$ is taken as an average of D over the (time)step:

$$[\overline{D}]_{N,K-1} = \frac{1}{\Delta t_N} \int_{t_{N-1}}^{t_N} [D]_{N,K-1} dt \qquad \textbf{4.2-2}$$

The procedure for ensuring adequate approximation of the stiffness matrix, $[\overline{D}]$, over the increment is the subject of the next subsection. It should be noted that the information in the preceding paragraph and next subsection have dealt with the numerical integration of the stress-strain relationship. Specific forms of the numerical integration of the dI_0 and dS relationships are presented in Appendix C.

4.2.1 Substepping and local iteration

In order to confirm the correctness of the integration, indicated by results conforming to two convergence criteria described later, the increment is divided into M = 1, 2, 4, 8, 16, 32 substeps. Assuming proportional strain components, the multistep trapezoidal rule is used to redefine Equation 4.2-2:

$$[\bar{D}]_{N,K-1} = \sum_{m=1}^{M} [\bar{D}]_{N,K-1}^{m} \quad \textbf{4.2-3}$$

$$[\bar{D}]_{N,K-1}^{m} \cong \frac{1}{2\Delta t_m}\left([D]_{N,K-1}^{m-1} + [D]_{N,K-1}^{m}\right) \quad \textbf{4.2-4}$$

where $[D]_{N,K-1}^{m-1}$ and $[D]_{N,K-1}^{m}$ are the values of [D] at the beginning and end of the substep, respectively.

If the substeps are taken to be of equal size, the size of a substep for global step N is $\Delta t_m = \Delta t_N/M$, where the time at a given substep can be taken as $t_m = t_{N-1} + m\Delta t_m = t_{m-1} + \Delta t_m$. Following this format, the strain and stress at time t_m are

$$\{\varepsilon\}_m \cong \{\varepsilon\}_{N-1} + \frac{m}{M}\{\Delta\varepsilon_N\} \quad \textbf{4.2-5}$$

$$\{\sigma\}_m \cong \{\sigma\}_{N-1} + \{\Delta\sigma_m\} = \{\Delta\sigma\}_{N-1} + \sum_{i=1}^{m-1}\{\Delta\varepsilon\}_i + \{\Delta\sigma\}_m \quad \textbf{4.2-6}$$

where the $\{\Delta\sigma\}_m$ tensor is updated in each local iteration using appropriate strain rate and stiffness matrix values from the previous local iteration.

Two tests are implemented to determine the appropriate number of substeps, M, into which a solution step is divided. Each solution step N will first be approached as a single step (i.e., M=1). After the appropriate calculations are completed, a stress state $\{\sigma\}$ will be predicted. If this $\{\sigma\}$ falls outside of the bounding surface, indicated by a corresponding value of b (see Equation 3.3-2) less than 1 (actual implemented value 0.999), a problem has occurred with the numerical integration and the number of substeps, M, will be doubled. This test is repeated until the b value check is passed or M=32. The number of substeps required to pass the b value check will be taken as the minimum M for all subsequent global iterations of the N^{th} solution step; this value will

not decrease, but may be increased if smaller substeps are deemed appropriate. The second test for appropriate substep size is an assessment of the convergence of the solution. To satisfy that convergence has occurred

$$\frac{|L_0^n - L_0^m|}{L_0^n} < 0.01 \qquad \textbf{4.2-7}$$

where L_0^n and L_0^m are the sums of the absolute values of the calculated incremental stress components at the end of the increment where m = 2n ≤ 32. Each substep undergoes up to five local iterations to determine $\{\Delta\sigma\}_m$. Local iteration is concluded when Equation 4.2-7 is satisfied where b values calculated from two consecutive local iterations are used in place of the L_0^x values.

4.2.2 Radial return correction procedure

When a calculated b value indicates that a stress state falls outside the bounding surface, the radial return procedure (Hughes 1984) is adopted to move the stress state back to the bounding surface. The scaled stress state and stress correction vector can be taken as:

$$\{\sigma\}_{N-1_{scaled}} = b\left[\{\sigma\}_{N-1} - \{\sigma\}_{N-1}^{PC}\right] + \{\sigma\}_{N-1}^{PC} \qquad \textbf{4.2-8}$$

$$\{\Delta\sigma_0\} = (b-1)[\{\sigma\} - \{\sigma\}^{PC}] \qquad \textbf{4.2-9}$$

and the scaled direct stress invariants can be calculated following Equations 3.1-3 through 3.1-5.

4.3 Incorporating pore water pressure

This section will address some of the issues pertaining to implementing the BONDCLAY algorithm into a parent FE program, specifically notes on incorporating pore water pressure into the stress-strain predictions for drained and undrained conditions. As the BONDCLAY algorithm only considers the stress-strain relationship

in terms of effective stresses, additional considerations must be made to incorporate the influence of pore water pressure for specific drainage conditions. Traditionally, two separate approaches have been taken to include the effects of pore water pressure in the soil response. First the change in pore water pressure is calculated directly from the volumetric strain increment and added directly into Equation 4.1-1:

$$\{\Delta\sigma\}_{N,K}{}^{t} = [\bar{D}]_{N,K-1}\{\Delta\varepsilon\}_{N,K} + \Delta u_{N,K}\{1\} + \{\Delta\sigma_0\}_{N,K} \quad \textbf{4.3-1}$$

$$\Delta u_{N,K} = \Gamma\Delta\varepsilon_{kk_{N,K}} \quad \textbf{4.3-2}$$

where $\{1\}=\{1,1,1,0,0,0\}^T$ and Γ is the combined bulk modulus of the pore fluid and solid phase. Alternatively, the total stress tensor can be calculated by including the influence of the pore water pressure into the stiffness matrix by:

$$\{\Delta\sigma\}_{N,K}{}^{t} = \left([\bar{D}]_{N,K-1} + [d]\right)\{\Delta\varepsilon\}_{N,K} + \{\Delta\sigma_0\}_{N,K} \quad \textbf{4.3-3}$$

where [d] is a 6x6 matrix populated by Γ in the left uppermost 3x3 submatrix and 0 in the remaining values. From these two formulations it is apparent that the values of Γ is of utmost importance in the pore water pressure predictions. Even though few real-world situations can be classified as being truly undrained or fully drained, most analyses are specified as one of these two drainage conditions. A fully drained condition is specified by $\Gamma = 0$, where no stiffness is contributed by pore fluids; conversely, an undrained condition is specified by setting $\Gamma = 2.20\text{x}10^6$ kPa, the bulk modulus of water. Herrmann et al. (1987) give additional details pertaining to the numerical implementation of bounding surface constitutive models for cohesive soils.

Chapter 5: Parameters: fitting and sensitivity analysis

The proposed model formulation requires the specification of fifteen parameters to characterize the initial state and elastoplastic response. This set of values can be subdivided into five categories: initial state parameters, traditional elastoplastic material parameters, destructuring parameters, hardening parameters, and bounding surface configuration parameters. Each parameter will be discussed with respect to its physical or model context, its method of determination, and its effects on model predictions. A list of all the model parameters and typical values for all parameters are given in Table 5.6-1.

A set of parameters should be determined for each chemical stabilization mix design (i.e. cement content, water content, approximate initial void ratio and curing conditions) and remolded soil. Establishing this set of parameters will require a set of eight laboratory tests, including:

1. An isotropic (preferred) or oedometer consolidation test on one structured and one fully remolded specimen, and
2. Six consolidated, undrained (preferred) or drained, triaxial tests on each of the following: one normally consolidated, one lightly overconsolidated, and one heavily overconsolidated improved structured specimen, sheared in compression (three total) and extension (three total).

Initial state and traditional material parameters, with the exception of P_L, are determined directly from this set of laboratory tests. Values of P_L, m, h_0, and w are considered fixed, or are determined with respect to other model parameters. The remainder of the parameters should be established by curve-fitting analytical solutions to laboratory test

results. A quick overview of the suggested range of values and calibration procedure is provided at the end of this chapter.

5.1 Initial state parameters

The parameters characterizing the initial state of the specimen are the initial void ratio (e_{in}), stress history [in the form of the isotropic or oedometer consolidation yield stress or maximum past consolidation pressure (p'_0)], and initial sensitivity (S_i). Additionally, the initial stress state is specified by the confining pressures (σ_x, σ_y, σ_z) and the initial pore water pressure (u_0). The physical meaning and determination of void ratio and consolidation yield stress are standard procedures within the larger geotechnical engineering field and their use in elastoplastic modeling of geomaterials is an established practice; therefore, they will not be further discussed herein.

5.1.1 Initial sensitivity S_i

Sensitivity is the parameter used to track the amount and influence of the intact bond structure, relating the strength of the bonded and remolded soils for a given specific volume or void ratio. The initial value of sensitivity is identified by relating the compression curves of the chemically stabilized and remolded soil, as shown in Figure 2.3-6. First, the stress and specific volume (or void ratio) of the treated specimen at yield should be determined (p'_{0i} and v_{0i}, respectively). Next, the virgin compression line for the remolded specimen should be extended such that the mean effective stress corresponding to the previously identified specific volume at yield can be determined (p'_{0ui}). The initial sensitivity is defined as:

$$S_i = {p'_{0i}}\Big/{p'_{0ui}} \qquad \textbf{5.1-1}$$

In the case that p'_{0ui} is excessively small, a lower limit value may be imposed. The value of initial sensitivity must be equal or greater than 1.

5.1.2 Initial stress-state and maximum past pressure specification

An important feature of the proposed formulation is the ability to predict destructuring of the improved soil skeleton due to isotropic and shear loading. Correctly specifying the initial stress state and maximum past pressure is important in tracking destructuring for model predictions. How the initial stress-state is specified is determined by the imposed loading used in the prediction; the following terminology will be adopted here to disambiguate these "loading types:"

- *Pre-yield, artificially overconsolidated* – This term applies to specimens which are consolidated to stress-state less than the isotropic or oedometer yield stress (p'_{0i}). The initial OCR for a prediction of this type will be defined with respect to the yield stress and will be denoted as the artificial OCR.
- *Normally consolidated (NC)* – This term applies to specimens which are consolidated to a stress-state equal to or greater than the isotropic or oedometer consolidation yield stress (p'_{0i}) prior to being sheared.
- *Overconsolidated (OC)* – This term applies to specimens which are consolidated to a stress-state greater than the isotropic or oedometer consolidation yield stress (p'_{0i}) and unloaded to a lower stress state prior to being sheared.

The initial stress-state of pre-yield, artificially overconsolidated predictions may be specified by declaring the initial confining stresses directly and setting the maximum past pressure equal to the isotropic or oedometer consolidation yield stress (p'_{0i}).

Conversely, destructuring of the specimen due to consolidation past yield in normally consolidated and over consolidated predictions should be specified in one of two ways: allowing the model to predict consolidation and destructuring as the first loading step(s) of the prediction, or direct specification with the effects of destructuring calculated and directly specified by the user. If the first method is chosen, the initial stress-state and maximum past pressure should be specified as the yield stress, then the initial loading increment(s) should be used to specify consolidation past the yield stress. If the second method is selected, the true initial stress-state and true maximum past pressure may be directly specified. However, the user should calculate the evolution of sensitivity (3.4-8/3.4-11) and cohesion (3.4-9/3.4-12) and use these values in place of their respective initial values, as discussed in the section above.

5.2 Elastic and critical state material constants

This set of material constants includes the elastic shear modulus (may also be calculated if Poisson's ratio, ν, is specified) and critical state parameters: slopes of the remolded virgin compression (λ_u) and structured rebound (κ_s) lines in e-ln(p') space, and large-strain slope of the critical state lines in q-p' space in compression and extension (M_c* and M_e*, respectively). The influence of varying the critical state parameters is presented in Figure 5.2-1, Figure 5.2-2, and Figure 5.2-3. The bulk elastic modulus is calculated as:

$$K = \frac{(1+e_{in})}{3\kappa_s}(\langle I - I_L \rangle - I_L) \qquad \textbf{5.2-1}$$

where I_L is a transitional stress used to limit excessive softening when very small values of I are used (Dafalias and Herrmann 1986). The transitional stress is specified by P_L, where $I_L = 3P_L$. Traditionally, P_L, which is not a model parameter, has been specified as one-third of the atmospheric pressure (P_{atm}) in applications of the Dafalias and Herrmann (1986) and Kaliakin and Dafalias (1989) bounding surface model for isotropic cohesive soils. The same definition is retained here.

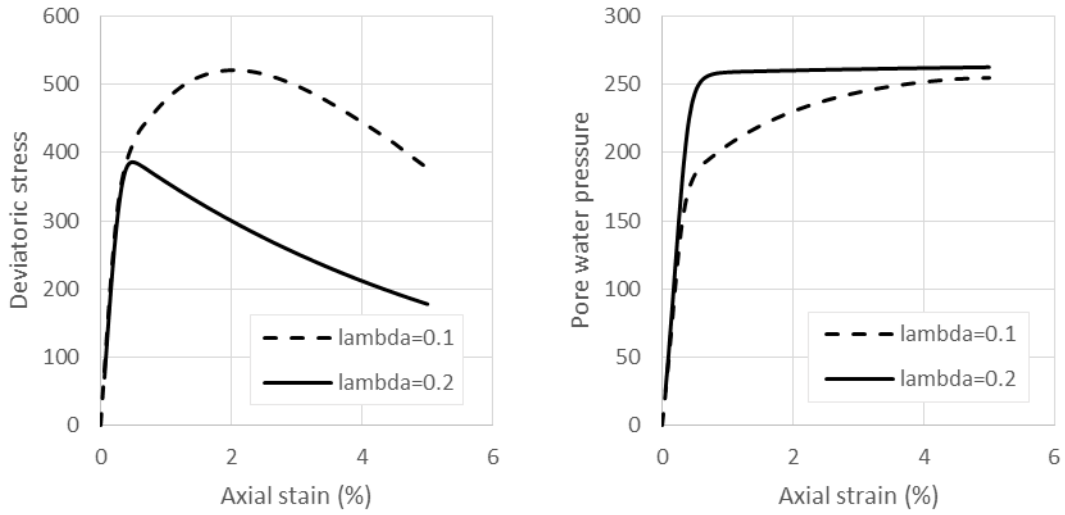

Figure 5.2-1: Effect of varying λ_u on the predicted stress-strain and pore pressure-strain response of soil specimens at OCR = 2.0 subjected to conventional undrained triaxial loading

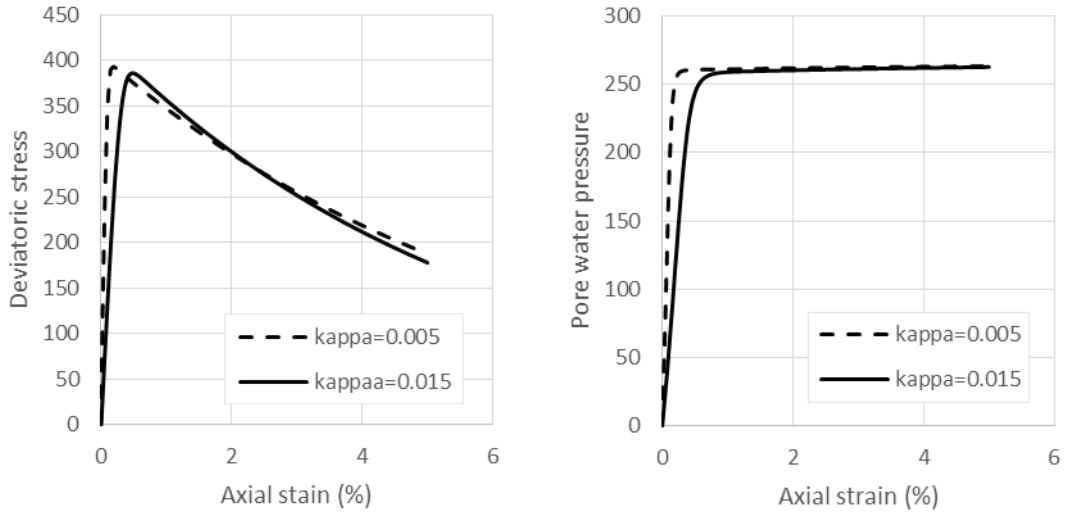

Figure 5.2-2: Effect of varying κ_s on the predicted stress-strain and pore pressure-strain response of soil specimens at OCR=2.0 subjected to conventional undrained triaxial loading

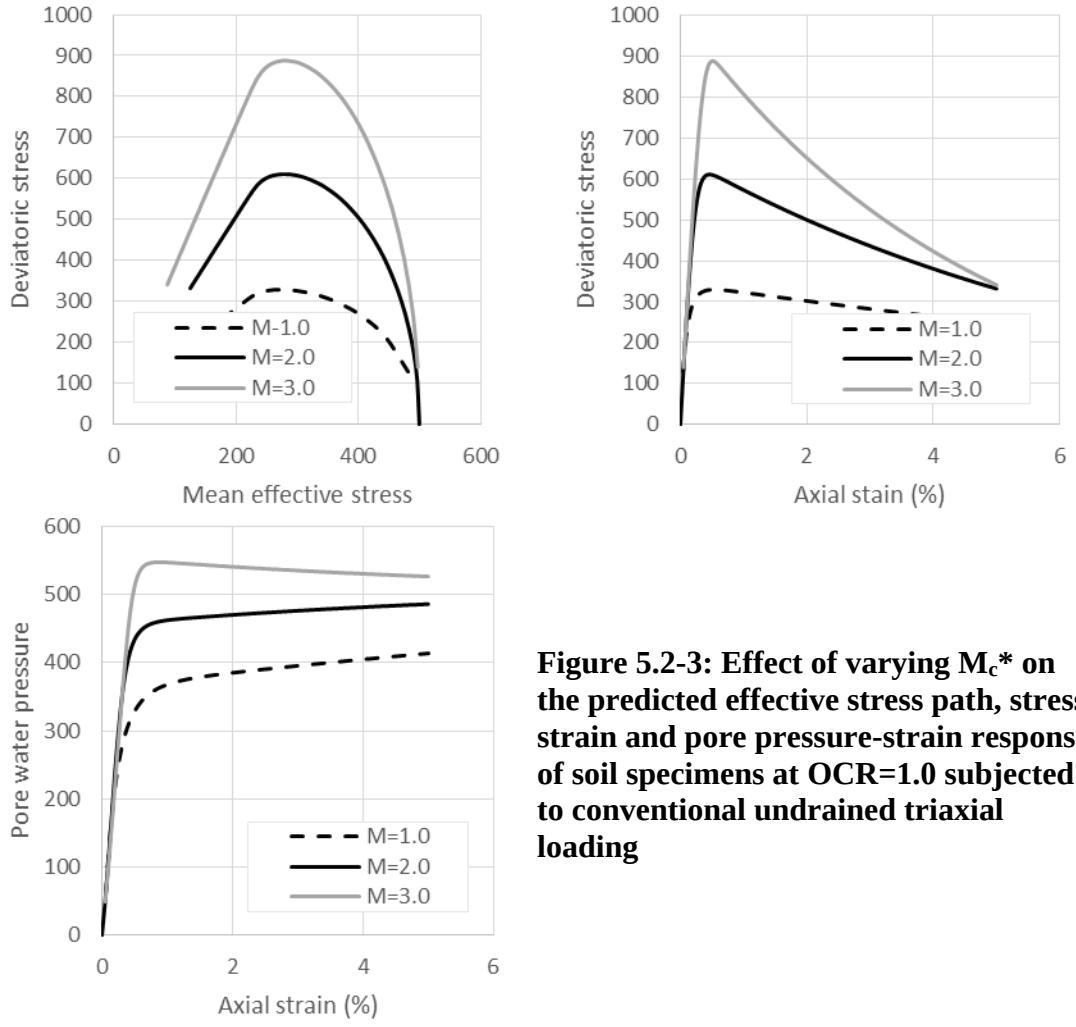

Figure 5.2-3: Effect of varying M_c* on the predicted effective stress path, stress-strain and pore pressure-strain response of soil specimens at OCR=1.0 subjected to conventional undrained triaxial loading

5.3 Structure degradation parameters

This set of parameters dictates the rate of destructuring due to accumulation of plastic strains, as detailed in Equations 3.4-7 through 3.4-12.

5.3.1 Destructuring rate parameter δ

The δ destructuring rate parameter characterizes both the rate of change in the size of the bounding surface (I_0) and value of sensitivity (S) due to plastic volumetric strain. This parameter should be greater than or equal to zero, where δ = 0 results in no changes in sensitivity and I_0 due to plastic volumetric strain.

Xiao and Lee (2014) proposed a method of determining δ from isotropic consolidation test results. Results of a structured consolidation test should be analyzed and plotted in $\ln\left(\frac{1-D}{\Theta-D}\right)$ vs. $\left[-(\lambda_u-\kappa_s)\frac{\Delta\nu}{\lambda_u}-\kappa_s\ln\Theta\right]$ space, where:

$$D = {}^{1}/_{S_i} \qquad \textbf{5.3-1}$$

$$\Theta = {}^{S}/_{S_i} \qquad \textbf{5.3-2}$$

The δ parameter is taken as the slope of the linear best fit line through the plotted results characterizing the virgin compression behavior, as shown in Figure 5.3-1.

While the Xiao and Lee (2014) determination procedure will produce a highly precise value, the amount of analysis required may be daunting for some users. It is suggested here that δ may be determined through fitting analytical results to consolidation test results. This process will be simplest if isotropic, as opposed to oedometer, consolidation results are used.

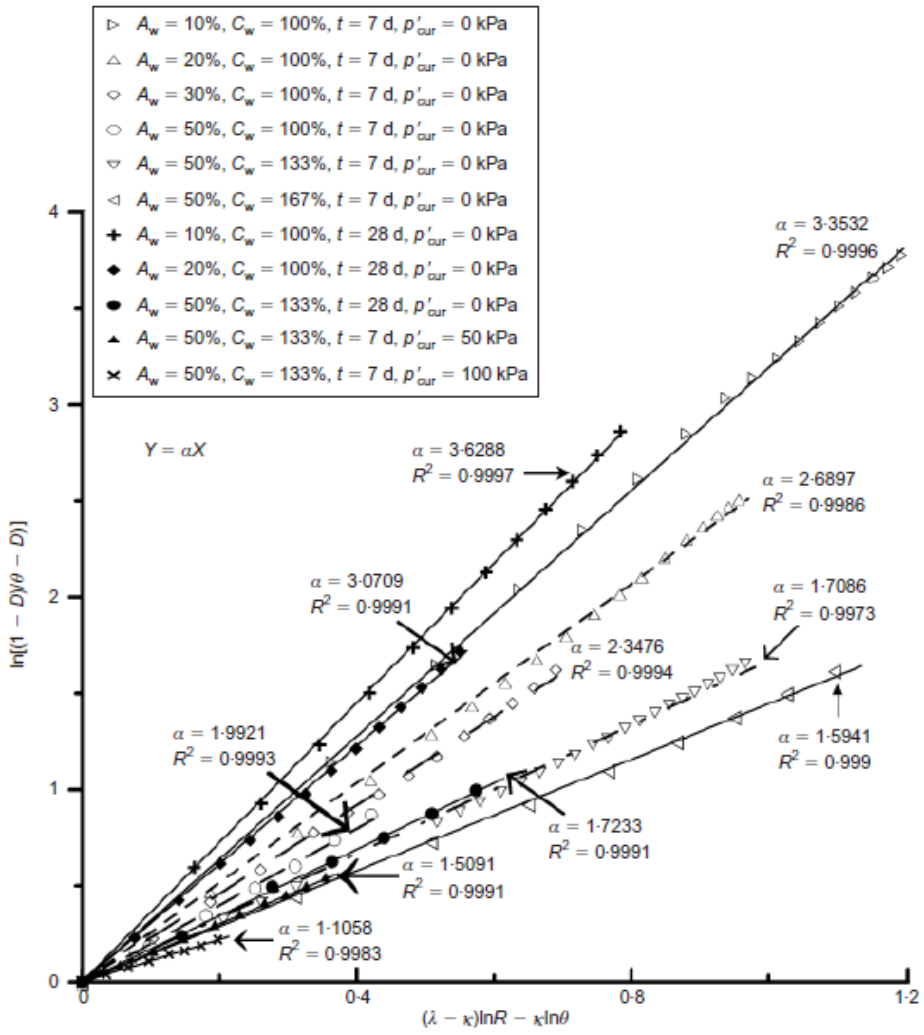

Figure 5.3-1: Determination of δ degradation parameter from consolidation test results (Xiao and Lee 2014)

5.3.2 Destructuring rate parameter π

The π parameter is used to characterize the destructuring rate due to plastic deviatoric strain accumulation. Similar to the δ parameter, π should be greater than or equal to zero, where π = 0 results in no changes in sensitivity and I_0 due to plastic deviatoric strain.

The value of the π parameter should be established by curve-fitting deviatoric stress versus axial strain (undrained) or deviatoric strain (drained) data for normally

consolidated specimens. This process will be simplest if undrained test data is used as destructuring will be a function of deviatoric strain alone. The influence of the π parameter on undrained and drained deviatoric stress versus strain is shown in Figure 5.3-2.

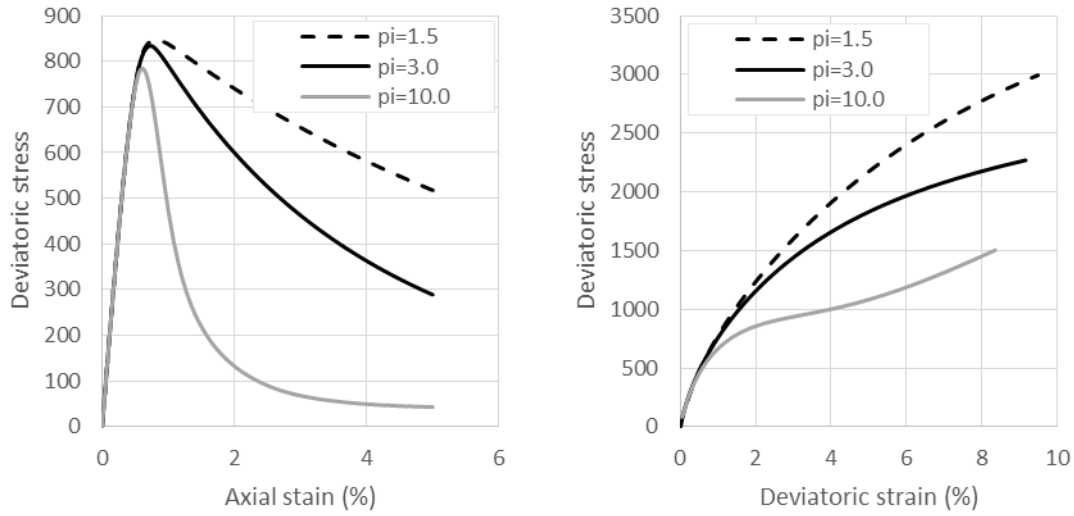

Figure 5.3-2: Effect of varying π on the predicted stress-strain response of soil specimens at OCR=1.0 subjected to conventional undrained (left) and drained (right) triaxial loading

5.4 Bounding surface configuration parameters

5.4.1 Initial projection center parameter c

The ability to define an initial projection center:

$$\left(I_{PC}^{i}, J_{PC}^{i}\right) = (cI_0, 0) \qquad \textbf{5.4-1}$$

has been preserved as a legacy feature from the Dafalias and Herrmann (1986) bounding surface for isotropic cohesive soils formulation. Implementation of the updating projection center rules complicates and limits the utility of specifying the c parameter. In theory the value of c may be set in the range of zero to one, where c = 0 sets the initial projection center at the origin in direct stress invariant space. However, in practice I_{PC}^{i} must be less than or equal to the I-coordinate of the initial stress state; if

this test is not satisfied, the projection center will be updated to the initial stress state in accordance with the projection center relocation rules. As a result, the proposed model formulation will not be able to predict initial dilation under drained loading conditions, an important feature of the Dafalias and Herrmann (1986) model's ability to predict the behavior of heavily overconsolidated soils.

Variation of c will influence degree of dilation or compaction predicted for overconsolidated specimens, as shown in Figure 5.4-1. The value of c should be established via curve-fitting pore water pressure (undrained) or volumetric strain (drained) versus axial strain behavior of lightly overconsolidated specimens.

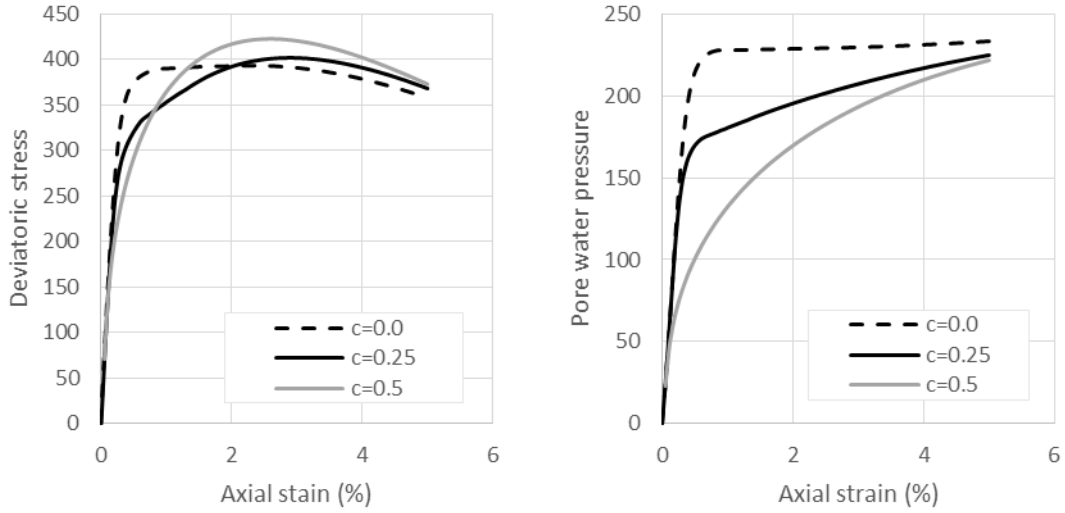

Figure 5.4-1: Effect of varying c on the predicted stress-strain and pore pressure-strain response of soil specimens at OCR=2.0 subjected to conventional undrained triaxial loading

5.4.2 Elastic zone parameter s

The elastic zone parameter defines an implied surface (similar and homologous to the bounding surface at the projection center) inside which only elastic strains are predicted. The s parameter may, theoretically, be defined by any value equal to or greater than one, where s = 1 denotes no purely elastic zone and s = ∞ causes the

bounding surface to operate as a classical yield surface. Figure 5.4-2 shows that increasing the value of s results in increased stiffness in the initial stress-strain response. As the elastic zone will always be contained within the bounding surface and therefore does not influence the response of states on the bounding surface, the stress-strain behavior of an overconsolidated specimen should be used to determine s.

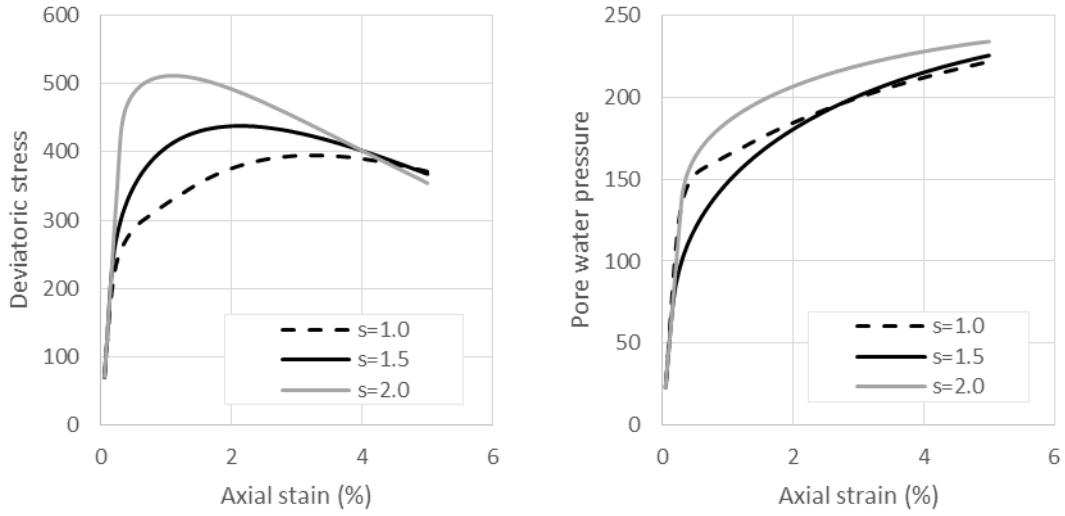

Figure 5.4-2: Effect of varying s on the predicted stress-strain and pore pressure-strain response of soil specimens at OCR=2.0 subjected to conventional undrained triaxial loading

5.4.3 Shape parameter R

The shape parameter R informs the shape of the bounding surface and size of the tension zone through designating the center of the elliptical bounding surface on the positive I axis. Mathematically, the R parameter must be assigned a value greater than 2.0; larger values will result in the center of the bounding surface being closer to the origin in I-J space. The effect of varying the R parameter is shown in Figure 5.4-3.

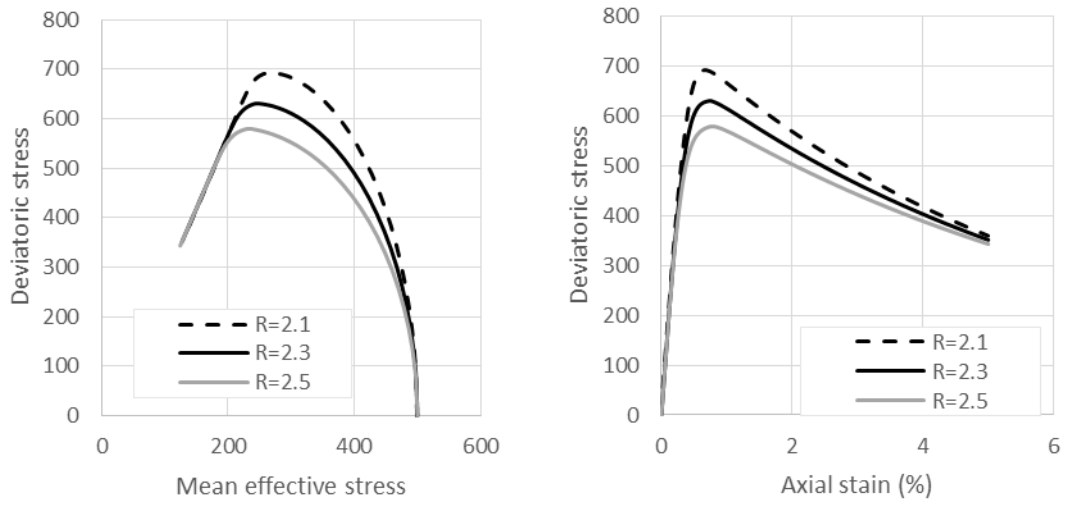

Figure 5.4-3: Effect of varying R on the predicted effective stress path and stress-strain response of soil specimens at OCR=1.0 subjected to conventional undrained triaxial loading

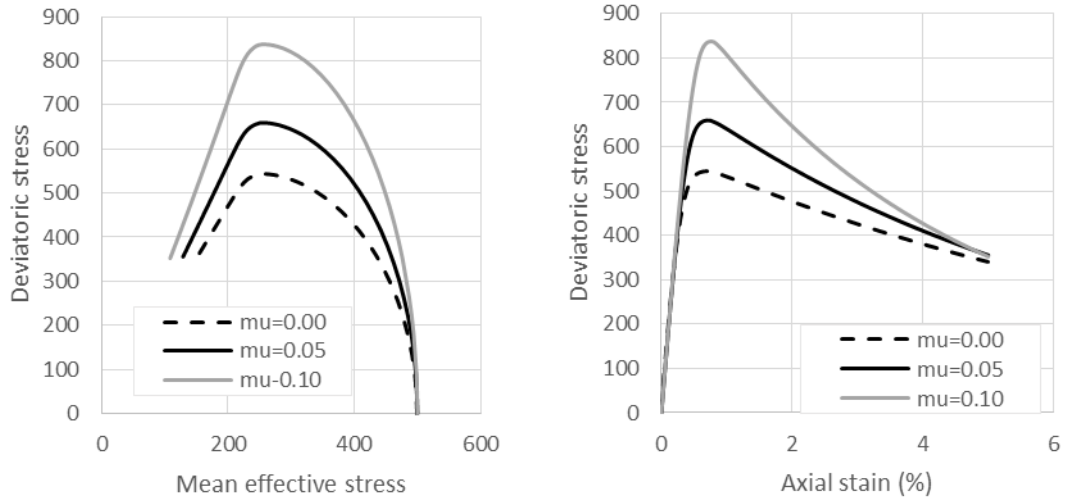

Figure 5.4-4: Effect of varying μ on the predicted effective stress path and stress-strain response of soil specimens at OCR=1.0 subjected to conventional undrained triaxial loading

5.4.4 Aspect ratio parameter μ

The μ aspect ratio parameter describes the influence the soil structure has on the peak deviatoric strength of the specimen. The value of the parameter may be set at any value greater or equal to 0.0, where zero results in no effect of destructuring on the aspect ratio of the bounding surface (i.e., the calculated critical state line). Larger values

of μ result in larger peak deviatoric stresses and larger effects of destructuring. Figure 5.4-4 demonstrates the influence of the aspect ratio parameter on normally consolidated undrained triaxial compression test predictions.

5.5 Shape hardening parameters

This set of parameters controls the amount of strain hardening or softening predicted for stress-states within the bounding surface through the hardening function, Equations 3.3-5 through 3.3-7.

5.5.1 Plastic shape hardening parameters h_c, h_e, h_0, and m

The parameters h_c and h_e are the primary shape hardening parameters, describing the stiffness of the response in triaxial compression and extension, respectively. The shape hardening parameters h_c and h_e can be assigned any value greater than zero; the bounding surface acts as a classical yield surface when $h_c = h_e = \infty$. Larger values of h_c (or h_e) result in greater values of the plastic modulus, K_p, and therefore in stiffer stress-strain response, smaller predicted volumetric strains in drained simulations or larger predicted pore water pressures in undrained simulations (Figure 5.5-1).

The exponent m in Equation 3.3-5 ensures that the h_0 parameter defines the hardening behavior in the vicinity of the I axis. The value of h_0 is traditionally set at the average of h_c and h_e in order to ensure a smooth transition when the stress point crosses the I axis. Similarly, the exponent m has typically been fixed at m = 0.02.

5.5.2 Single ellipse hardening parameters a and w

The single ellipse hardening parameters a and w determine the hardening response predicted for analyses in the heavily overconsolidated range. Variations in the

parameter ‘a’ significantly affect the stiffness exhibited in stress-strain response, as shown in Figure 5.5-2. Nieto-Leal and Kaliakin (2014) propose the w parameter should be considered fixed at w = 5.0.

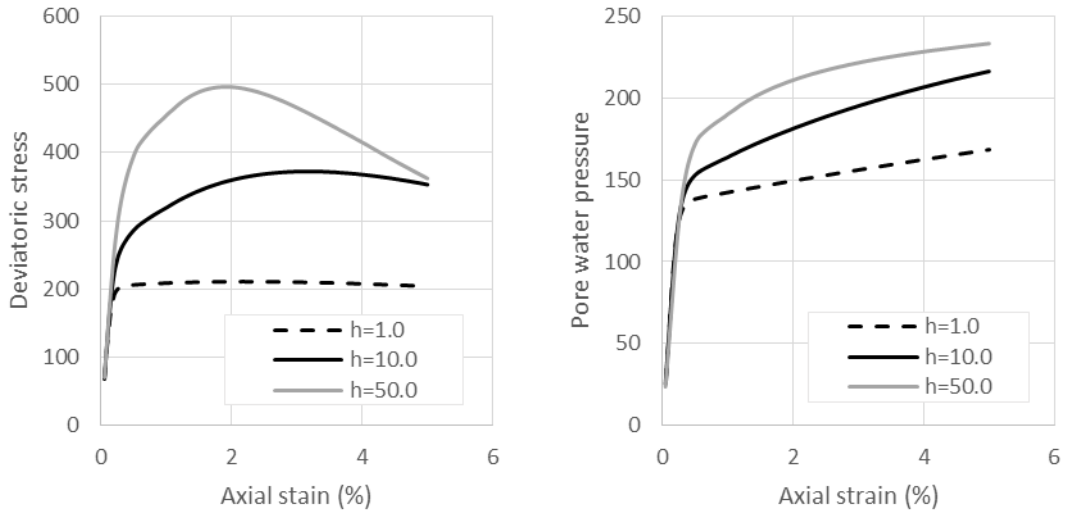

Figure 5.5-1: Effect of varying h_c on the predicted stress-strain and pore pressure-strain response of soil specimens at OCR=2.0 subjected to conventional undrained triaxial loading

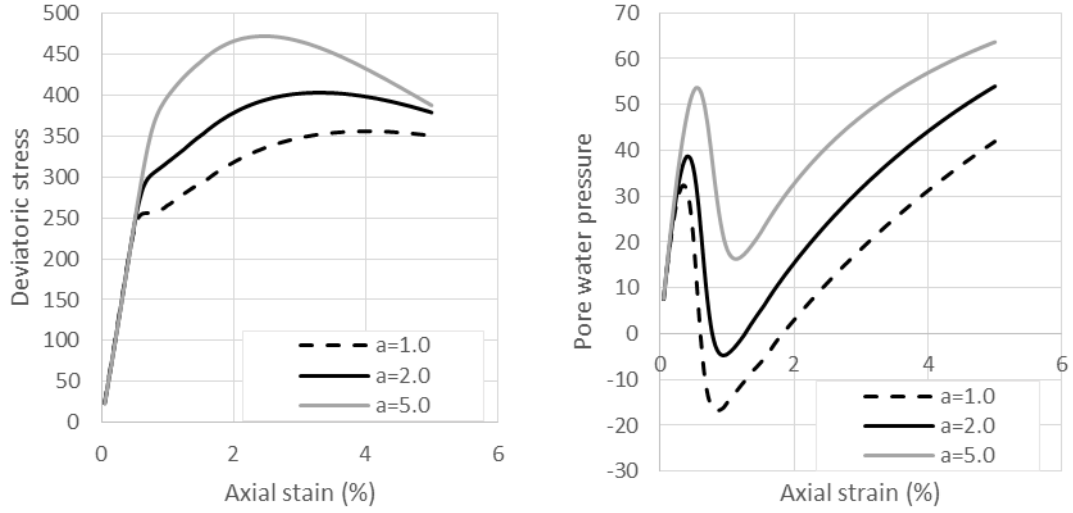

Figure 5.5-2: Effect of varying a on the predicted stress-strain and pore pressure-strain response of soil specimens at OCR=6.0 subjected to conventional undrained triaxial loading

5.6 Abbreviated guide to parameter determination

The process of determining a suitable set of model parameters should be approached systematically in order to avoid unnecessary complications and confusion. This section aims to suggest a reasonable calibration procedure and provides guidance on an appropriate range of values for each parameter.

Once the appropriate initial stress state and past stress history values have been determined for the prediction type, as discussed in Subsection 5.1.2, values of the remaining model parameters should be set to the typical values provided in Table 5.6-1 before proceeding with the calibration procedure presented in Table 5.6-2. Parameters listed within the same calibration step should be characterized one at a time.

Although no model parameters presented in this chapter can be directly defined by the cement content, or any other facet of the mix design, it is notable that a few of the model parameters loosely correlate to the amount of cement used in the mixed soil. The material parameters, κ_s and M_c^* tend to decrease and increase, respectively, with increasing cement content. Most notably, the purely theoretical μ parameter shows a strong trend toward larger values with increasing cement content (over $10\% \leq$ cement content $\leq 30\%$). Interestingly, value of μ used for the X_2-1-4 soil is less than that for the X_2-1-3 soil (see Chapter 6 for the description of the soils), despite having the same amount of cement in the mixed soil. Miura et al. (2001) state that the behavior of cement-mixed soils depends on a number of factors, but that cement and total water contents play key roles; greater cement contents results in larger yield stresses, while greater total water contents does the opposite.

Table 5.6-1: Typical values for model parameters

Initial state parameters	Typical Value	Range of Values
S_i	35.0	5.0 – 100.0
Elastoplastic model parameters	**Typical Value**	**Range of Values**
λ_u	0.20	0.10 – 0.30
κ_s	0.015	0.01 – 0.03
M_c*	2.4	2.2 – 2.6
M_e*/M_c*	0.2	0.1 – 0.5
ν	0.2	0.15 – 0.3
P_L†	$P_{atm}/3$	$P_{atm}/3$
Destructuring parameters	**Typical Value**	**Range of Values**
δ	2.69	1.1 – 3.7
π	2.69	1.0 – 5.0
Surface configuration parameters	**Typical Value**	**Range of Values**
c	0.3	0.0 – 0.5
s	1.2	1.0 – 2.0
R	2.2	2.1 – 2.4
μ	0.05	0.0 – 0.1
Hardening parameters	**Typical Value**	**Range of Values**
m†	0.02	0.02
h_c	15.0	5.0 – 100.0
h_e	15.0	3.0 – 100.0
h_0†	$(h_c + h_e)/2$	---------
a	2.0	1.0 – 5.0
w†	5.0	5.0

† Parameters considered fixed values as indicated.

Table 5.6-2: Overview of suggested calibration procedure

Step	Parameters determined	Methodology
1	S_i	Directly from comparison of structured and remolded consolidation test results
	λ_u	Directly from remolded consolidation test
	κ_s	Directly from structured consolidation test
	M_c*	Directly from set of triaxial compression tests
	M_e*	Directly from set of triaxial extension tests
	G or ν	Adopt a standard value from the literature
2	δ	Curve-fitted to structured consolidation test or directly from consolidation test results
3	μ	Curve-fitted to NC triaxial compression test
	π	Curve-fitted to NC triaxial compression test
	R	Curve-fitted to NC triaxial compression test
4	c	Curve-fitted to lightly OC triaxial compression test
5	h_c	Curve-fitted to lightly OC triaxial compression test
	h_e	Curve-fitted to lightly OC triaxial extension test
6	s	Curve-fitted to lightly OC triaxial compression test
7	a	Curve-fitted to heavily OC triaxial compression test

Chapter 6: Predictions

The proposed model's ability to predict the stress-strain behavior of cement-mixed clay specimens under monotonic and cyclic loading is investigated. First, model predictions using the cohesion and variable R parameter defined bounding surface and the final proposed form of the bounding surface (detailed in Subsections 3.4.3 and 3.5.2, respectively) are compared. Then a fuller set of model predictions using the final proposed model formulation is presented. In the case of monotonic loading behavior, a comparison of predictions and published laboratory test results validate the model formulation. Model predictions will also be presented to demonstrate the model's ability to predict evolution of the stress-strain response over a number of cycles.

6.1 Soils and laboratory tests used for model validation

A large amount of data exists on the monotonic stress-strain response of cement-improved cohesive soils. However, "fully-developed" data sets; i.e., those containing triaxial tests over large ranges of confining pressures and consolidation tests for both structured and unstructured soil samples, are not common in the literature. The comparisons presented herein are based on datasets published by Xiao et al. (2016), Xiao and Lee (2014), and Quiroga et al. (2017) on specimens with cement contents ranging between ten to fifty percent. Table 6.1-1 shows an overview of the prediction comparisons for each of the six cement-mixed soils used in this chapter. A note on the soil-type nomenclature scheme: the leading letter refers to the source of the test data and the numbers denote the soil-cement-water proportions in the mix determined by weight. The cement contents and total water contents for each soil type are provided in Table 6.1-2. Test data for all X-designated soils were presented by both Xiao and Lee (2014)

Table 6.1-1: Overview of predictions for each soil type

Category	X_10-1-11	X_5-1-6	X_10-3-13	X_2-1-3	X_2-1-4	Q_10-2-5
NC specimens	CD 500 CD 1000	CU 500 CU 1000 CU 1500 CD 500 CD 1000	CU 750 CU 1250 CU 1500	CD 1025	CU 500 CU 1000 CU 1500 CD 500 CD 1000	---
OC specimens	CU 300-150 CU 500-250 CU 1000-500 CU 1500-750 CD 300-150 CD 500-250 CD 1000-500 CD 2500-1250	CU 500-250 CU 1000-500 CU 1500-750 CU 2000-1000 CD 380-190 CD 1000-500 CD 1500-750 CD 2500-1250	CU 1000-500 CU 1500-750 CU 2000-1000 CD 1000-500 CD 1500-750 CD 2000-1000 CD 2500-1250	CU 1500-750 CU 2000-1000 CD 1500-750 CD 2000-1000 CD 2500-1250	CU 500-250 CU 1000-500 CU 1500-750 CU 2000-1000 CD 500-250 CD 1000-500 CD 1500-750 CD 2000-1000 CD 2500-1250	---
PY specimens	---	CD 200	CU 350 CD 500	CU 500 CD 450	CD 250	CU 207 CU 120 CU 41
Consolidation	Isotropic	Isotropic	Isotropic	Isotropic	Isotropic	Oedometer

Key: CD = drained triaxial compression test; CU = undrained triaxial compression test
NC = normally consolidated; OC = overconsolidated; PY = pre-yield; For NC and PY tests, the number designates confining stress in kPa.
For OC specimens, the numbers designate precompression pressure – confining stress in kPa, respectively.

(isotropic consolidation data) and Xiao et al. (2016) (drained and undrained triaxial compression data). Results for identical soils are presented as a single dataset herein.

Table 6.1-2: Mix design for model comparison soils

	Cement contents (%)	Total water content (%)	Curing time (days)
X_10-1-11	10	100	7
X_5-1-6	20	100	7
X_10-3-13	30	100	7
X_2-1-3	50	100	7
X_2-1-4	50	133	7
Q_10-2-5	20	41	60

Note: Data on X-soils reproduced from Xiao and Lee (2014) and Xiao et al. (2016); data on Q-soil reproduced from Quiroga et al. (2017).

6.2 Comparison of model predictions using two bounding surface equations

The two disparate equations for the bounding surface depend on two similar sets of model parameters. In particular, the final bounding surface formulation requires characterization of the M_c^*, M_e^*/M_c^*, μ, and R parameters, as discussed in Chapter 5; conversely defining the bounding surface through the cohesion intercept required characterization of the M_c, M_e/M_c, UCS, A, C_e/C_c, and ζ parameters, defined in the following subsection.

6.2.1 Parameters for cohesion-based single-ellipse bounding surface model

The slope of the critical state lines in q-p′ space in compression and extension (M_c and M_e, respectively) are equivalent to the starred values (i.e., final or large strain values) used in the final proposed model formulation.

Unconfined compression strength, UCS, and a cohesion scale factor, A, are used to determine the initial cohesion value. The customary analysis of unconfined compression tests for purely cohesive soils states that cohesion is UCS/2, however Xiao et al. (2016) suggest cohesion for a chemically stabilized marine clay may be better represented as UCS/3. In order to allow flexibility within the model formulation, the initial cohesion in compression in triaxial stress-space is calculated as:

$$C_{i,comp} = {UCS}/{A} \qquad \textbf{6.2-1}$$

The value of C_e/C_c defines the relationship between the cohesion intercepts in triaxial extension and compression.

The cohesion degradation parameter, ζ, relates the change in cohesion to the change in sensitivity. Xiao et al. (2016) state that $\zeta = 0.28$ adequately characterizes the change in cohesion, via Equations 3.4-9 and 3.4-12, for a set of cement-treated soils with cement contents ranging from 10-50% (by dry weight) and total water content between 100-133%.

6.2.2 Selected model predictions

Updating the equation of the bounding surface generally increased the predictive capabilities of the proposed model formulation. The largest increases in agreement between prediction and test data were noted for triaxial tests on normally consolidated specimens. For the sake of brevity, only one set of compared model predictions is presented (Figure 6.2-1); although this trend was evident with all of the soil types used in this study. Model parameters used in these simulations are presented in Table 6.2-1 and Table 6.3-2.

a)

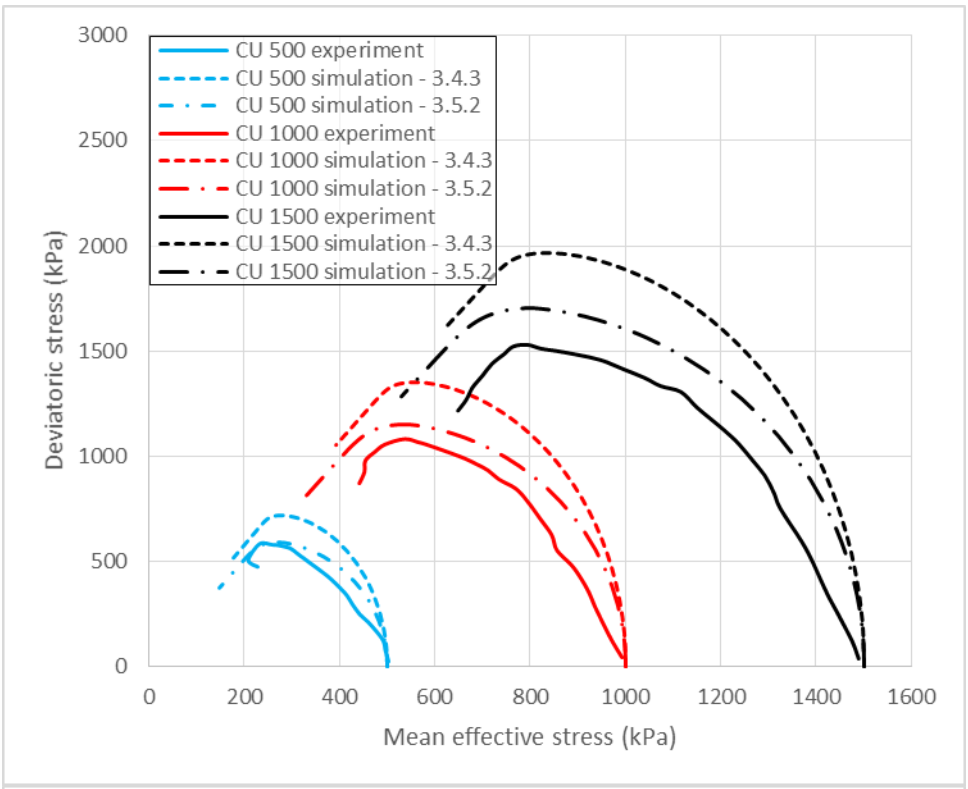

b)

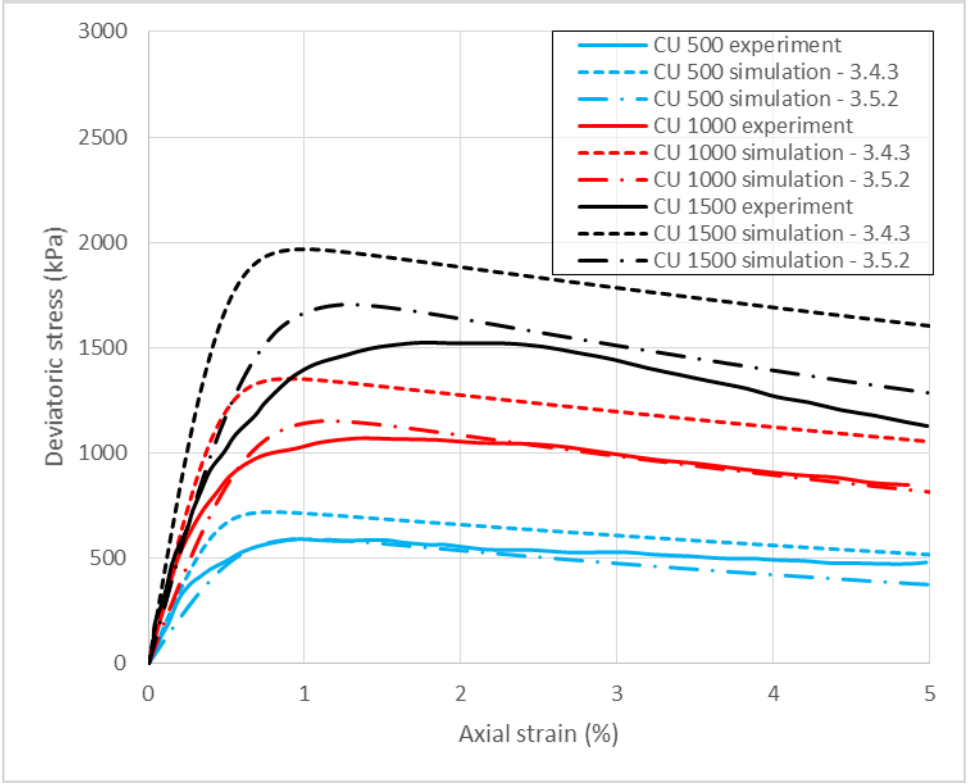

Figure 6.2-1: Comparison of model simulations of undrained shear behavior of normally consolidated X_5-1-6 soil specimens using bounding surface formulations from Subsections 3.4.3 and 3.5.2: (a) mean effective stress versus deviatoric stress, and (b) axial strain versus deviatoric stress

Table 6.2-1: Bounding surface model parameters for X_5-1-6 soil model predictions using Subsection 3.4.3 bounding surface

Parameter	Value	Parameter	Value	Parameter	Value
e_{in}	2.445	κ_s	0.020	**c**	0.5
p'_0 **(kPa)**	370	M_c	2.36	**s**	2.00
UCS (kPa)	300	M_e/M_c	1.0	h_c	55.0
C_e/C_c	1.0	**ν**	0.3	h_e/h_c	1.0
A	3.0	**δ**	2.69	**a**	2.0
S_i	54.63	**π**	1.69		
λ_u	0.230	ζ	0.28		

The remainder of this chapter presents and discusses predictions made with the actual proposed model formulation (i.e., using the bounding surface detailed in Subsection 3.5.2).

6.3 Predictions of monotonic response

The method for calibrating model parameters outlined in Chapter 5 was followed as closely as possible for each soil type. However, from Table 6.1-1 it is evident that none of the data sets include all of the tests required by the calibration procedure. The modifications taken will be detailed in discussing the individual soil predictions.

Values of initial void ratio, p'_0, S_i, λ_u, κ_s, M_c^*, and δ for X-soils are adopted from Xiao and Lee (2014) and Xiao et al. (2016). Values of M_e^*/M_c^* and h_e/h_c are set to one in the absence of triaxial extension data. It is important to note that for all normally consolidated and overconsolidated tests, the change in initial sensitivity and void ratio was calculated and directly specified accordingly, as discussed in Subsection 5.1.2.

Specific tests used to calibrate model parameters for X-soil predictions are detailed in Table 6.3-1.

Values of initial void ratio, p'_0, λ_u, κ_s, and M_c^* for Q_10-2-5 soils are adopted from Quiroga et al. (2017) and initial sensitivity is determined from improved and unimproved soil oedometer tests. Values of M_e^*/M_c^* and h_e/h_c are set to one in the absence of triaxial extension data. Although the results of an isotropic model predicting anisotropic consolidation behavior is questionable, oedometer test data was used to determine δ and a starting value of π. The CU 207 (PY) test was used to finalize the value of π and the remaining model parameters.

A list of the model parameters used for each soil type can be found in Table 6.3-2. Figure 6.3-1 shows the predictions of X-soil isotropic consolidation tests. Predictions of drained and undrained triaxial compression test results for various X-soils are shown in Figure 6.3-2 through Figure 6.3-19. Oedometer test predictions for the Q-soil are shown in Figure 6.3-20. Figure 6.3-21 shows the predictions of Q-soil undrained triaxial compression test results. A single set of parameters are used to predict all the test results for a given soil.

Table 6.3-1: Tests used to calibrate X-soil curve-fitted parameters

	NC parameters (π)	Lightly OC parameters (c, s, h_c)	Heavily OC parameters (a)
X_10-1-11	CD 500	CU 500-250	---
X_5-1-6	CU 500	CU 500-250	---
X_10-3-13	CU 500	CU 350 (PY)	---
X_2-1-3	CD 1025	CU 500 (PY)	---
X_2-1-4	CU 500	CU 500-250	---

Table 6.3-2: Bounding surface model parameters for all soil types

Parameter	X_10-1-11	X_5-1-6	X_10-3-13	X_2-1-3	X_2-1-4	Q_10-2-5
e_{in}	2.539	2.445	2.364	2.249	3.033	0.910
p'_0 (kPa)	217	370	654	1025	439	1500
S_i	238.33	54.63	24.01	5.47	28.85	11.45
$\lambda_{\nu i}$	0.200	0.230	0.250	0.285	0.300	0.104
κ_s	0.025	0.020	0.019	0.013	0.013	0.007
M_c*	2.26	2.36	2.38	2.42	2.53	2.33
M_e/M_c*	1.0	1.0	1.0	1.0	1.0	1.0
ν	0.3	0.3	0.3	0.3	0.3	0.3
R	2.15	2.20	2.15	2.20	2.20	2.20
δ	3.35	2.69	2.55	2.40	2.00	4.20
π	4.35	2.69	2.65	3.40	1.71	4.20
μ	0.02	0.03	0.08	0.06	0.03	0.03
c	0.5	0.5	0.5	0.5	0.5	0.5
s	1.10	1.30	1.10	1.25	1.20	1.20
h_c	55.0	45.0	35.0	45.0	35.0	65.0
h_e/h_c	1.0	1.0	1.0	1.0	1.0	1.0
a	2.0	2.0	2.0	2.0	2.0	15.0

a)

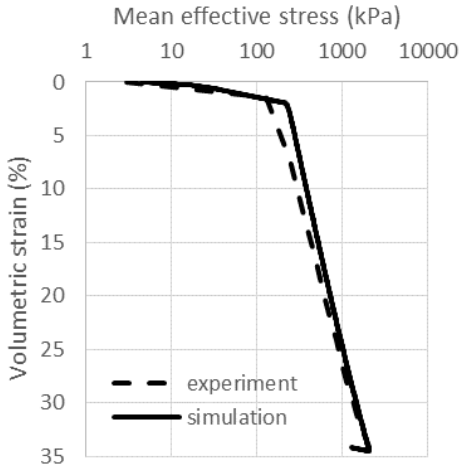

b)

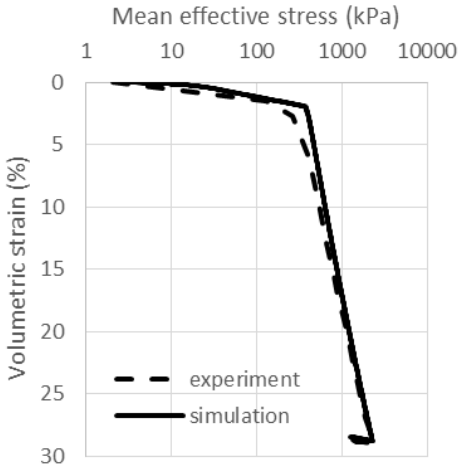

c)

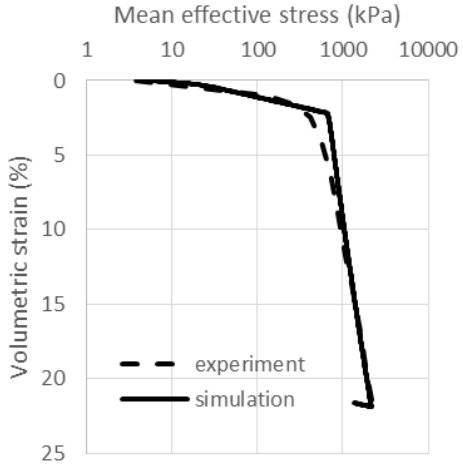

d)

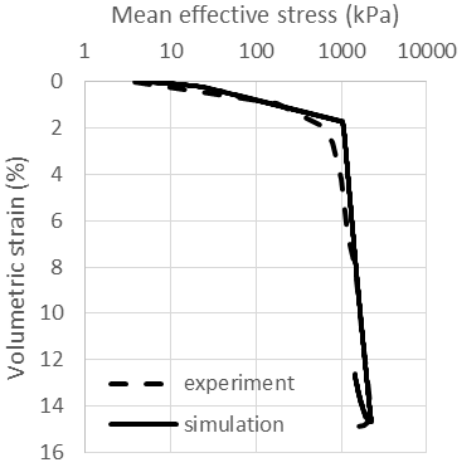

e)

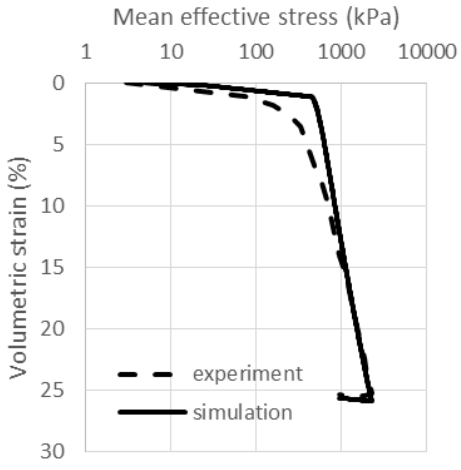

Figure 6.3-1: Simulation of isotropic consolidation behavior of (a) X_10-1-11, (b) X_5-1-6, (c) X_10-3-13, (d) X_2-1-3, and (e) X_2-1-4 soil specimens

a)

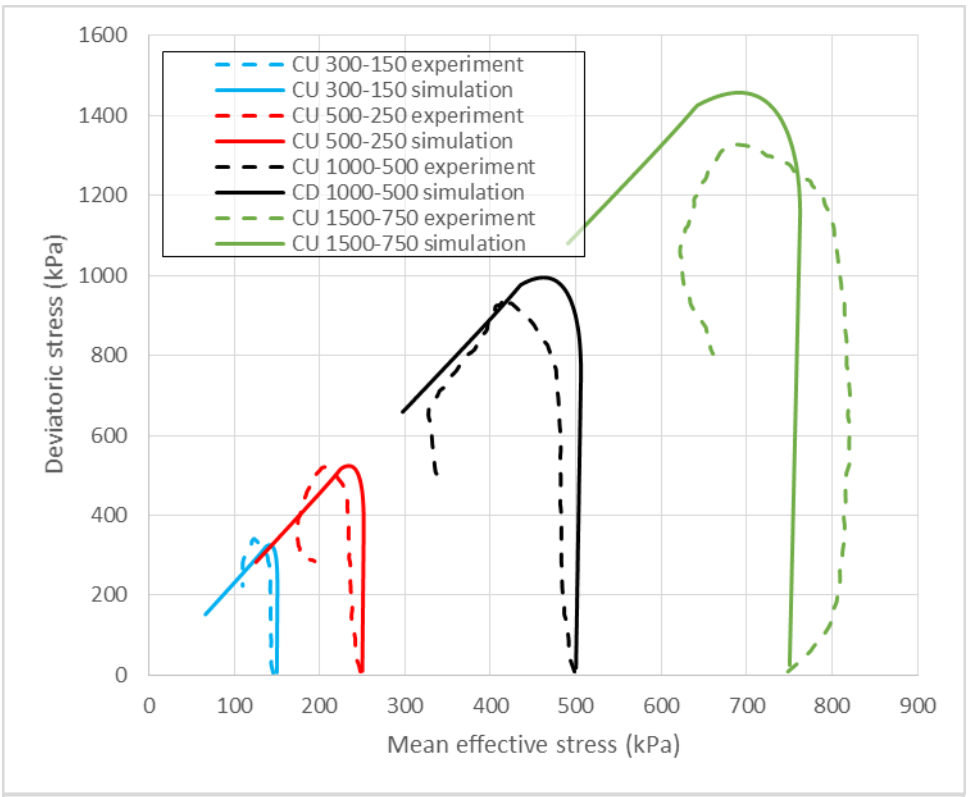

b)

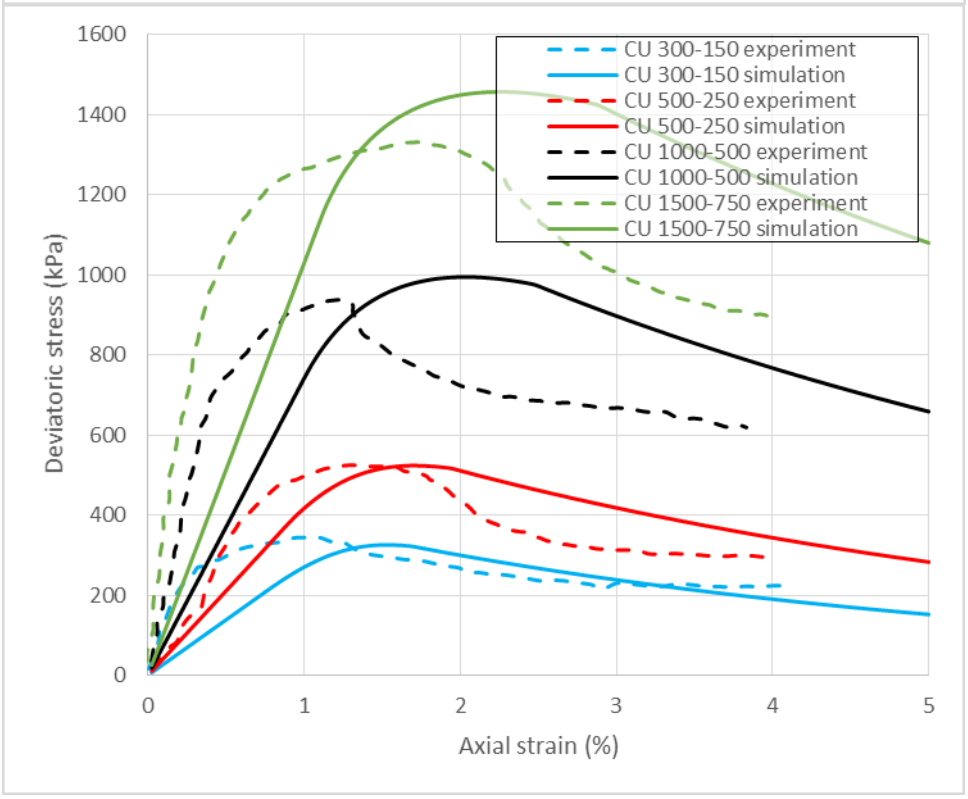

Figure 6.3-2: Simulation of undrained shear behavior of overconsolidated X_10-1-11 soil specimens: (a) mean effective stress versus deviatoric stress, and (b) axial strain versus deviatoric stress

a)

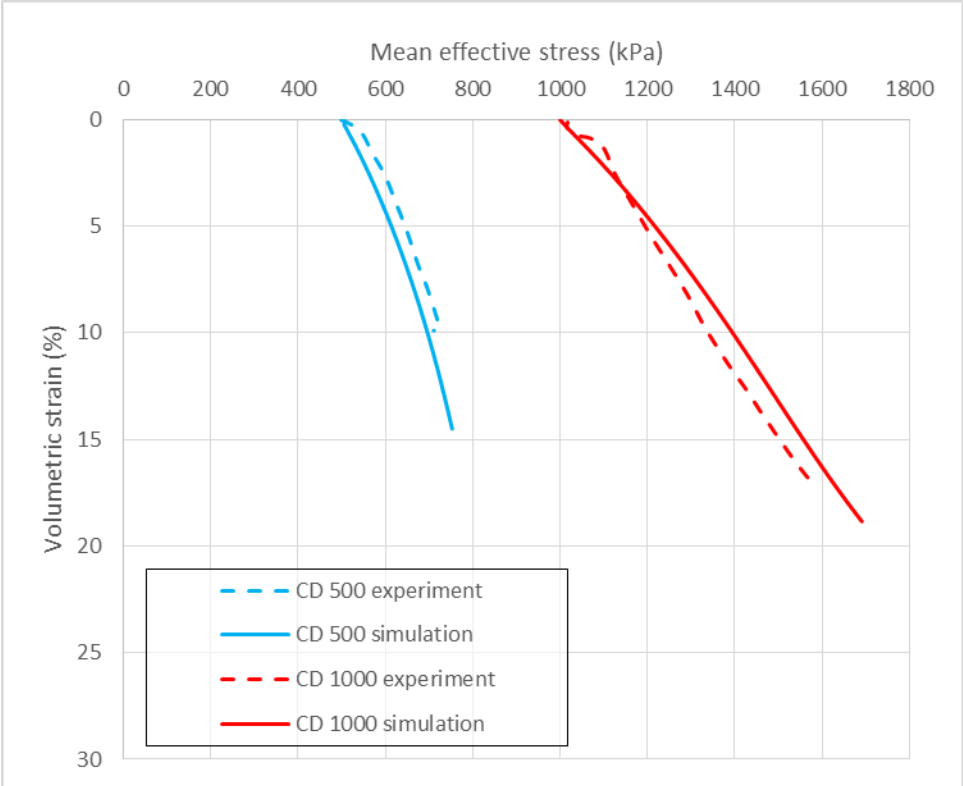

b)

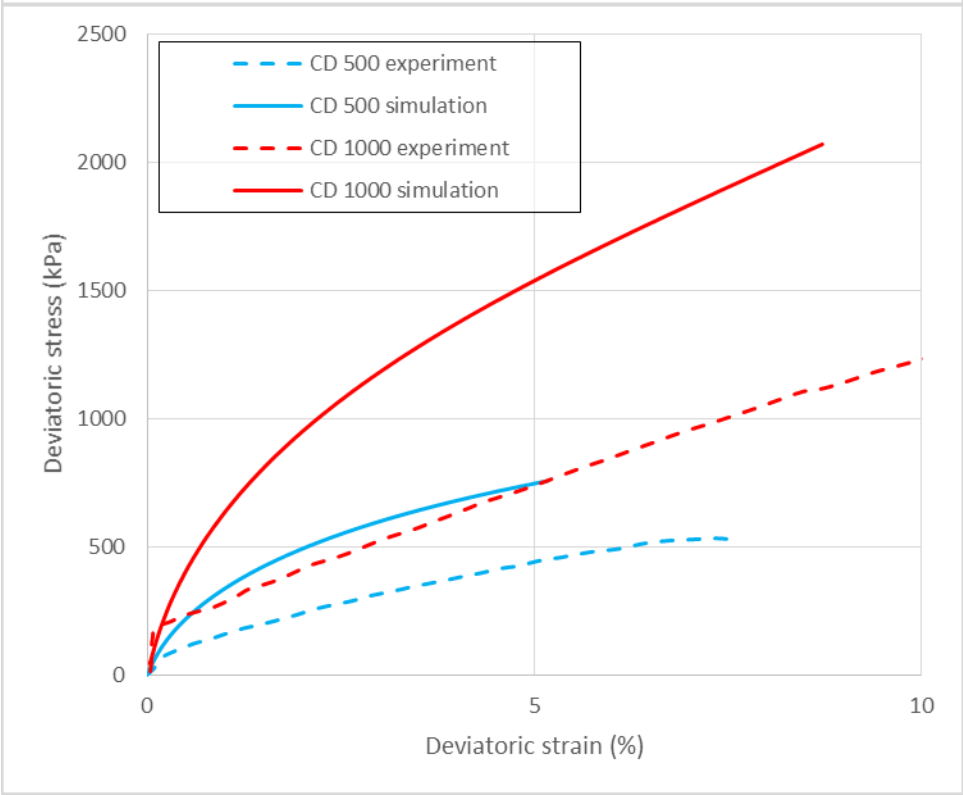

Figure 6.3-3: Simulation of drained shear behavior of normally consolidated X_10-1-11 soil specimens: (a) mean effective stress versus volumetric strain, and (b) deviatoric strain versus deviatoric stress

a)

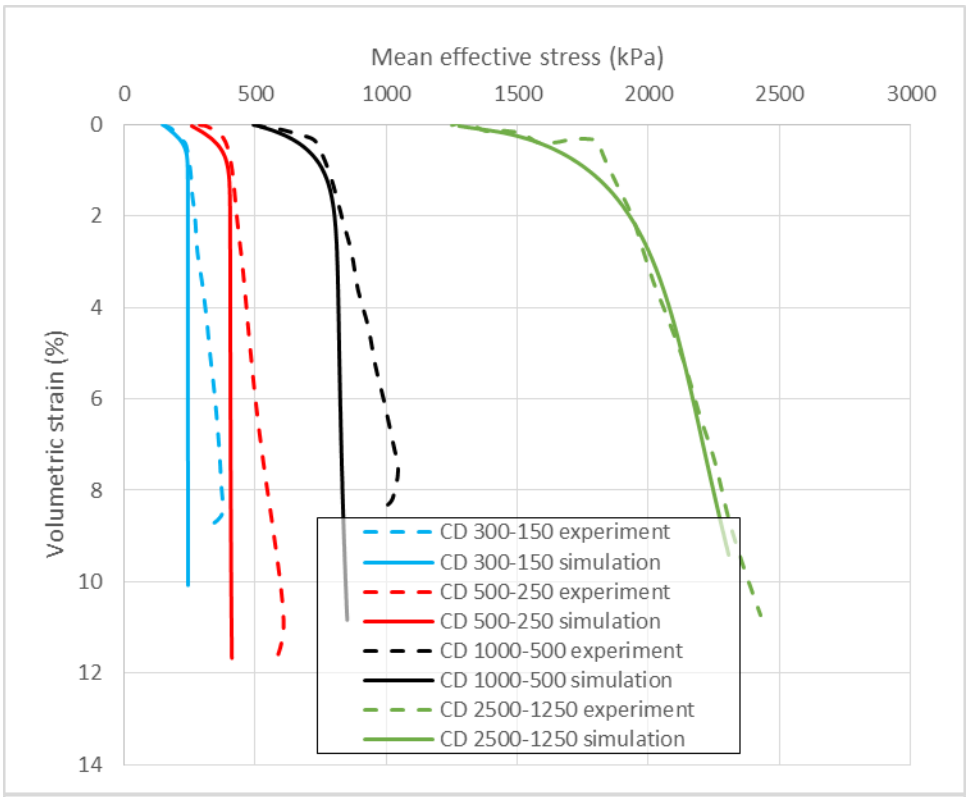

b)

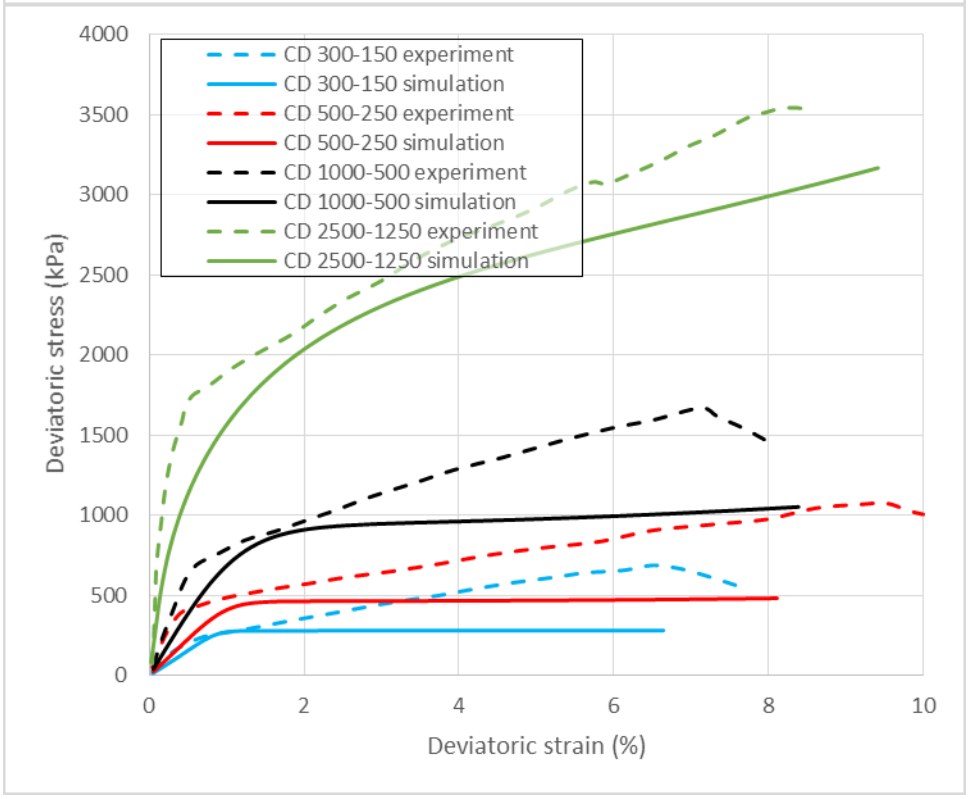

Figure 6.3-4: Simulation of drained shear behavior of overconsolidated X_10-1-11 soil specimens: (a) mean effective stress versus volumetric strain, and (b) deviatoric strain versus deviatoric stress

a)

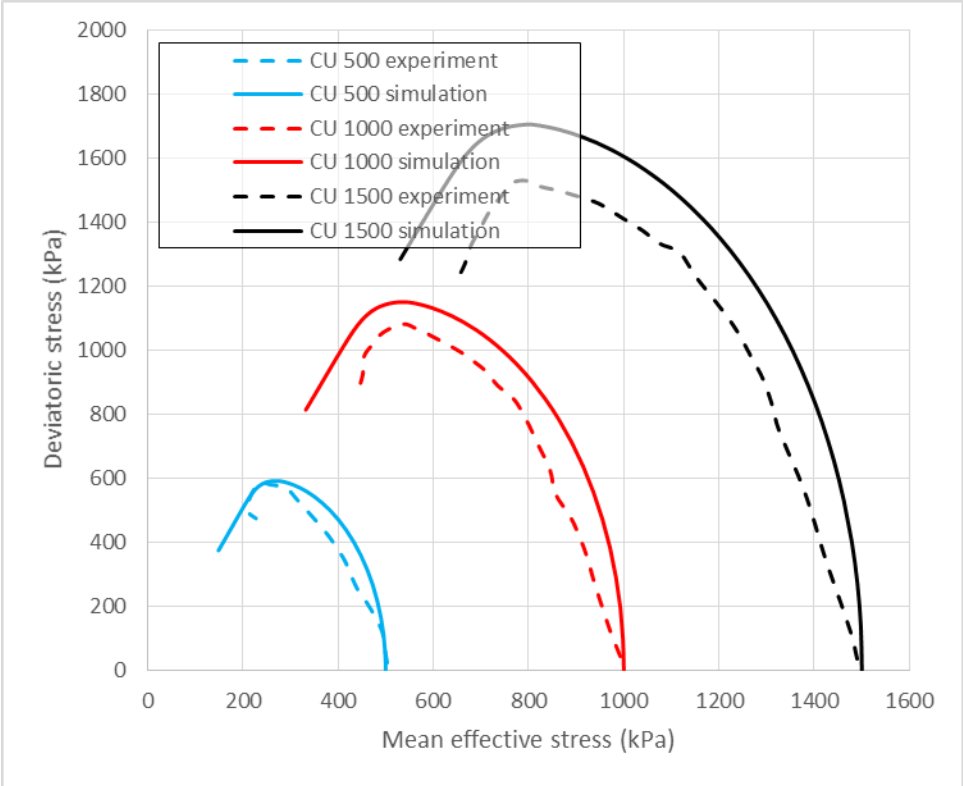

b)

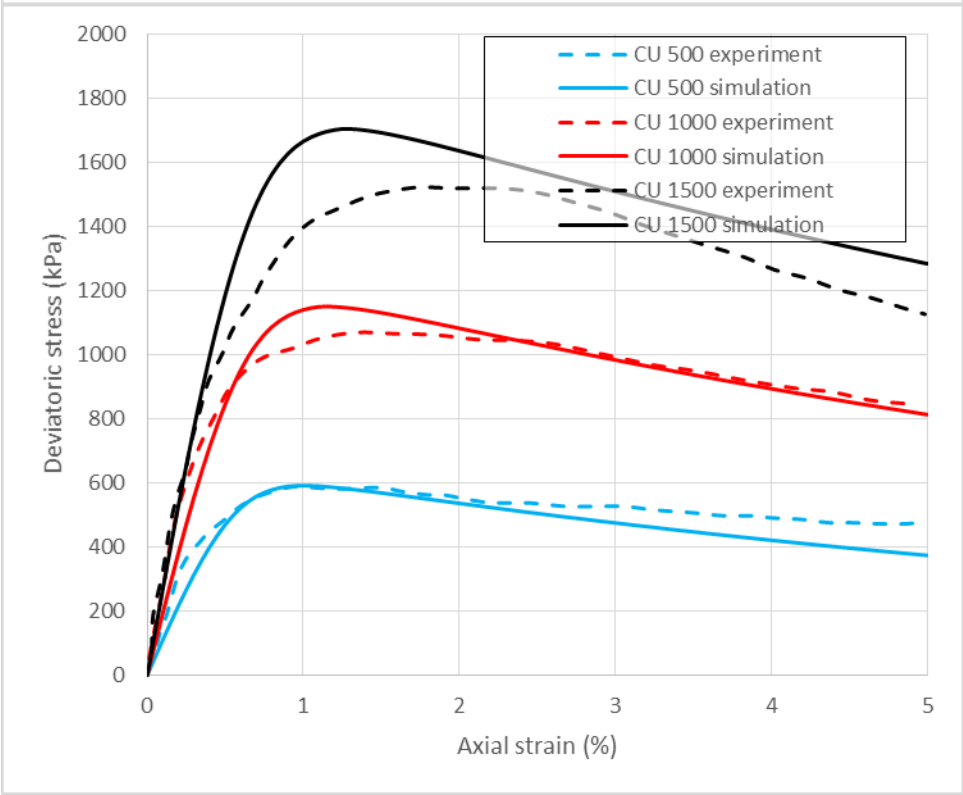

Figure 6.3-5: Simulation of undrained shear behavior of normally consolidated X_5-1-6 soil specimens: (a) mean effective stress versus deviatoric stress, and (b) axial strain versus deviatoric stress

a)

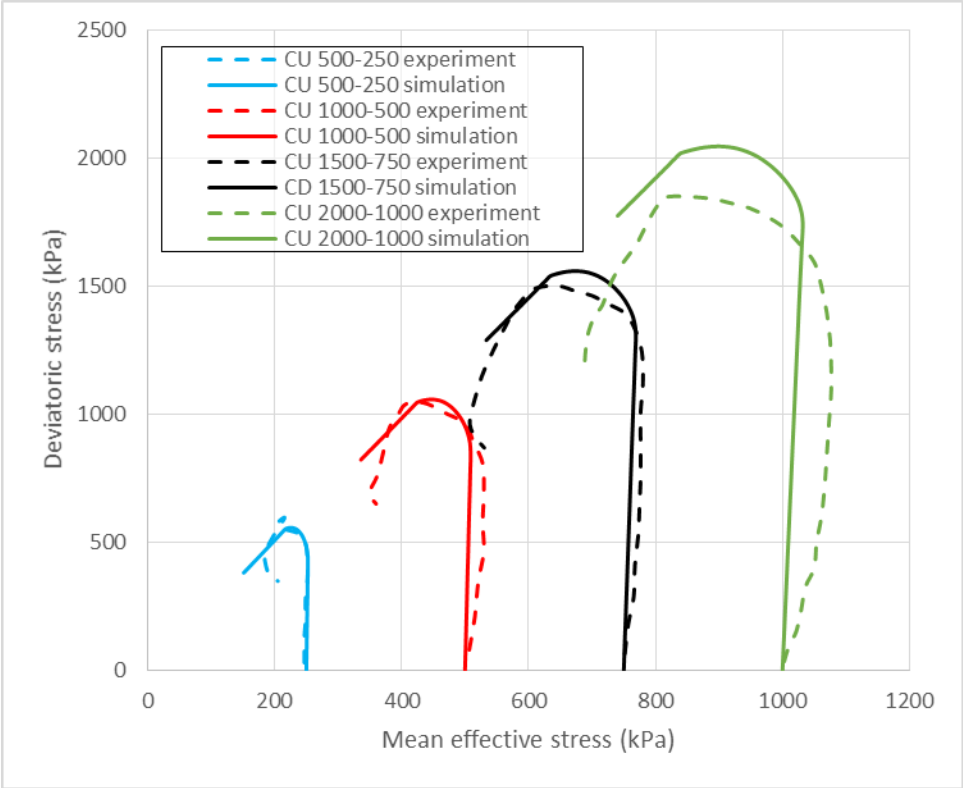

b)

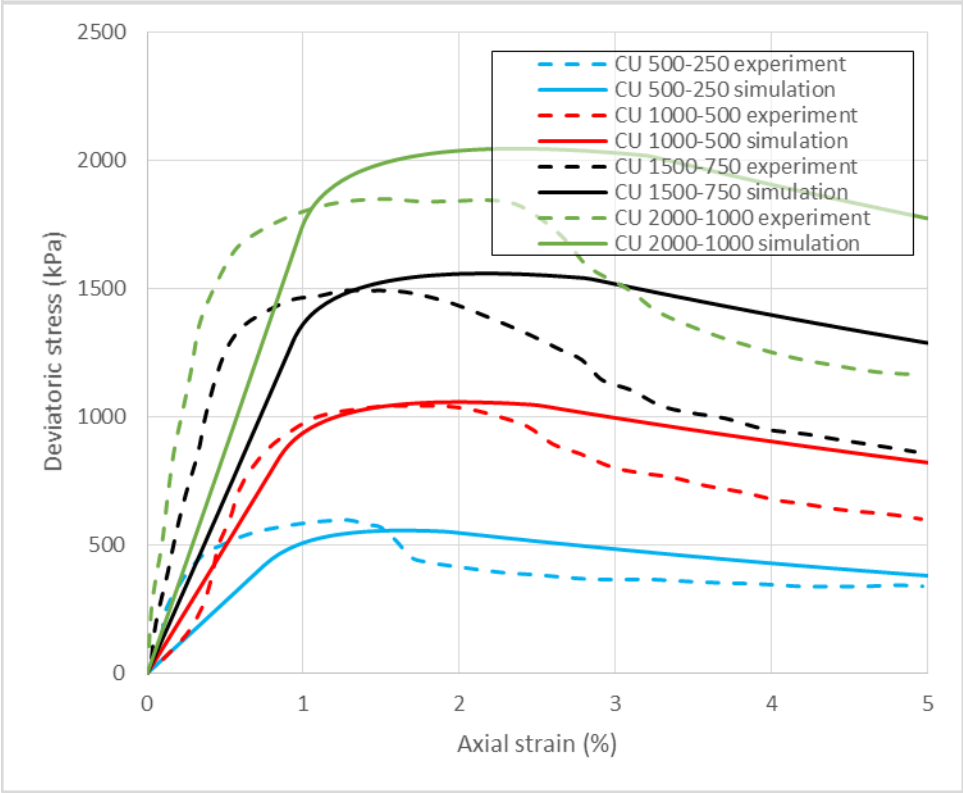

Figure 6.3-6: Simulation of undrained shear behavior of overconsolidated X_5-1-6 soil specimens: (a) mean effective stress versus deviatoric stress, and (b) axial strain versus deviatoric stress

a)

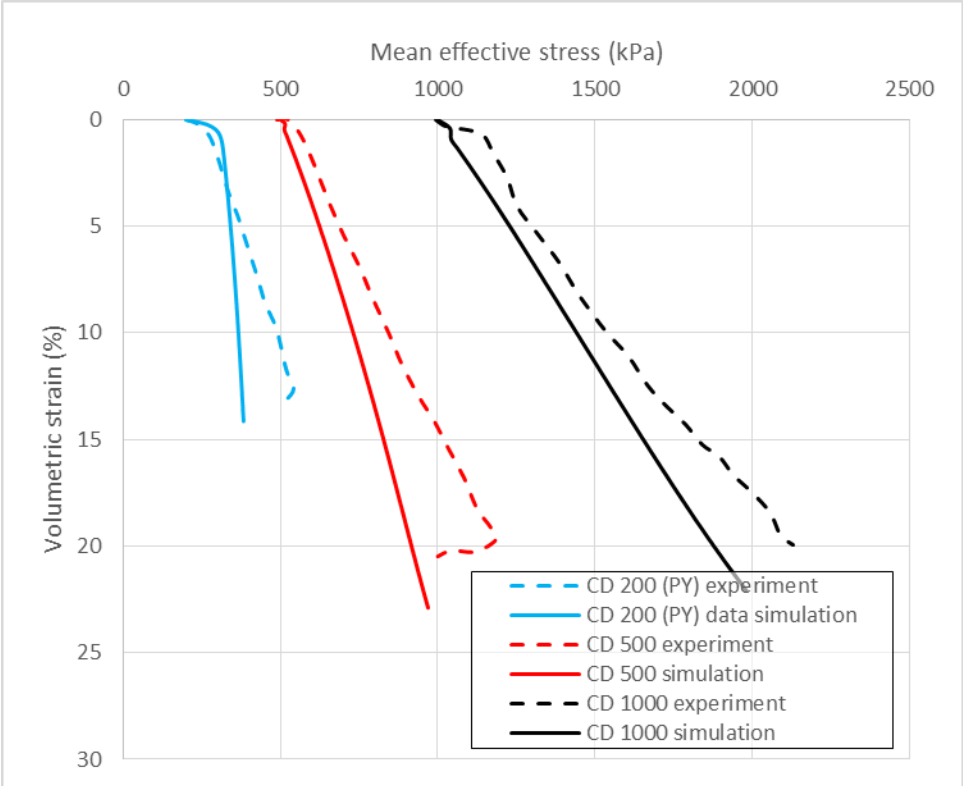

b)

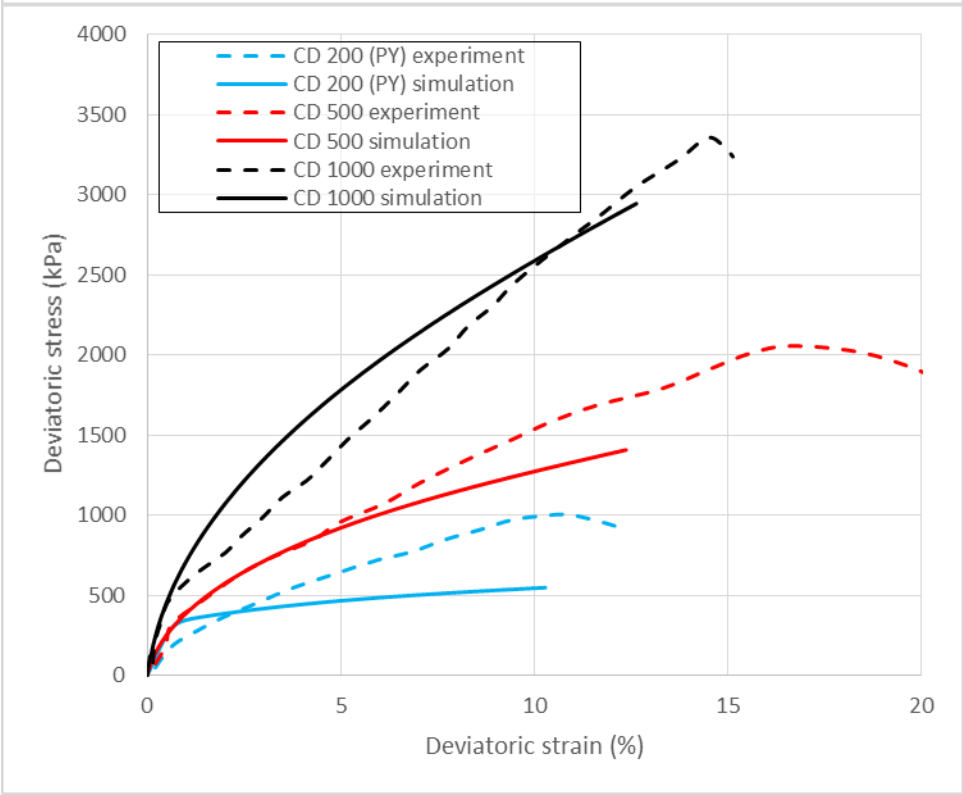

Figure 6.3-7: Simulation of drained shear behavior of normally consolidated and pre-yield (PY) X_5-1-6 soil specimens: (a) mean effective stress versus volumetric strain, and (b) deviatoric strain versus deviatoric stress

a)

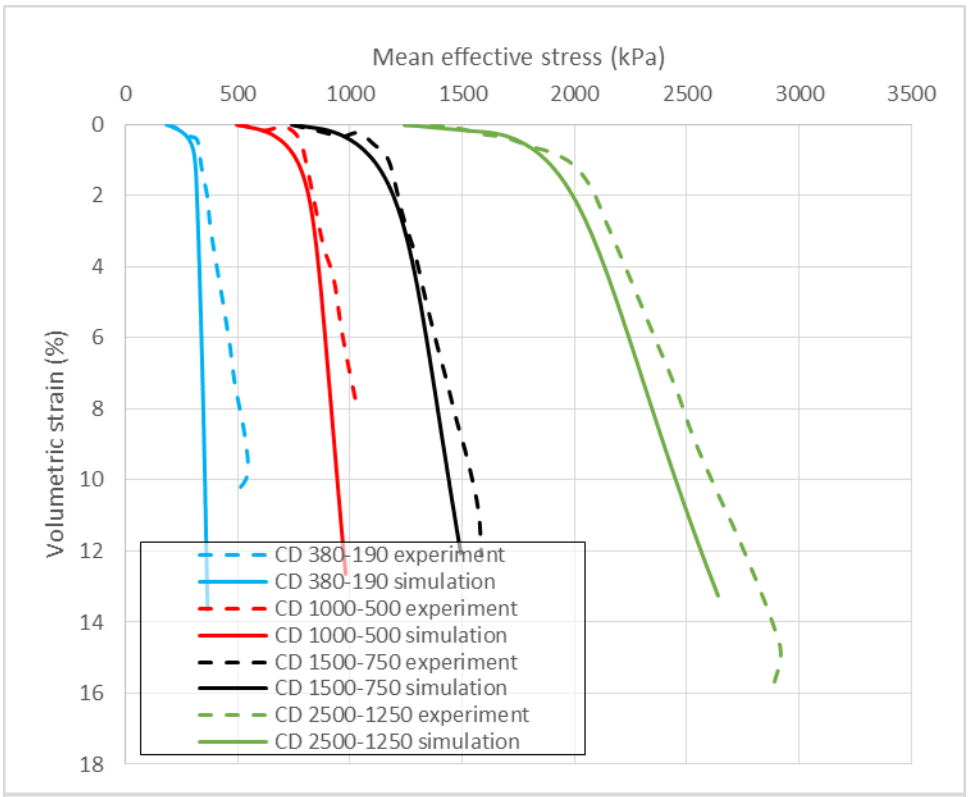

b)

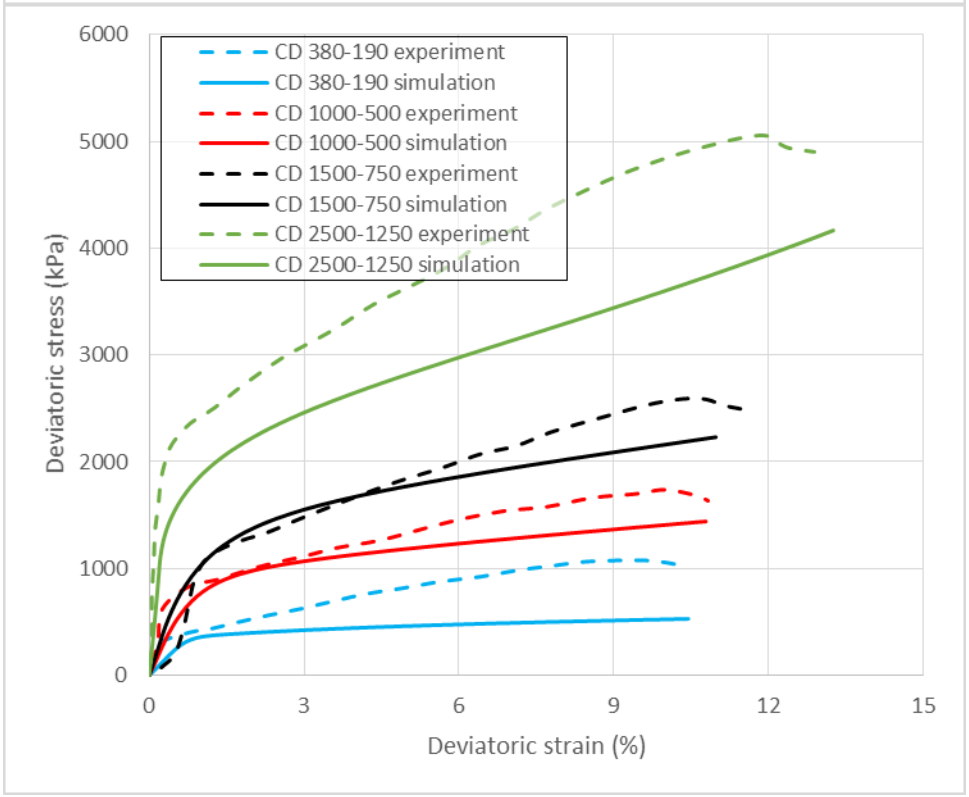

Figure 6.3-8: Simulation of drained shear behavior of overconsolidated X_5-1-6 soil specimens: (a) mean effective stress versus volumetric strain, and (b) deviatoric strain versus deviatoric stress

a)

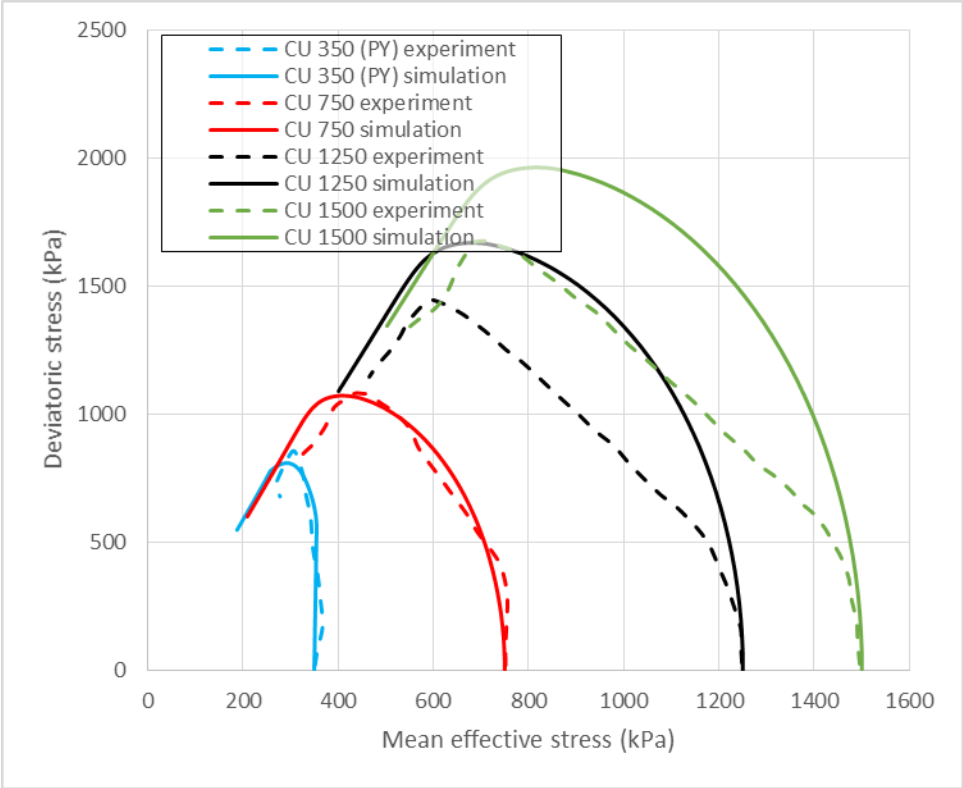

b)

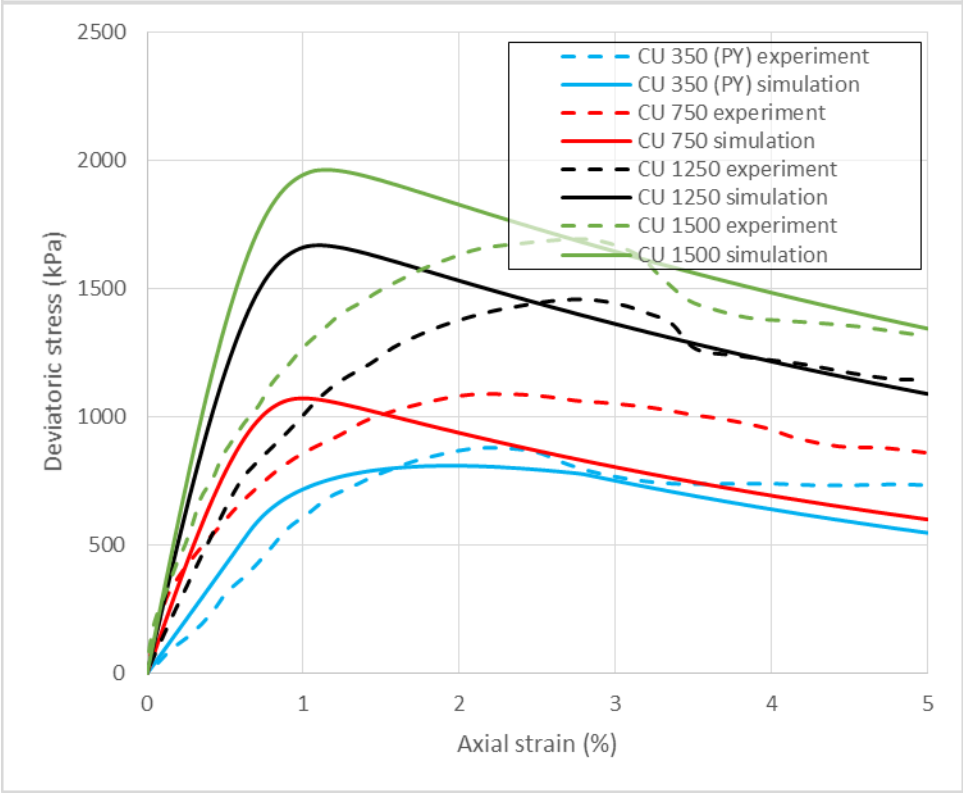

Figure 6.3-9: Simulation of undrained shear behavior of normally consolidated and pre-yield (PY) X_10-3-13 soil specimens: (a) mean effective stress versus deviatoric stress, and (b) axial strain versus deviatoric stress

a)

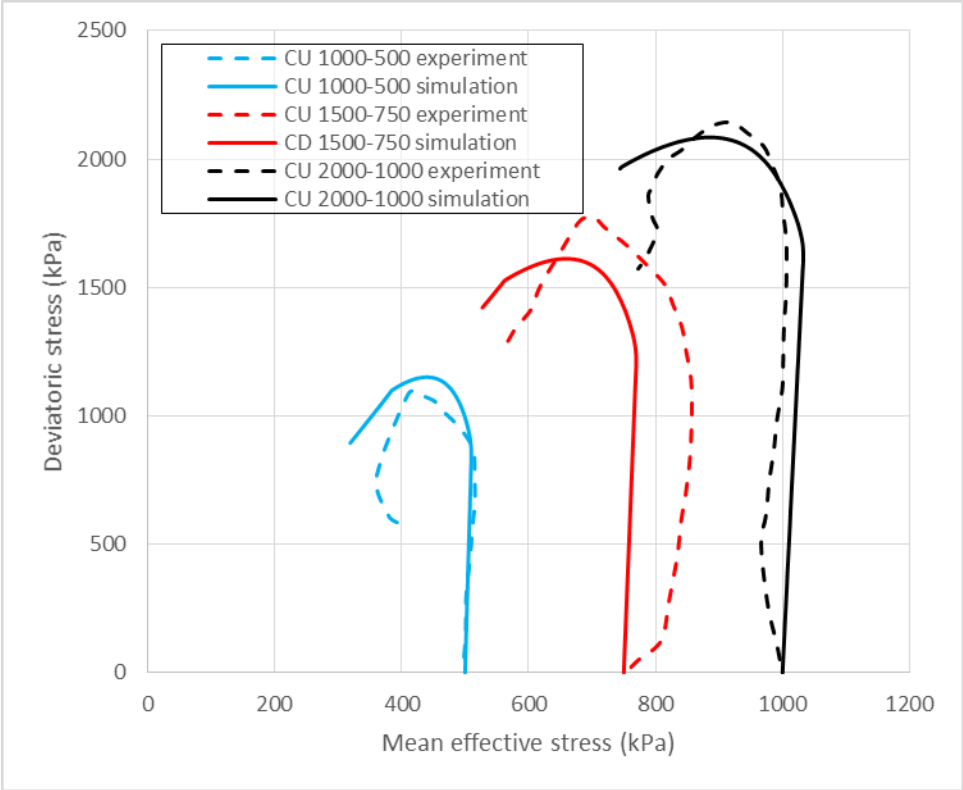

b)

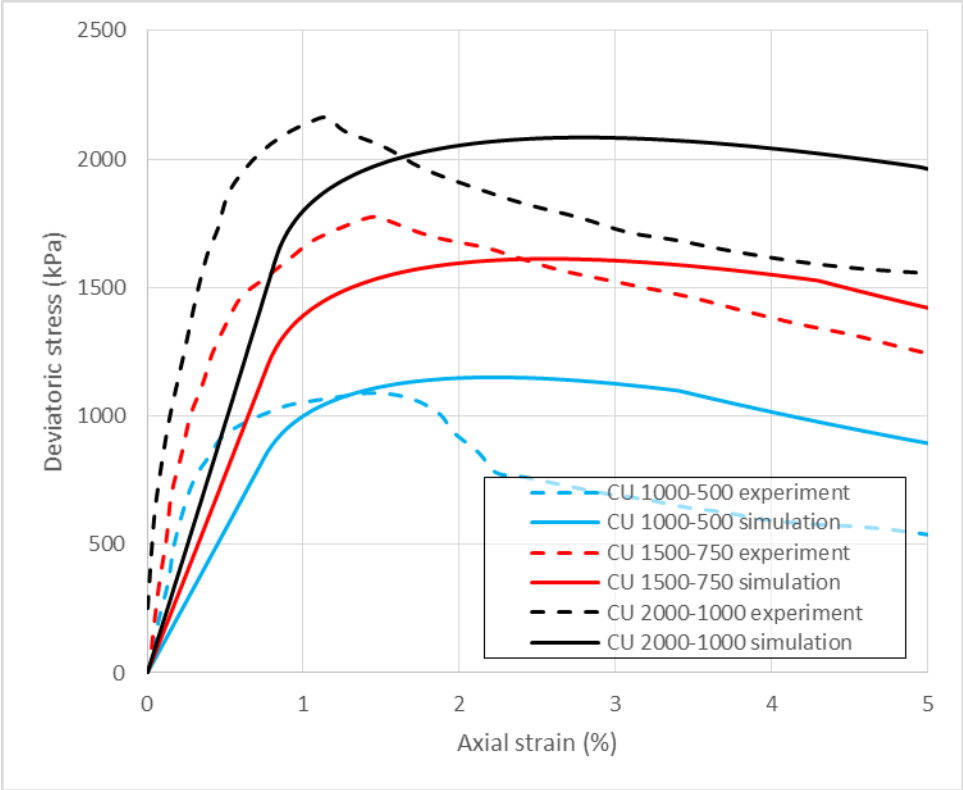

Figure 6.3-10: Simulation of undrained shear behavior of overconsolidated X_10-3-13 soil specimens: (a) mean effective stress versus deviatoric stress, and (b) axial strain versus deviatoric stress

a)

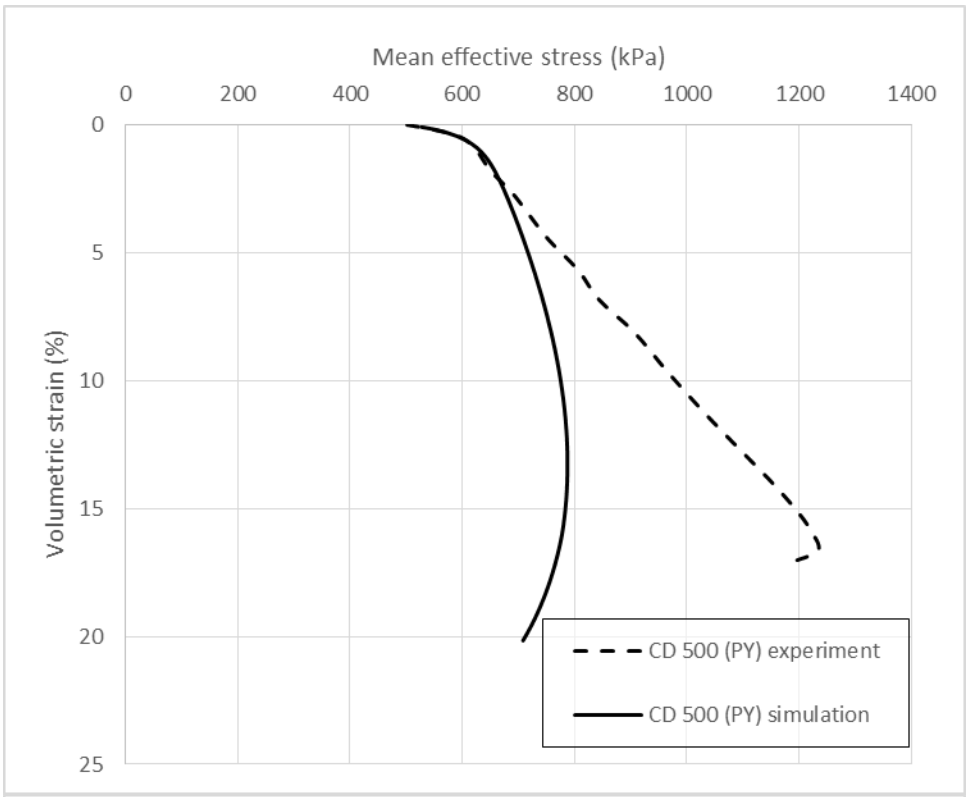

b)

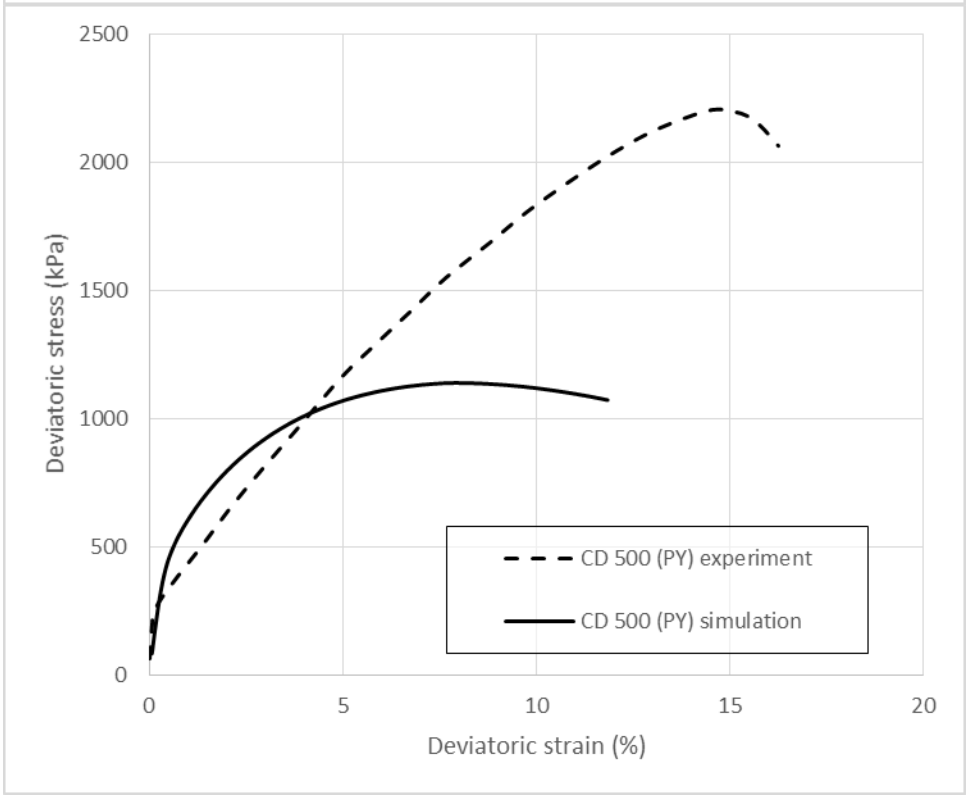

Figure 6.3-11: Simulation of drained shear behavior of pre-yield (PY) X_10-3-13 soil specimens: (a) mean effective stress versus volumetric strain, and (b) deviatoric strain versus deviatoric stress

a)

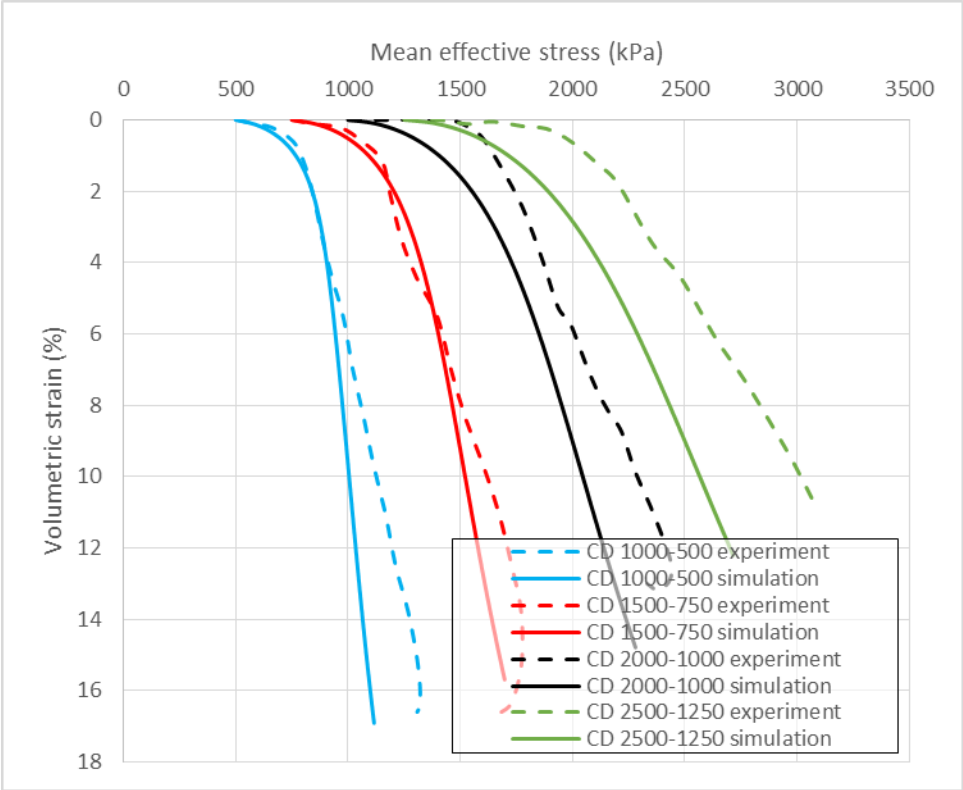

b)

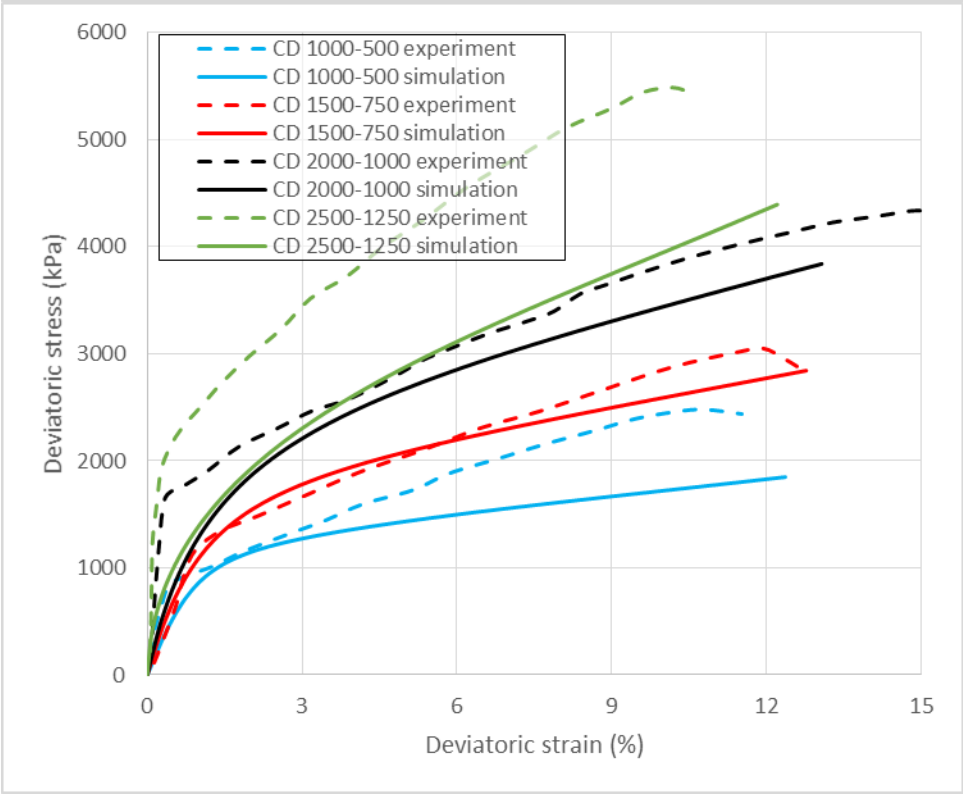

Figure 6.3-12: Simulation of drained shear behavior of overconsolidated X_10-3-13 soil specimens: (a) mean effective stress versus volumetric strain, and (b) deviatoric strain versus deviatoric stress

a)

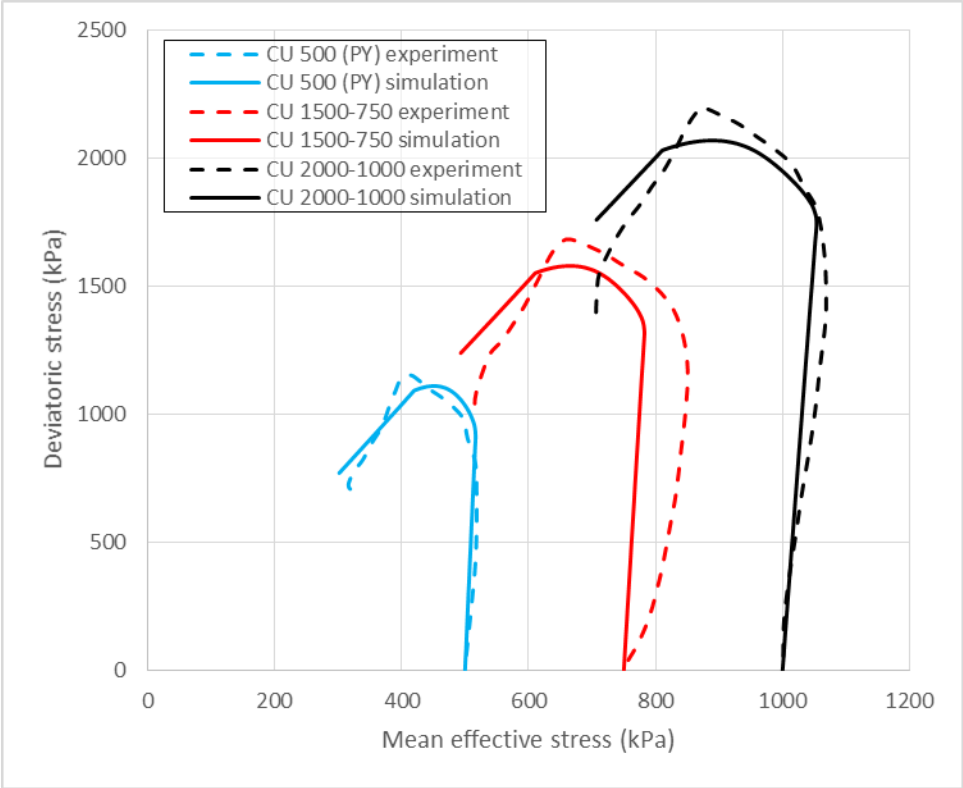

b)

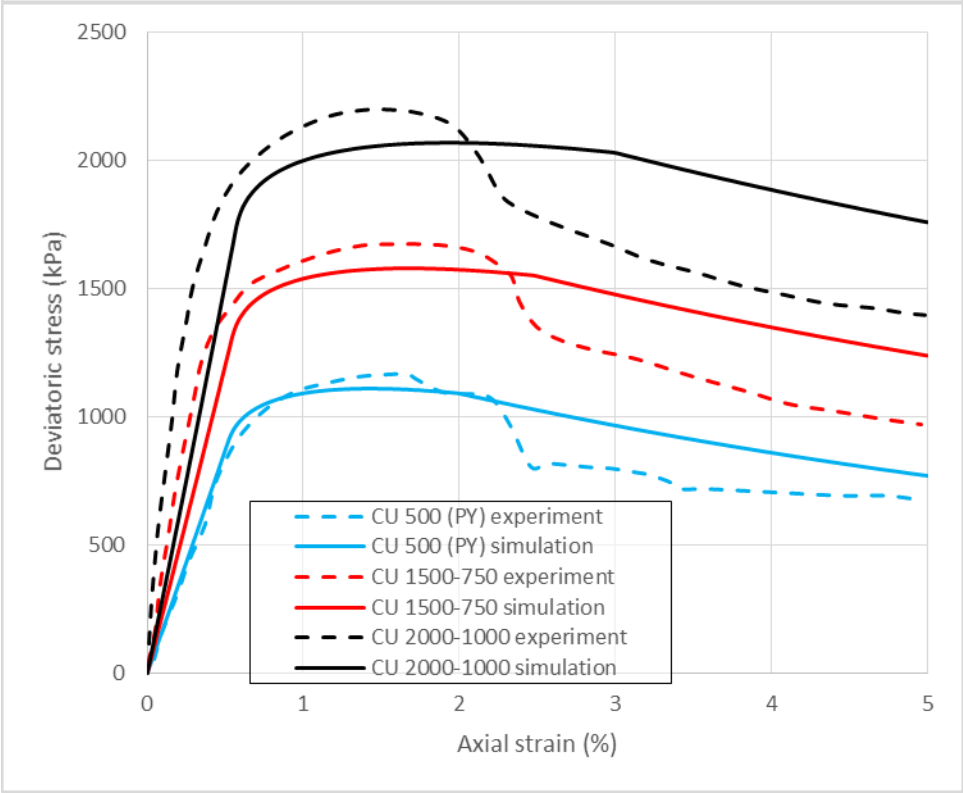

Figure 6.3-13: Simulation of undrained shear behavior of overconsolidated and pre-yield (PY) X_2-1-3 soil specimens: (a) mean effective stress versus deviatoric stress, and (b) axial strain versus deviatoric stress

a)

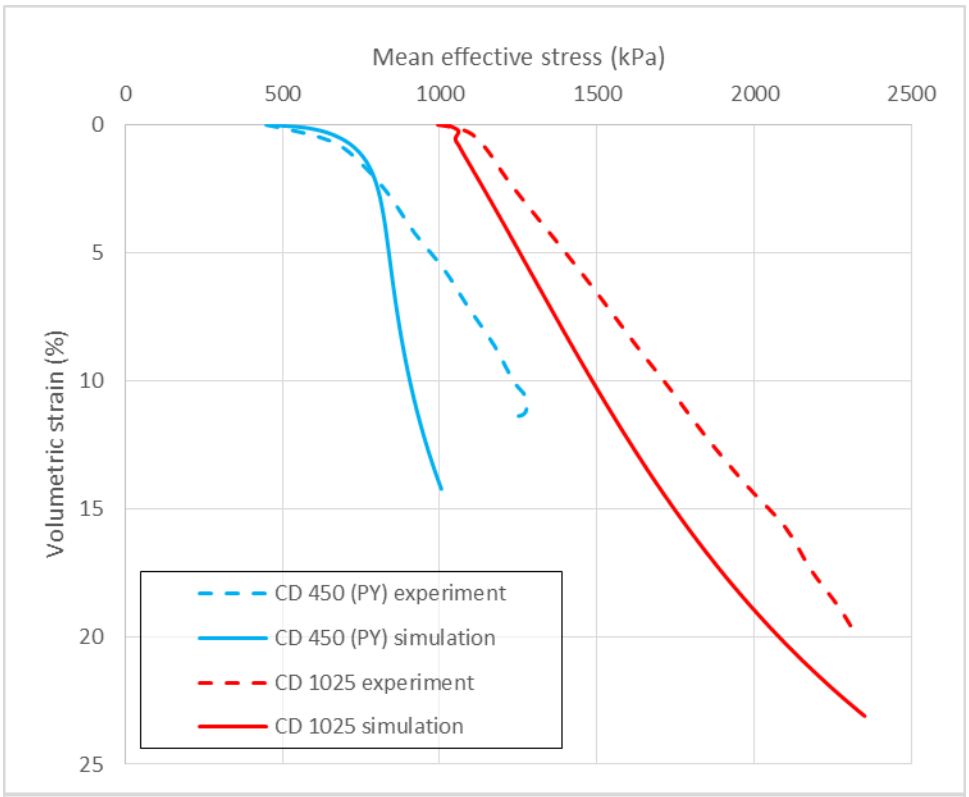

b)

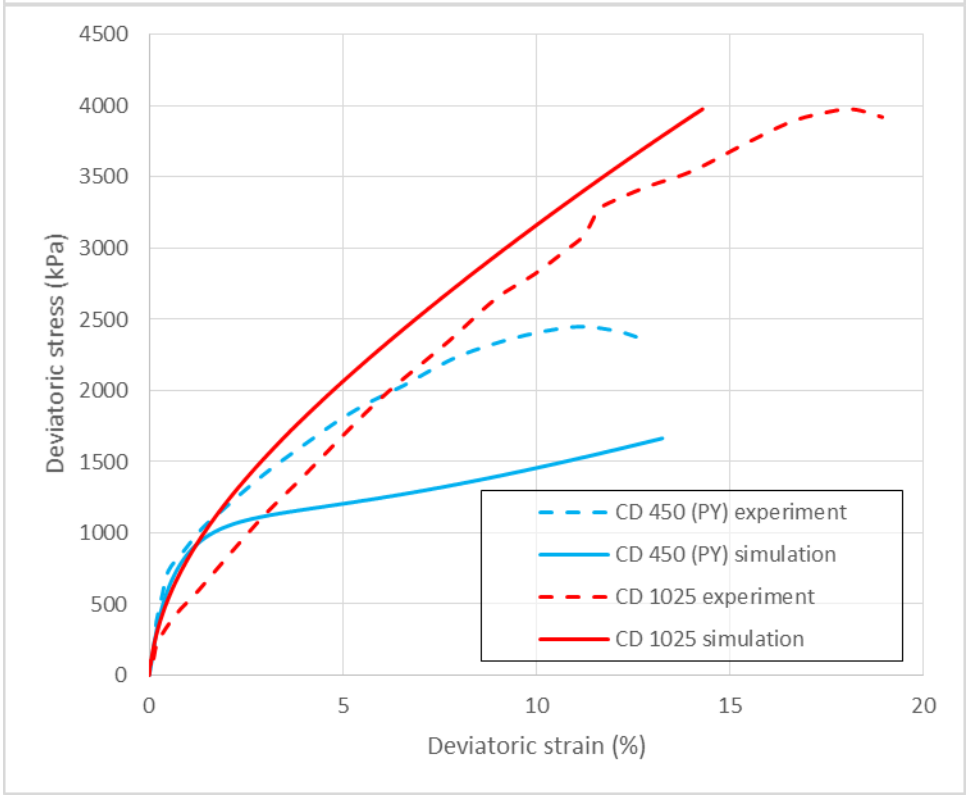

Figure 6.3-14: Simulation of drained shear behavior of normally consolidated and pre-yield (PY) X_2-1-3 soil specimens: (a) mean effective stress versus volumetric strain, and (b) deviatoric strain versus deviatoric stress

a)

b)

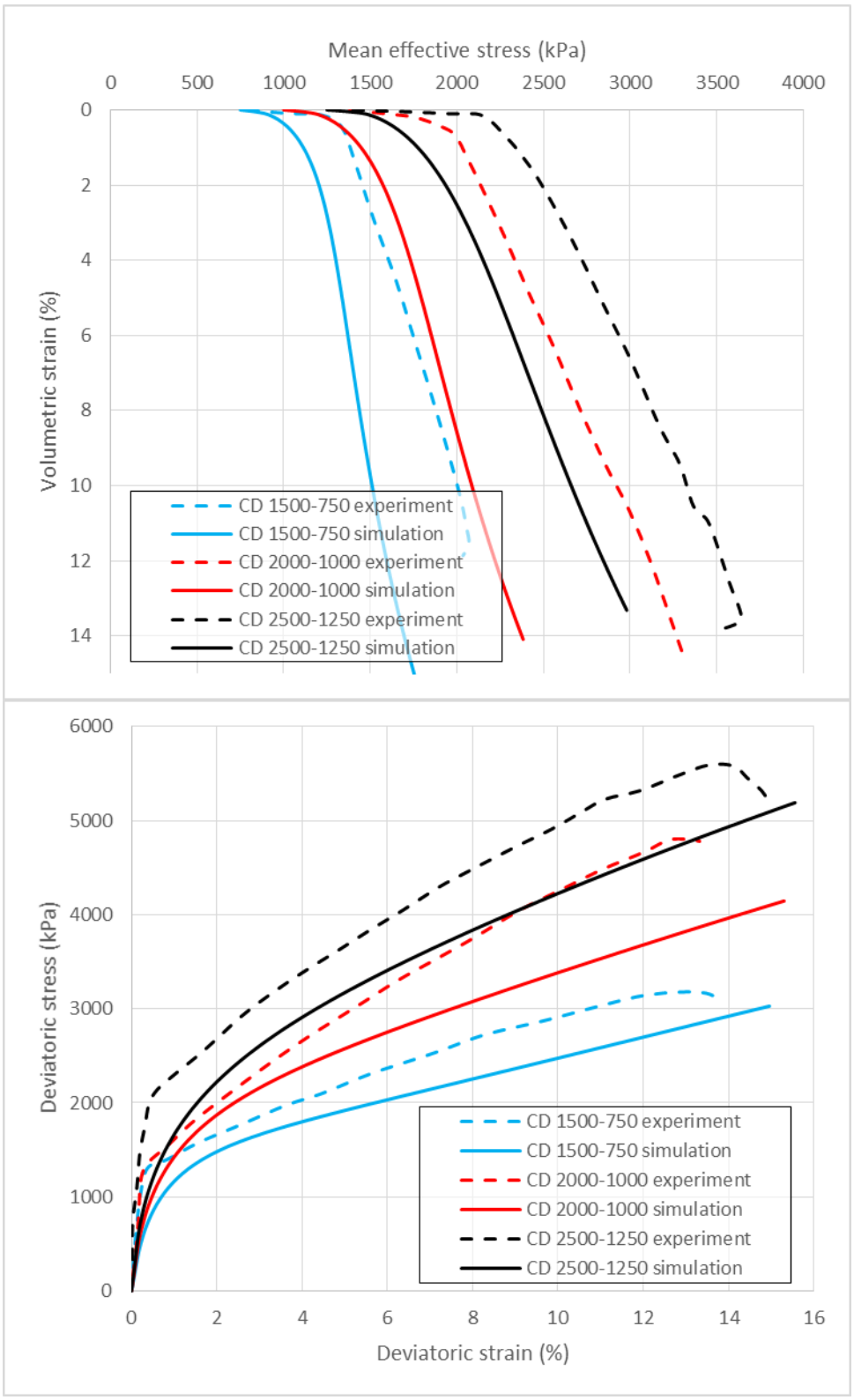

Figure 6.3-15: Simulation of drained shear behavior of overconsolidated X_2-1-3 soil specimens: (a) mean effective stress versus volumetric strain, and (b) deviatoric strain versus deviatoric stress

a)

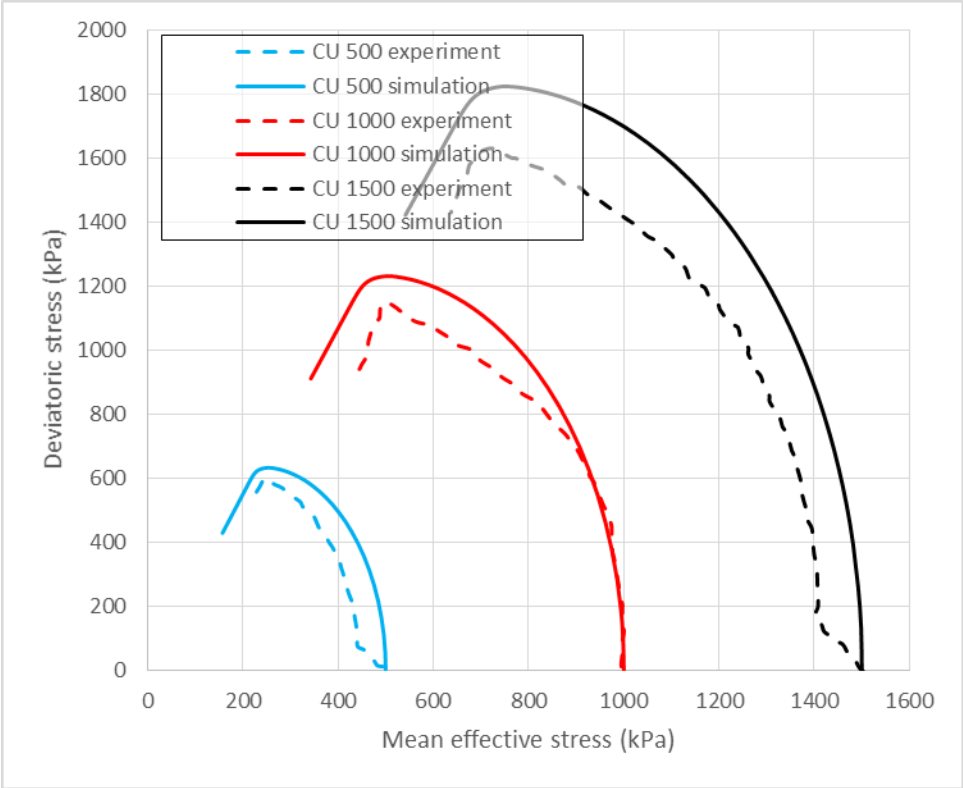

b)

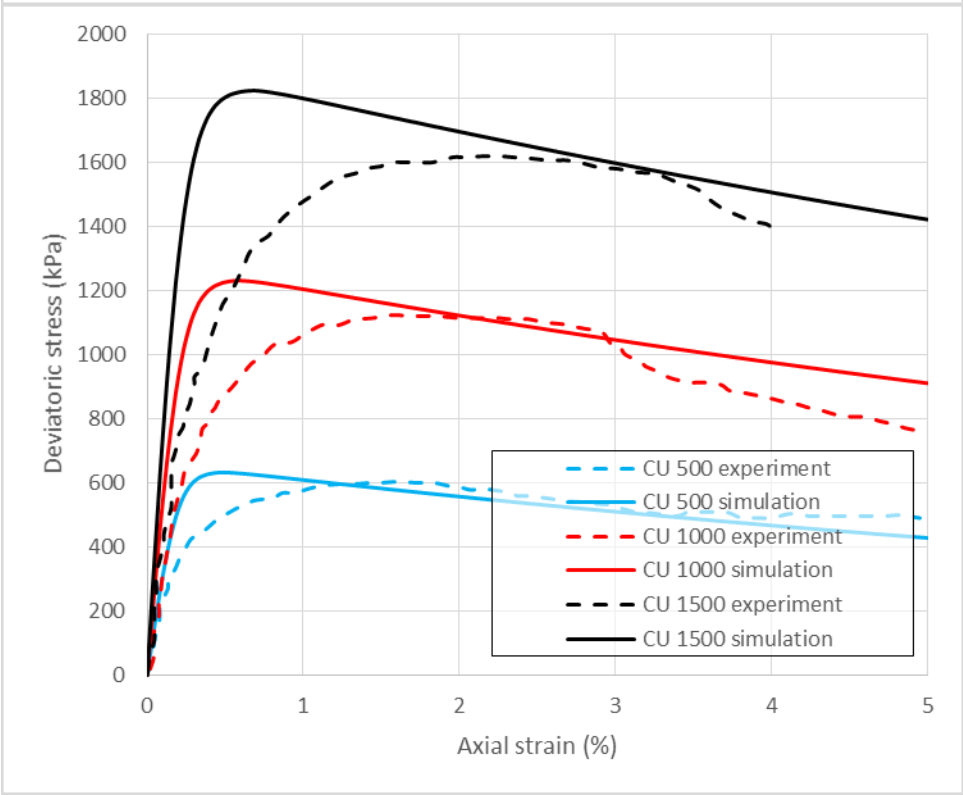

Figure 6.3-16: Simulation of undrained shear behavior of normally consolidated X_2-1-4 soil specimens: (a) mean effective stress versus deviatoric stress, and (b) axial strain versus deviatoric stress

a)

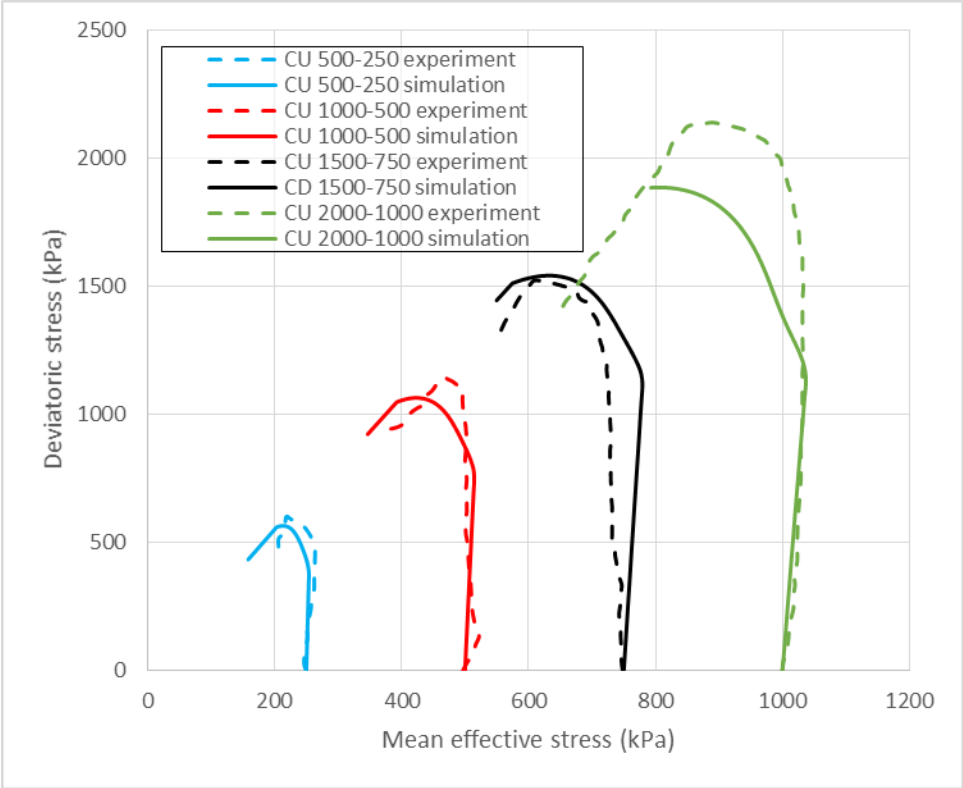

b)

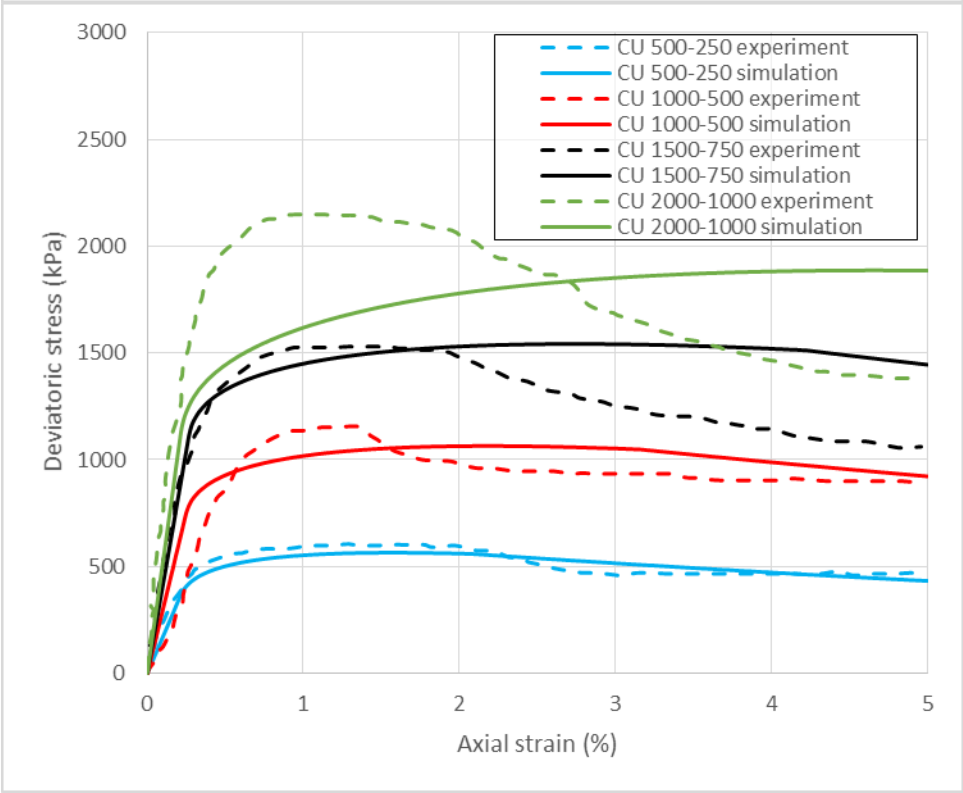

Figure 6.3-17: Simulation of undrained shear behavior of overconsolidated X_2-1-4 soil specimens: (a) mean effective stress versus deviatoric stress, and (b) axial strain versus deviatoric stress

a)

b)

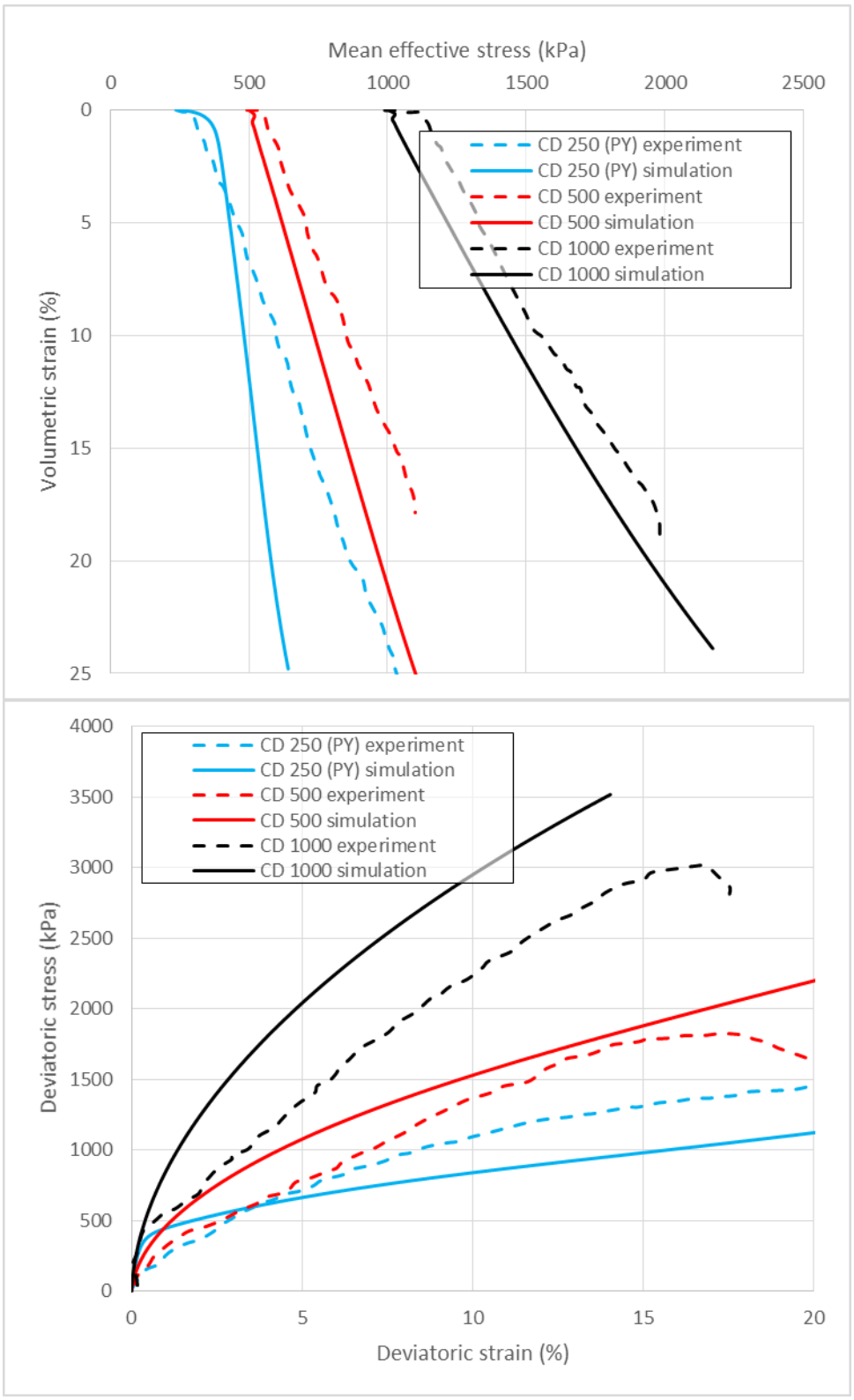

Figure 6.3-18: Simulation of drained shear behavior of normally consolidated and pre-yield (PY) X_2-1-4 soil specimens: (a) mean effective stress versus volumetric strain, and (b) deviatoric strain versus deviatoric stress

a)

b)

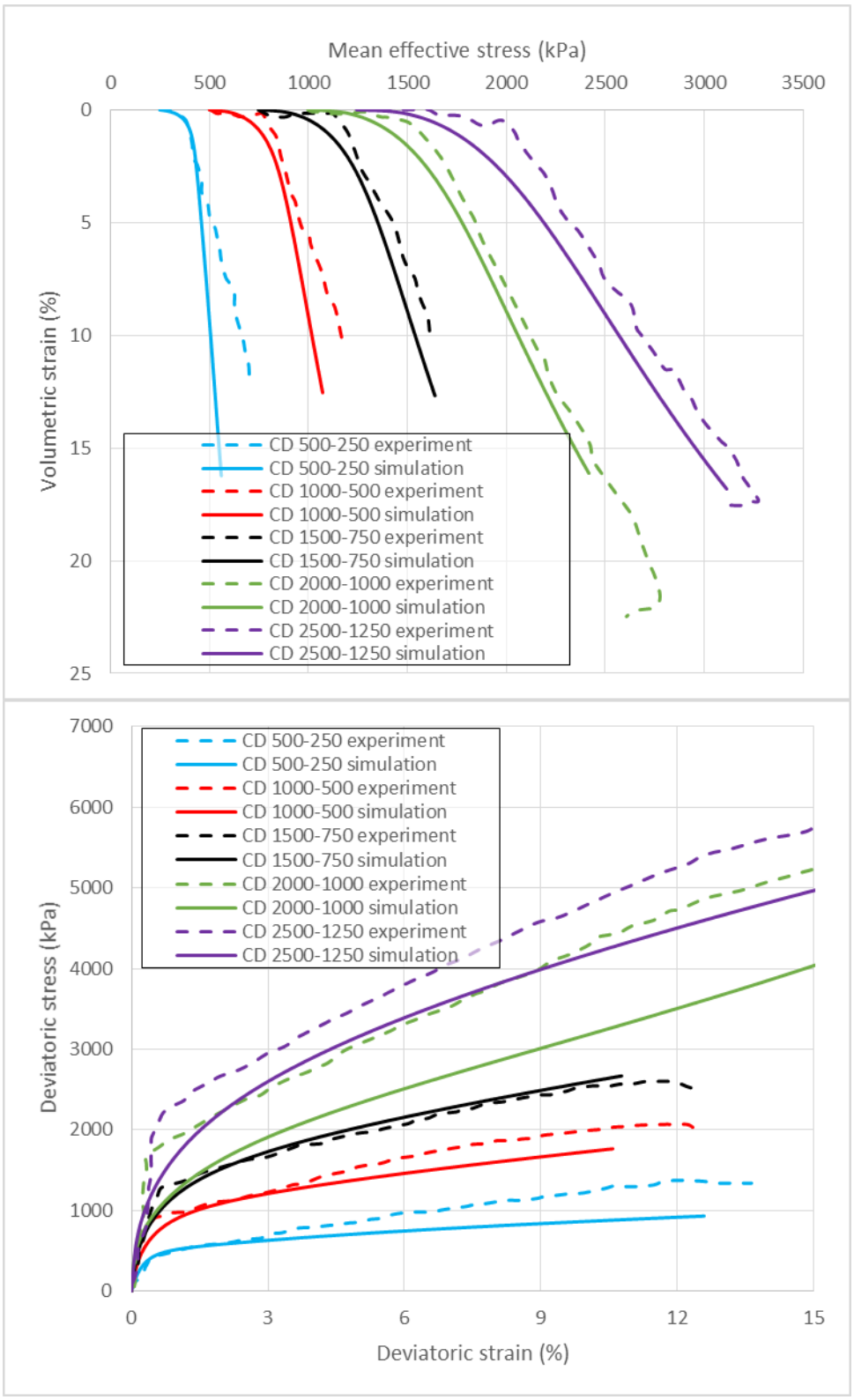

Figure 6.3-19: Simulation of drained shear behavior of overconsolidated X_2-1-4 soil specimens: (a) mean effective stress versus volumetric strain, and (b) deviatoric strain versus deviatoric stress

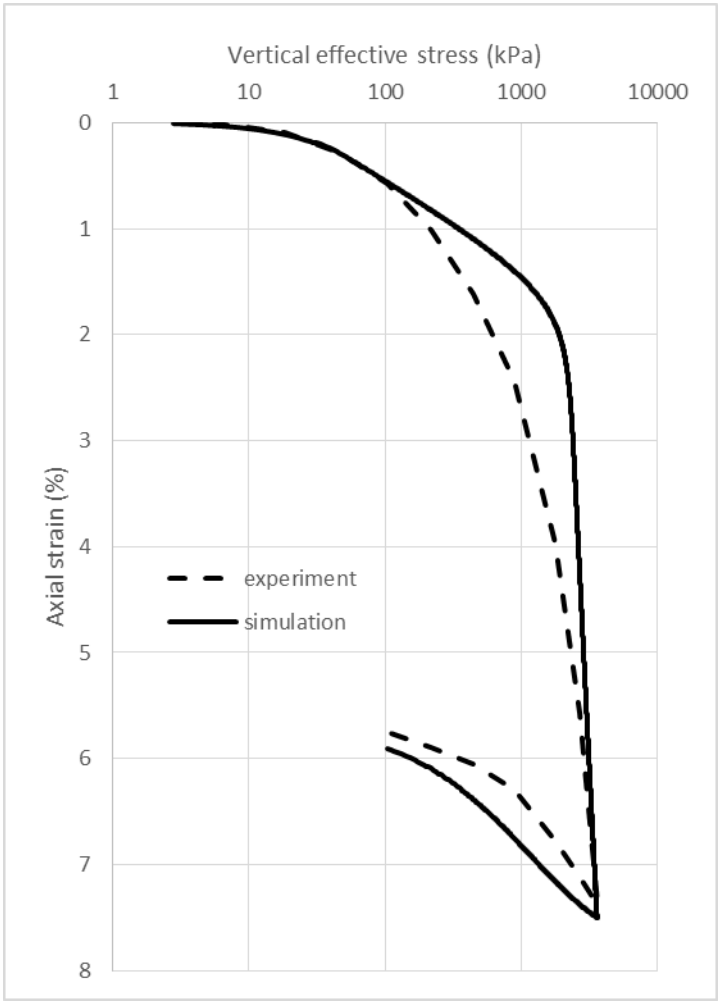

Figure 6.3-20: Simulation of oedometer consolidation behavior of Q_10-2-5 soil

a)

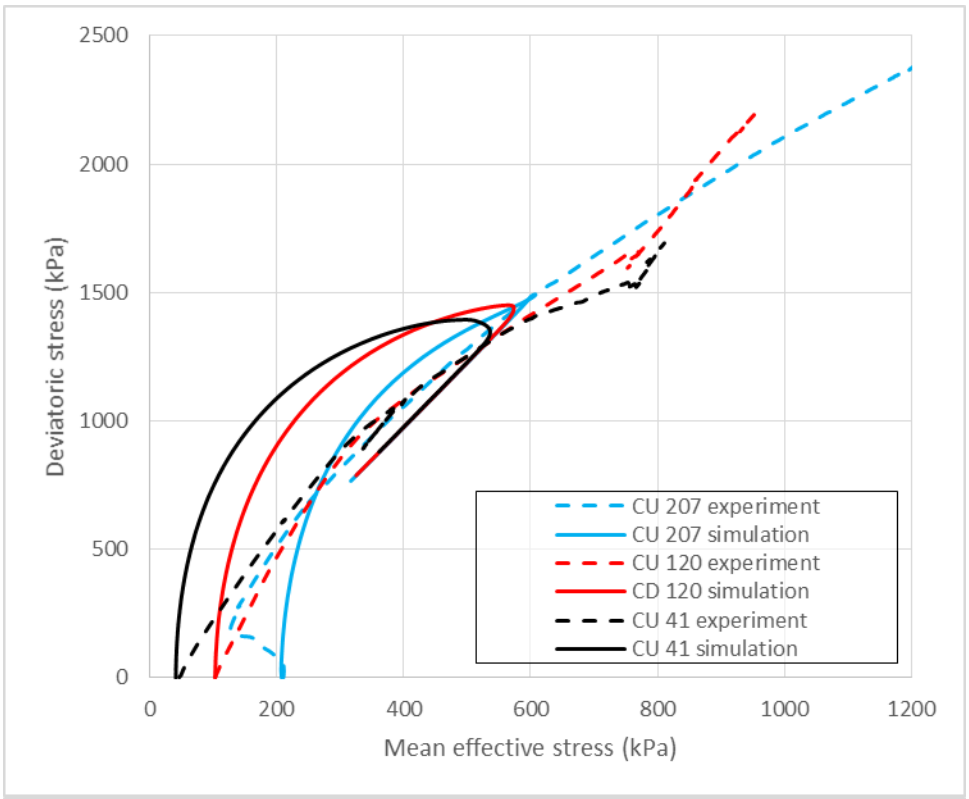

b)

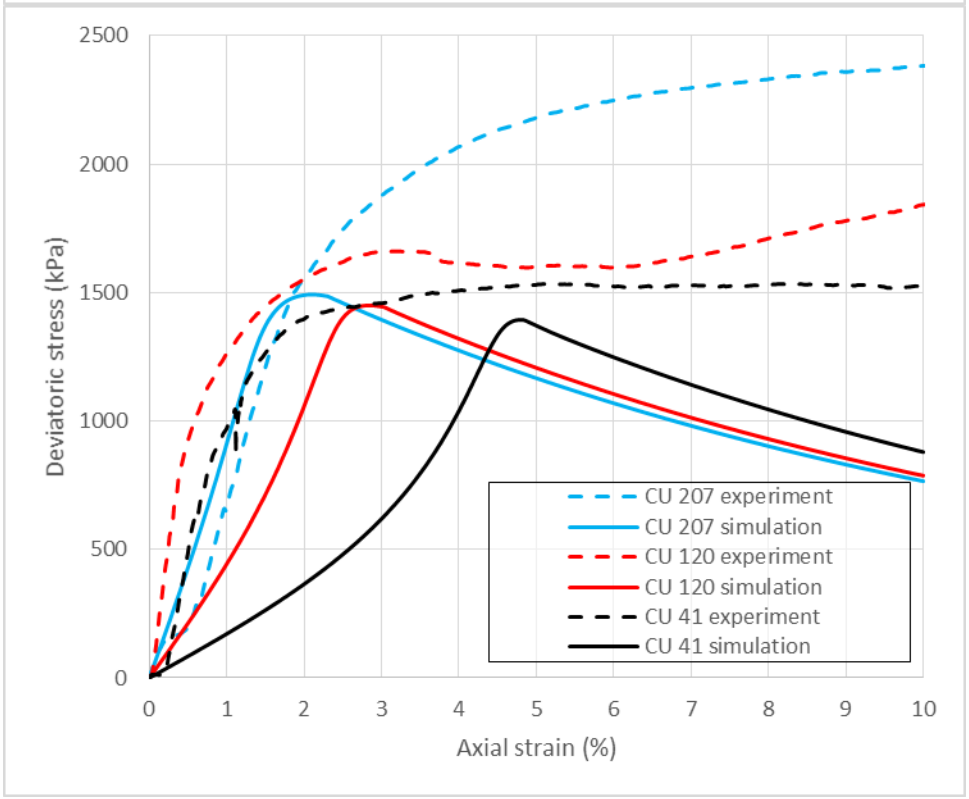

Figure 6.3-21: Simulation of undrained shear behavior of pre-yielded Q_10-2-5 soil specimens: (a) mean effective stress versus deviatoric stress, and (b) axial strain versus deviatoric stress

6.4 Comments on monotonic predictions

The model predictions in the previous subsection show the proposed model formulation will predict isotropic consolidation behavior and capture the general stress-strain behavior for soils subjected drained and undrained triaxial compression loading. Predictions for lightly overconsolidated and artificially lightly overconsolidated, pre-yield specimens show the best agreement with the actual results. Normally consolidated predictions using large confining stresses overestimate the deviatoric strength of the cement-mixed soil.

An important feature of stress-strain predictions to note is the tracking of dI_o through Equation 3.4-10. For a loading increment when the current stress state is located on the bounding surface, the numerical model will calculate a stress increment which pushes the state of stress along the bounding surface toward the peak of the surface, (I_0/R, NI_0/R), where N is the calculated slope of the line located through the origin and peak of the surface in direct stress invariant space. Once the current stress-state is located at the peak of the bounding surface, the stress-state will remain at the peak for additional loading stress increments. In the Dafalias and Herrmann (1986), and other plastic and elastoplastic models, this state defines the critical state. However in the proposed model, the line defined by the calculated slope, N, is not indicative of the actual critical state. In the current formulation, critical state may only be achieved once the cemented soil becomes fully remolded; i.e., the sensitivity equals one.

The “post-peak” behavior exhibited by the effective stress paths, most obvious in Figure 6.3-16a, tracks the evolution of the bounding surface as destructuring takes place. For all X-soil predictions, this “post-peak” behavior models the decrease in

deviatoric stress due to destructuring. Conversely, for Q-soil predictions the tracking of the maximum point on the bounding surface describes the downward hook in the effective stress paths and marked peak/residual deviatoric strength behavior in the stress-strain relationship (see Figure 6.3-21). The test data do not exhibit the hook behavior and destructuring shown in the predictions. The model begins to predict such unrealistic behaviors for pre-yield specimens with artificial overconsolidation ratios greater than 4.0.

The predictions show good agreement with the peak/residual deviatoric stress vs. axial strain undrained triaxial compression test data for normally consolidated and lightly overconsolidated (artificial and real) specimens. However, the test data show the deviatoric stresses have largely stabilized (i.e., reached the residual value) at, or before, 5% axial strain; for the predictions shown in the previous subsection, the predictions do not reach a residual deviatoric strength by 5% axial strain, but continue to exhibit destructuring for larger axial strains. Additional model predictions show the ultimate shear strength near critical state will be extremely low compared to that exhibited in the test data. Recall that Equations 3.4-10 and 3.4-11 describe the change in the size of the bounding surface and change in sensitivity. One may note from Equation 3.4-10 that the size of the bounding surface will generally decrease, or increase at a rate slower than the traditional elastoplastic formulation would predict, with the rate of change largely dependent on the sensitivity and rate parameters δ and π. Larger sensitivity implies a greater amount of structure, and thus a greater potential for decrease in the structured bounding surface and strain softening. The tendency of the predictions to exhibit greater

softening behavior than is evidenced by actual test data implies that the Xiao and Lee (2014) method of calibrating initial sensitivity could be improved.

6.5 A forecast of cyclic modeling capability

As the datasets used in this study do not include cyclic triaxial test data, the ability of the model to predict the behavior of cyclically loaded cement-mixed soils will be determined by a model prediction to the behavioral trends discussed in the literature.

Figure 6.5-1 shows the prediction for an undrained, two-way triaxial cyclic test using the model parameters for a normally consolidated X_10-3-13 specimen. Note that arrows indicate the trend with increasing numbers of cycles. The predictions exhibit shear modulus degradation, a phenomenon discussed by several authors studying small-strain pavement subgrade applications (Abu-Farsakh et al. 2015; Ardah et al. 2017; da Fonseca et al. 2013; Panico and da Fonseca 2016) and authors investigating cyclic behavior using larger deviatoric stresses (Subramaniam and Banerjee 2014). The model also captures the increases in pore water pressure generation, which is a key feature of cyclic response of soft clays but, is also identified as a characteristic response of cyclically loaded cemented marine clays (Moses and Rao 2003).

a)

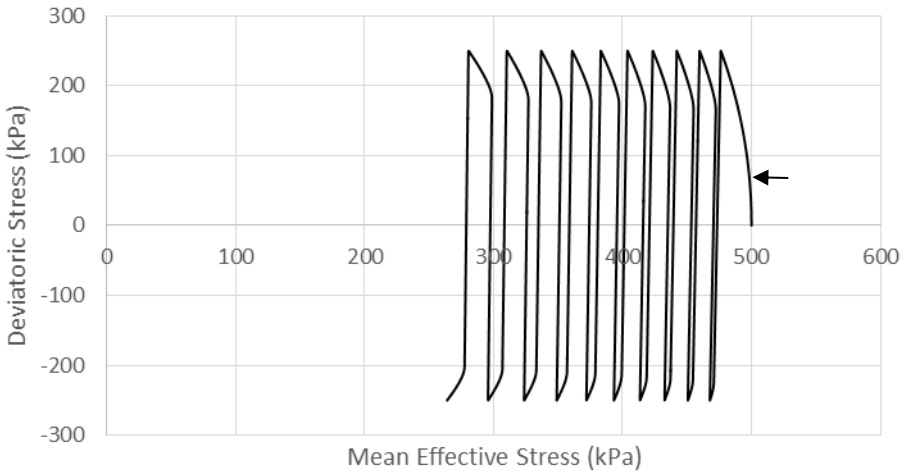

b)

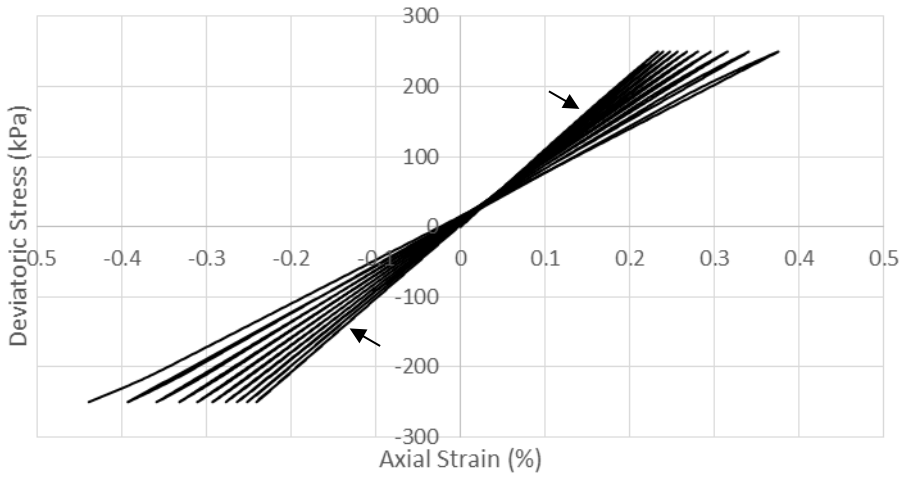

c)

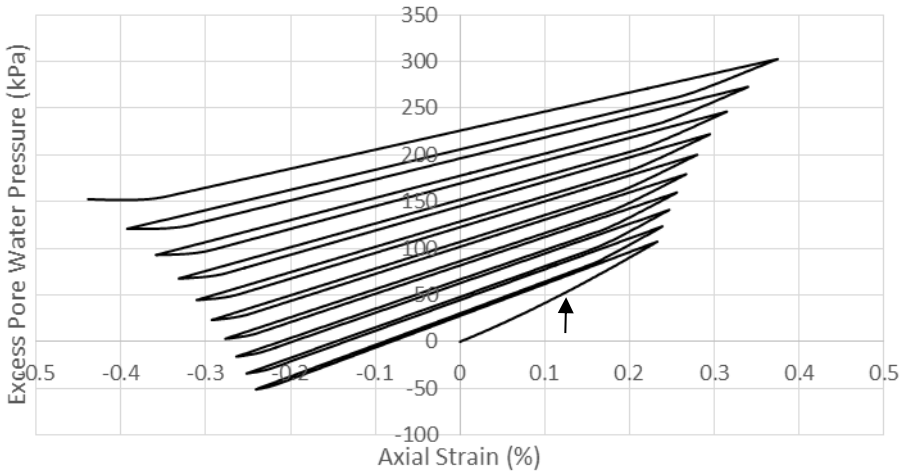

Figure 6.5-1: Prediction of an undrained, stress-controlled, two-way triaxial cyclic test for a normally consolidated X_5-1-6 specimen

6.6 Investigation into the effects of initial sensitivity

Excessive strain softening seen in the model predictions was not shown previously; however predictions with larger axial strains (see Figure 6.6-2) show continued destructuring over larger values of axial strain. Sensitivity is the model parameter relating the sizes of the bonded and remolded bounding surfaces. Therefore, excessive strain softening in monotonic model predictions indicates the choices of initial sensitivity are too large for the soils used in this study. It is hypothesized that using smaller values of initial sensitivity will result in better stress-strain predictions. In this section, this hypothesis will be tested by treating initial sensitivity as an additional fitted model parameter for simulations of X_2-1-4 undrained triaxial compression test data.

For this investigation, S_i and δ were calibrated simultaneously from the isotropic compression curve using a trial-and-error curve-fitting approach, shown in Figure 6.6-1. The parameter π was calibrated using the CU 500 test results shown in Figure 6.6-2a. The remaining parameters were assumed to be the same as used in the previous calibration. A list of the resulting model parameters is provided in Table 6.6-1.

Figure 6.6-2 compares test results, model predictions using the original theoretically-based definition of sensitivity, and model predictions using the fitted initial sensitivity value. Two test results are presented for each confining stress: one test using a specimen with a traditional triaxial test specimen and one specimen with a 1:1 ratio of height to diameter, denoted as a tall and short specimen, respectively. These two test results are presented as bounds of stress-strain behavior which may be expected in full-scale boundary value problems. The model predictions using the fitted initial

sensitivity shown in Figure 6.6-2 exhibit modest increases in predictive capacities over the predictions using the theoretically-based definition of sensitivity. New model predictions shown in Figure 6.6-2a exhibit faster destructuring, but also predict a higher residual deviatoric strength, than the original predictions; however, the model still over-predicts the occurrence of destructuring in this specimen. The new model prediction shown in Figure 6.6-2b shows much closer agreement with the test data, especially in the magnitude of residual deviatoric strength.

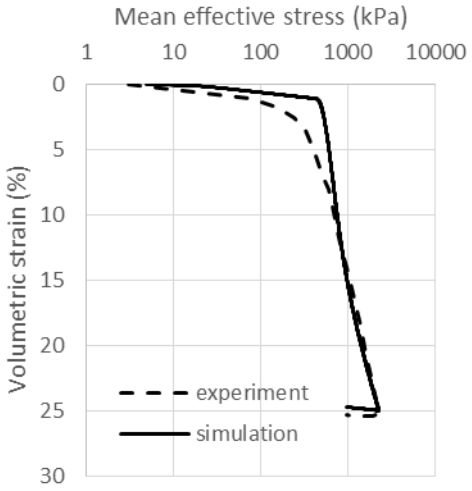

Figure 6.6-1: Simulation of isotropic consolidation behavior of X_2-1-4 soil specimen with S_i treated as a fitted parameter

Table 6.6-1: Bounding surface model parameters for prediction of X_2-1-4 soil tests with S_i treated as a fitted parameter

e_{in}	3.033	M_e^*/M_c^*	1.0	**c**	0.5
p'_0	439	**ν**	0.3	**s**	1.20
S_i	8.0	**R**	2.20	h_c	35.0
λ_u	0.300	**δ**	3.00	h_e/h_c	1.0
κ_s	0.013	**π**	2.30	**a**	2.0
M_c^*	2.53	**μ**	0.03		

a)

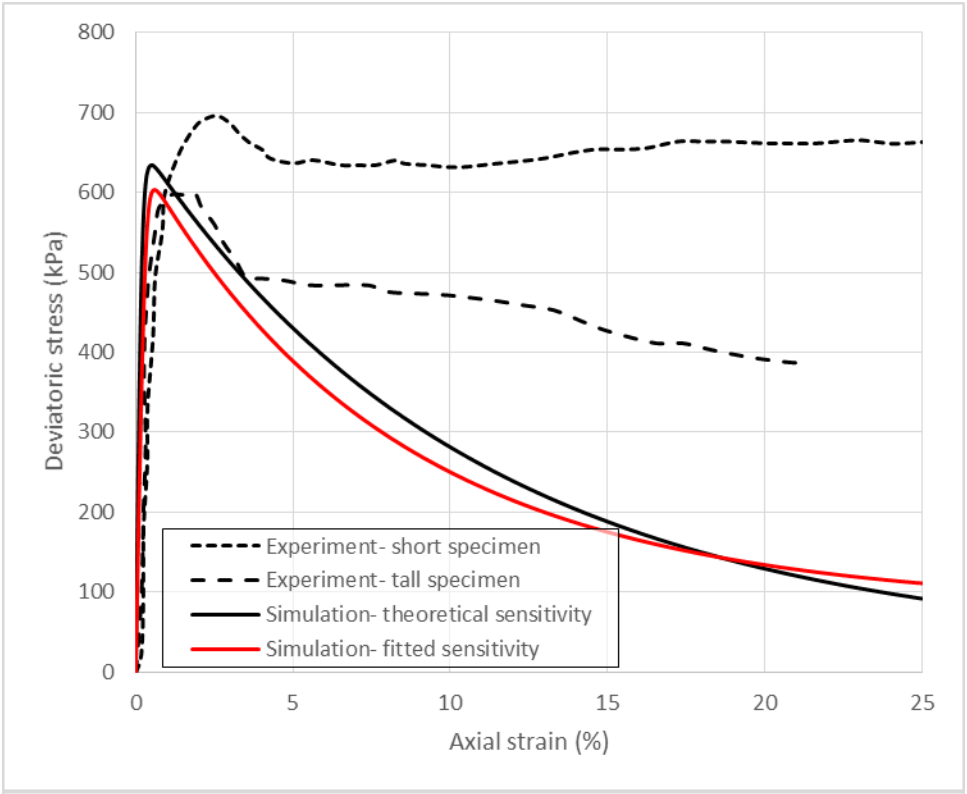

b)

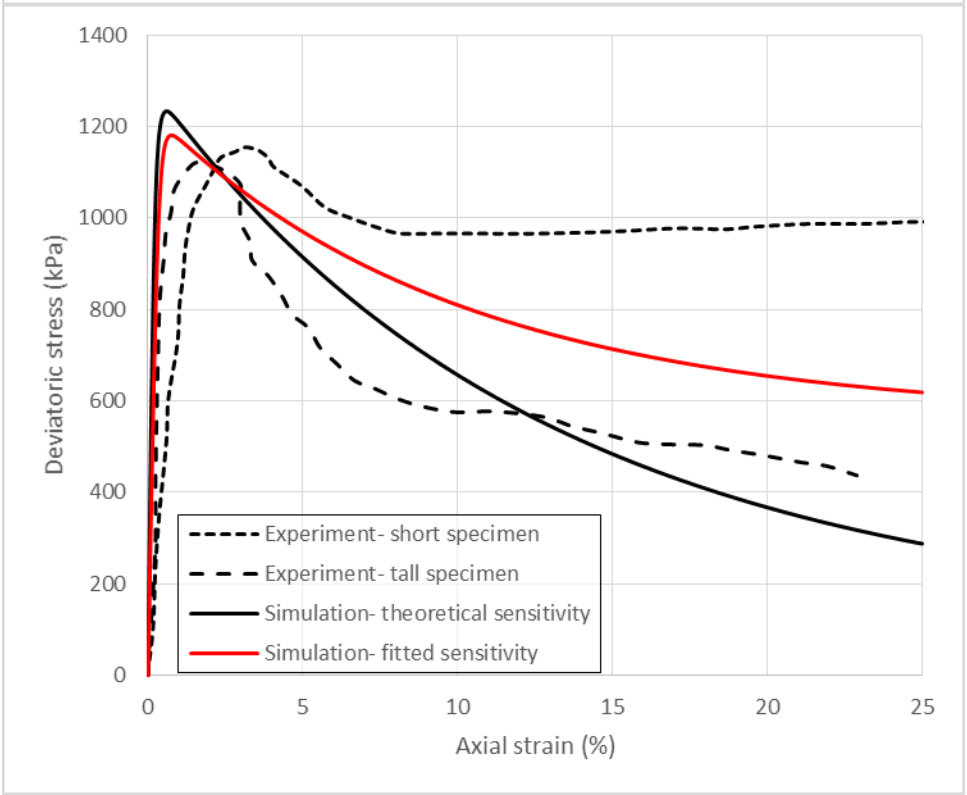

Figure 6.6-2: Comparison of simulations of axial strain versus deviatoric stress relationship for undrained shear behavior of large-strain, normally consolidated triaxial compression tests for X_2-1-4 soil specimens with theoretically determined and fitted S_i parameters: (a) CU 500, and (b) CU 1000

Chapter 7: Conclusions and recommendations

While the proposed model may not be meaningfully applied to artificially cemented soils with a large overconsolidation ratio, the model is able to capture the behavioral trends of lightly overconsolidated and normally consolidated soils. The ability of the implemented projection center relocation formulation to allow accumulation of plastic strain during load-reversal is demonstrated not only in the prediction of cyclic loading, but also during the unloading stage of the Q-soil oedometer test prediction. Although it should, again, be noted that an isotropic model may not be able to accurately predict anisotropic consolidation behavior. Despite the cyclic prediction not being compared with an actual test result, the prediction does exhibit the anticipated destructuring behaviors, namely decreasing secant shear modulus and increasing strain accumulation with an increasing number of loading cycles.

Excessive softening behavior in the monotonic model predictions implies the initial sensitivity values are excessively large. The Xiao and Lee (2014) calibration method, utilized in this dissertation, uses two separate specimens, one intact and one fully remolded, to characterize the sensitivity and the δ parameter. It is unclear if any control has been enacted to ensure the consolidation curves would coincide (i.e., reach the same specific volume or void ratio and p') if the intact specimen was loaded to cause a fully remolded state. It is hypothesized a more accurate representation of sensitivity would be achieved if a structured specimen is consolidated to very large stresses to effectively create a remolded state with the slope of the remolded consolidation line projected backwards to smaller p' values in order to determine the initial sensitivity and δ parameter. Future research should investigate if the resulting

values of S_i and δ are better predictors of the bond degradation, especially in undrained triaxial compression stress-strain behavior. Initial investigations, detailed in Section 6.6, indicate this will likely increase the predictive capabilities in some, but not all cases.

The results presented in the investigation into the effects of initial sensitivity and the model predictions for pre-yield, artificially heavily overconsolidated specimens (Figure 6.3-21) show that the current formulation over-predicts destructuring behavior at large strains and for soils with large artificial overconsolidation ratios. In addition to the redefinition of initial sensitivity, future work to refine the proposed model should modify the destructuring equations (3.4-10 and 3.4-11) to better reflect the soil behavior. Adoption of a non-associative flow rule should also be considered.

Although a large amount of work has been completed to characterize the stress-stain and destructuring behavior of cement-mixed soils, few fully developed and thorough data sets, including triaxial extension and cyclic loading, are available in the literature. Future work should focus on developing larger sets of laboratory test data, including:

- An isotropic consolidation test, loaded to extremely large stresses with at least one unloading;
- A set of pre-yield, undrained, triaxial compression and extension tests with artificial overconsolidation ratios equal to 2, 4, and 8;
- A set of pre-yield, drained, triaxial compression tests with artificial overconsolidation ratios equal to 2, 4, and 8;

- A set of normally consolidated, undrained triaxial compression and extension tests with confining stresses approximately equal to 1, 1.5, 2, and 4 times the isotropic yield stress;
- A set of normally consolidated, drained triaxial compression tests with confining stresses approximately equal to 1, 1.5, 2, and 4 times the isotropic yield stress;
- A set of overconsolidated, undrained triaxial compression and extension tests with preconsolidation pressures approximately equal to 1.5, 2, and 4 times the isotropic yield stress and overconsolidation ratios equal to 2, 4, and 8;
- A set of undrained, stress-controlled, one-way and two-way cyclic shear triaxial tests using pre-yield specimens with artificial overconsolidation ratios equal to 2, 4, 8 and maximum shear stresses equal to 15, 35, and 70% of the peak deviatoric strength for the comparable monotonic triaxial test;
- A set of undrained, stress-controlled, one-way and two-way cyclic shear triaxial tests using overconsolidated with preconsolidation pressures approximately equal to 1.5 and 4 times the isotropic yield stress, overconsolidation ratios equal to 2 and 4, and maximum shear stresses equal to 15, 35, and 70% of the peak deviatoric strength for the comparable monotonic triaxial test;
- A set of constant p' triaxial tests utilizing various confining stresses and artificial overconsolidation ratios; and
- A set of monotonic and cyclic plane strain or true triaxial tests with various boundary conditions.

Additional laboratory testing plans to investigate the strain-rate effects and development of stress-induced anisotropy should also be considered.

References

Abu-Farsakh, M., Dhakal, S., and Chen, Q. (2015). "Laboratory characterization of cementitiously treated/stabilized very weak subgrade soil under cyclic loading." *Soils and Foundations*, 55(3), 504-516.

Ardah, A., Chen, Q., and Abu-Farsakh, M. (2017). "Evaluating the performance of very weak subgrade soils treated/stabilized with cementitious materials for sustainable pavements." *Transportation Geotechnics*, 11, 107-119.

Arroyo, M., Ciantia, M., Castellanza, R., and Gens, A. "A soft-rock model for cement-improved clays." *Proc., 15th European conference of soil mechanics and foundation engineering*, 501-506.

Arroyo, M., Ciantia, M., Castellanza, R., Gens, A., and Nova, R. (2012). "Simulation of cement-improved clay structures with a bonded elasto-plastic model: A practical approach." *Computers and Geotechnics*, 45, 140-150.

Asaoka, A., Nakano, M., and Noda, T. (2000). "Superloading yield surface concept for highly structured soil behavior." *Soils and Foundations*, 40(2), 99-110.

Baudet, B., and Stallebrass, S. (2004). "A constitutive model for structured clays." *Géotechnique*, 54(4), 269-278.

Cambou, B., and Hicher, P. Y. (2010). "Elastoplastic Modeling of Soils: Cyclic Loading." *Constitutive Modeling of Soils and Rocks*, 143-186.

Chiu, C., Zhu, W., and Zhang, C. (2009). "Yielding and shear behaviour of cement-treated dredged materials." *Engineering Geology*, 103(1-2), 1-12.

Cotecchia, F., and Chandler, R. (2000). "A general framework for the mechanical behaviour of clays." *Géotechnique*, 50(4), 431-448.

da Fonseca, A. V., Rios, S., Amaral, M., and Panico, F. (2013). "Fatigue cyclic tests on artificially cemented soil." *Geotechnical Testing Journal*, 36(2), 227-235.

Dafalias, Y. (1975). "On cyclic and anisotropic plasticity." *A General model*.

Dafalias, Y. F. (1986). "Bounding surface plasticity. I: Mathematical foundation and hypoplasticity." *Journal of Engineering Mechanics*, 112(9), 966-987.

Dafalias, Y. F., and Herrmann, L. R. (1986). "Bounding surface plasticity. II: Application to isotropic cohesive soils." *Journal of Engineering Mechanics*, 112(12), 1263-1291.

Dafalias, Y. F., and Popov, E. P. (1977). "Cyclic loading for materials with a vanishing elastic region." *Nuclear Engineering and Design*, 41(2), 293-302.

Desai, C. S., and Toth, J. (1996). "Disturbed state constitutive modeling based on stress-strain and nondestructive behavior." *International Journal of Solids and Structures*, 33(11), 1619-1650.

Desmorat, R., Gatuingt, F., and Ragueneau, F. (2007). "Nonlocal anisotropic damage model and related computational aspects for quasi-brittle materials." *Engineering Fracture Mechanics*, 74(10), 1539-1560.

González, N. A., Gens Solé, A., Arroyo Alvarez de Toledo, M., and Rouainia, M. "A structured constitutive model for simulating the behaviour of an overconsolidated bonded clay." *Proc., Computational plasticity XI: fundamentals and applications: proceedings of the XI International Conference on Computational Plasticity held in Barcelona, Spain, 07-09 September 2011*, Centro Internacional de Métodos Numéricos en Ingeniería (CIMNE), 2-12.

Halm, D., and Dragon, A. (1998). "An anisotropic model of damage and frictional sliding for brittle materials." *European Journal of Mechanics-A/Solids*, 17(3), 439-460.

Hashiguchi, K. (1977). "Elastoplastic constitutive laws of granular materials." *Constitutive Equations of Soils (Proc. 9th ICFSME, Spec. Session 9)*, 73-82.

Herrmann, L. R., Kaliakin, V., Shen, C., Mish, K. D., and Zhu, Z.-Y. (1987). "Numerical implementation of plasticity model for cohesive soils." *Journal of engineering mechanics*, 113(4), 500-519.

Hong, P., Pereira, J.-M., Cui, Y.-J., Tang, A. M., Collin, F., and Li, X. L. (2014). "An elastoplastic model with combined isotropic–kinematic hardening to predict the cyclic behavior of stiff clays." *Computers and Geotechnics*, 62, 193-202.

Horpibulsuk, S., Liu, M. D., Liyanapathirana, D. S., and Suebsuk, J. (2010). "Behaviour of cemented clay simulated via the theoretical framework of the structured cam clay model." *Computers and Geotechnics*, 37(1-2), 1-9.

Hu, C., and Liu, H. (2015). "A new bounding-surface plasticity model for cyclic behaviors of saturated clay." *Communications in Nonlinear Science and Numerical Simulation*, 22(1-3), 101-119.

Hughes, T. J. (1984). "Numerical implementation of constitutive models: rate-independent deviatoric plasticity." *Theoretical foundation for large-scale computations for nonlinear material behavior*, Springer, 29-63.

Jiang, M., Yu, H. S., and Leroueil, S. (2007). "A simple and efficient approach to capturing bonding effect in naturally microstructured sands by discrete element method." *International Journal for Numerical Methods in Engineering*, 69(6), 1158-1193.

Kaliakin, V., and Dafalias, Y. (1989). "Simplifications to the bounding surface model for cohesive soils." *International Journal for Numerical and Analytical Methods in Geomechanics*, 13(1), 91-100.

Kamruzzaman, A., Chew, S., and Lee, F. (2009). "Structuration and destructuration behavior of cement-treated Singapore marine clay." *Journal of geotechnical and geoenvironmental engineering*, 135(4), 573-589.

Kasama, K., Ochiai, H., and Yasufuku, N. (2000). "On the stress-strain behaviour of lightly cemented clay based on an extended critical state concept." *Soils and Foundations*, 40(5), 37-47.

Lanoye, E., Cormery, F., Kondo, D., and Shao, J.-F. (2013). "An isotropic unilateral damage model coupled with frictional sliding for quasi-brittle materials." *Mechanics Research Communications*, 53, 31-35.

Larew, H., and Leonards, G. "A strength criterion for repeated loads." *Proc., Highway Research Board Proceedings*.

Lee, K., Chan, D., and Lam, K. (2004). "Constitutive model for cement treated clay in a critical state frame work." *Soils and foundations*, 44(3), 69-77.

Li, T., and Meissner, H. (2002). "Two-surface plasticity model for cyclic undrained behavior of clays." *Journal of geotechnical and geoenvironmental engineering*, 128(7), 613-626.

Liu, E.-L., Yu, H.-S., Zhou, C., Nie, Q., and Luo, K.-T. (2016). "A Binary-Medium Constitutive Model for Artificially Structured Soils Based on the Disturbed State Concept and Homogenization Theory." *International Journal of Geomechanics*, 17(7), 04016154.

Liu, M., and Carter, J. (2000). "Modelling the destructuring of soils during virgin compression." *Géotechnique*, 50(4), 479-483.

Liu, M. D., Carter, J. P., and Airey, D. W. (2010). "Sydney soil model. I: Theoretical formulation." *International Journal of Geomechanics*, 11(3), 211-224.

Liu, M. D., Carter, J. P., Horpibulsuk, S., and Liyanapathirana, D. S. (2006). "Modelling the behaviour of cemented clay." *Ground Modification and Seismic Mitigation*, 65-72.

Masing, G. "Eigenspannungen und verfestigung beim messing." *Proc., Proceedings, second international congress of applied mechanics*, 332-335.

McDowell, G., and Hau, K. (2003). "A simple non-associated three surface kinematic hardening model." *Géotechnique*, 53(4), 433-437.

Miura, N., Horpibulsuk, S., and Nagaraj, T. (2001). "Engineering behavior of cement stabilized clay at high water content." *Soils and Foundations*, 41(5), 33-45.

Montáns, F.-J. (2000). "Bounding surface plasticity model with extended Masing behavior." *Computer methods in applied mechanics and engineering*, 182(1-2), 135-162.

Moses, G. G., and Rao, S. N. (2003). "Degradation in cemented marine clay subjected to cyclic compressive loading." *Marine Georesources and Geotechnology*, 21(1), 37-62.

Mroz, Z. (1966). "On forms of constitutive laws for elastic- plastic solids(Linear and nonlinear nonassociated flow laws analyzed for elastoplastic work-hardenable solids)." *Archiwum Mechaniki Stosowanej*, 18(1), 3-35.

Mroz, Z. (1967). "On the description of anisotropic workhardening." *Journal of the Mechanics and Physics of Solids*, 15(3), 163-175.

Navarro, A., Giráldez, J., and Vallellano, C. (2005). "A constitutive model for elastoplastic deformation under variable amplitude multiaxial cyclic loading." *International journal of fatigue*, 27(8), 838-846.

Nguyen, L., Fatahi, B., and Khabbaz, H. (2017). "Development of a constitutive model to predict the behavior of cement-treated clay during cementation degradation: C3 model." *International Journal of Geomechanics*, 17(7), 04017010.

Nguyen, L. D., Fatahi, B., and Khabbaz, H. (2014). "A constitutive model for cemented clays capturing cementation degradation." *International Journal of Plasticity*, 56, 1-18.

Nieto-Leal, A., and Kaliakin, V. (2013). "Behavior of cohesive soils subjected to cyclic loading “an extensive review of pertinent literature”." Technical report, Department of Civil and Environmental Engineering, University of Delaware.

Nieto-Leal, A., and Kaliakin, V. N. (2014). "Improved shape hardening function for bounding surface model for cohesive soils." *Journal of Rock Mechanics and Geotechnical Engineering*, 6(4), 328-337.

Nieto Leal, A. (2016). *Generalized bounding surface model for cohesive soils: a novel formulation for monotonic and cyclic loading*, Dissertation, Department of Civil and Environmental Engineering, University of Delaware.

Nieto Leal, A., and Kaliakin, V. N. (2016). "General response observed in cyclically loaded cohesive soils." *Ciencia e Ingeniería Neogranadina*, 26(1), 21-39.

Nova, R., Castellanza, R., and Tamagnini, C. (2003). "A constitutive model for bonded geomaterials subject to mechanical and/or chemical degradation." *International*

Journal for Numerical and Analytical Methods in Geomechanics, 27(9), 705-732.

Obermayr, M., Dressler, K., Vrettos, C., and Eberhard, P. (2013). "A bonded-particle model for cemented sand." *Computers and Geotechnics*, 49, 299-313.

Ouria, A. (2017). "Disturbed State Concept–Based Constitutive Model for Structured Soils." *International Journal of Geomechanics*, 17(7), 04017008.

Panico, F., and da Fonseca, A. V. (2016). "Long Term Cyclic Response of a Soil-Cement Mixture: Experimental Study and Modelling." *Procedia engineering*, 143, 178-186.

Quiroga, A. J., Thompson, Z. M., Muraleetharan, K. K., Miller, G. A., and Cerato, A. B. (2017). "Stress–strain behavior of cement-improved clays: testing and modeling." *Acta Geotechnica*, 12(5), 1003-1020.

Roscoe, K. H., and Burland, J. (1968). "On the generalized stress-strain behaviour of wet clay." *Engineering Plasticity*, 535-609.

Rouainia, M., and Muir Wood, D. (2000). "A kinematic hardening constitutive model for natural clays with loss of structure." *Géotechnique*, 50(2), 153-164.

Rowe, P. (1963). "Stress-dilatancy, earth pressures, and slopes." *Journal of the Soil Mechanics and Foundations Division*, 89(3), 37-62.

Rowe, P. W. "The stress-dilatancy relation for static equilibrium of an assembly of particles in contact." *Proc., Proc. R. Soc. Lond. A*, The Royal Society, 500-527.

Seidalinov, G., and Taiebat, M. (2014). "Bounding surface SANICLAY plasticity model for cyclic clay behavior." *International Journal for Numerical and Analytical Methods in Geomechanics*, 38(7), 702-724.

Sharma, S. S., and Fahey, M. (2003). "Degradation of stiffness of cemented calcareous soil in cyclic triaxial tests." *Journal of Geotechnical and Geoenvironmental engineering*, 129(7), 619-629.

Sheng, D., Sloan, S., and Yu, H. (2000). "Aspects of finite element implementation of critical state models." *Computational mechanics*, 26(2), 185-196.

Sheu, W.-Y. (1984). "Modeling of stress-strain-strength behavior of a clay under cyclic loading."Ph. D. dissertation, University of Colorado.

Subramaniam, P., and Banerjee, S. (2014). "Factors affecting shear modulus degradation of cement treated clay." *Soil Dynamics and Earthquake Engineering*, 65, 181-188.

Suebsuk, J., Horpibulsuk, S., and Liu, M. D. (2010). "Modified Structured Cam Clay: A generalised critical state model for destructured, naturally structured and artificially structured clays." *Computers and Geotechnics*, 37(7-8), 956-968.

Suebsuk, J., Horpibulsuk, S., and Liu, M. D. (2011). "A critical state model for overconsolidated structured clays." *Computers and Geotechnics*, 38(5), 648-658.

Taiebat, M., Dafalias, Y. F., and Peek, R. (2010). "A destructuration theory and its application to SANICLAY model." *International Journal for Numerical and Analytical Methods in Geomechanics*, 34(10), 1009-1040.

Vatsala, A., Nova, R., and Murthy, B. S. (2001). "Elastoplastic model for cemented soils." *Journal of Geotechnical and Geoenvironmental Engineering*, 127(8), 679-687.

Wathugala, G., and Desai, C. (1993). "Constitutive model for cyclic behavior of clays. I: Theory." *Journal of Geotechnical Engineering*, 119(4), 714-729.

Xiao, H., and Lee, F. (2014). "An energy-based isotropic compression relation for cement-admixed soft clay." *Géotechnique*, 64(5), 412.

Xiao, H., Lee, F. H., and Liu, Y. (2016). "Bounding surface cam-clay model with cohesion for cement-admixed clay." *International Journal of Geomechanics*, 17(1), 04016026.

Yu, H., Tan, S., and Schnaid, F. (2007). "A critical state framework for modelling bonded geomaterials." *Geomechanics and Geoengineering*, 2(1), 61-74.

Zhang, D.-M., Yin, Z.-Y., Hicher, P.-Y., and Huang, H.-W. (2013). "Analysis of cement-treated clay behavior by micromechanical approach." *Frontiers of Structural and Civil Engineering*, 7(2), 137-153.

Appendix A: Specific forms of partial derivatives of the bounding surface equation and variable bounding surface parameters

From Equation 3.5-8:

$$F_{,\bar{I}} = 2I_0\left(\frac{\bar{I}}{I_0} - \frac{1}{R}\right) \quad \textbf{A-1}$$

$$F_{,\bar{J}} = 2\bar{J}\left(\frac{R-1}{N}\right)^2 \quad \textbf{A-2}$$

$$F_{,N} = -\frac{2\bar{J}^2}{N}\left(\frac{R-1}{N}\right)^2 \quad \textbf{A-3}$$

$$F_{,I_0} = -\frac{2}{R}\{\bar{I} - (R-2)I_0\} \quad \textbf{A-4}$$

$$F_{,\theta} = \frac{\partial F}{\partial N}\frac{\partial N}{\partial \theta} \quad \textbf{A-5}$$

From Equations 3.5-9 and 3.5-10:

$$\frac{\partial N}{\partial \theta} = g_{N,\theta} \quad \textbf{A-6}$$

$$\frac{\partial N}{\partial S} = \frac{\mu N_c^* g_N}{S(1-\mu \ln S)^2} \quad \textbf{A-7}$$

where $N(\theta)$ and $g_N(\theta)$ are given by Equation 3.5-9, and $g_{N,\theta}$ is the partial derivative of Equation 3.5-9 with respect to Lode angle, given by:

$$g_{N,\theta} = \frac{3{k_N}^4\left(1-{k_N}^4\right)\cos(3\theta)}{2\left(\frac{2{k_N}^4}{1+{k_N}^4-\left(1-{k_N}^4\right)\sin(3\theta)}\right)^{3/4}\left(1+{k_N}^4-\left(1-{k_N}^4\right)\sin(3\theta)\right)^2} \quad \textbf{A-8}$$

Appendix B: Closed form solution for similarity ratio (b)

In order to solve for the similarity ratio, b, Equation 3.5-8 is expanded via Equations 3.5-1 and 3.5-2 and rearranged into an equation which is quadratic in b, which may be solved by:

$$b = \frac{-B \pm \sqrt{B^2 - 4AC}}{2A} \quad \textbf{B-1}$$

$$A = (I - I_{PC})^2 + \left[\frac{(R-1)(J - J_{PC})}{N}\right]^2 \quad \textbf{B-2}$$

$$B = (I - I_{PC})\left[I_{PC} + I_0\frac{R-2}{R}\right] + (I_{PC} - I_0)(I - I_{PC}) + 2J_{PC}(J - J_{PC})\left(\frac{R-1}{N}\right)^2 \quad \textbf{B-3}$$

$$C = (I_{PC} - I_0)\left[I_{PC} + I_0\frac{R-2}{R}\right] + \left(J_{PC}\frac{R-1}{N}\right)^2 \quad \textbf{B-4}$$

Appendix C: Specific forms for numerical integration of dI_0 and dS

It should be noted that updating the isotropic compression stress (Equation 3.4-10) and sensitivity (Equation 3.4-11) calculated at the end of each solution step requires the numerical integration of these relationships. Following the steps outlined by Herrmann et al. (1987), including approximation of dependent values by the trapezoidal rule, the value of I_0 and S for a given solution step of a drained prediction can be taken as:

<u>If $I > I_l$ and $I_0 > I_l$</u> **C-1**

$$I_{0_m} = \left[I_{0_{m-1}} + \frac{a}{b}\right] exp(b) - \frac{a}{b}$$

$$S_m = \left[S_{m-1} + \frac{c}{d}\right] exp(d) - \frac{c}{d}$$

$$a = \frac{-\lambda_u(1+e_{in})}{\lambda_u - \kappa_s}\left\{\delta I_{m-1}\Delta\varepsilon_{v_m} - \frac{\delta(\Delta I_m)^2}{12}\left(\frac{1}{K_{m-1}} + \frac{1}{K_m}\right) + 3\sqrt{3}\pi J_{m-1}\Delta\varepsilon_{s_m} - \frac{3}{2}\frac{\pi(\Delta J_m)^2}{G} - \sqrt{\left[\frac{\delta I_{m-1}\Delta\varepsilon_{v_m}}{2}\left(\frac{1}{S_{m-1}} + \frac{1}{S_m}\right) - \frac{\delta(\Delta I_m)^2}{12S_{m-1}}\left(\frac{1}{K_{m-1}} + \frac{1}{K_m}\right)\right]^2 + \left[\frac{3\sqrt{3}\pi N I_{m-1}\Delta\varepsilon_{s_m}}{2}\left(\frac{1}{S_{m-1}} + \frac{1}{S_m}\right) - \frac{3\pi N I_{m-1}}{GS_{m-1}}\Delta J_m\right]^2}\right\}$$

$$b = \left\{\frac{1+e_{in}}{\lambda_u - \kappa_s}\left[\Delta\varepsilon_{v_m} - \frac{1}{6}\left(\frac{1}{K_{m-1}} + \frac{1}{K_m}\right)\Delta I_m\right]\right\}$$

$$c = \frac{1+e_{in}}{I_{0_{m-1}}}\left\{\sqrt{\left[\delta I_{m-1}\Delta\varepsilon_{v_m} - \frac{\delta(\Delta I_m)^2}{12}\left(\frac{1}{K_{m-1}} + \frac{1}{K_m}\right)\right]^2 + \left[3\sqrt{3}\pi N I_{m-1}\Delta\varepsilon_{s_m} - \frac{3\pi N I_{m-1}}{G}\Delta J_m\right]^2}\right\}$$

$$d = \frac{-(1+e_{in})}{I_{0_{m-1}}}\left\{\delta I_{m-1}\Delta\varepsilon_{v_m} - \frac{\delta(\Delta I_m)^2}{12}\left(\frac{1}{K_{m-1}} + \frac{1}{K_m}\right) + 3\sqrt{3}\pi J_{m-1}\Delta\varepsilon_{s_m} - \frac{3\pi(\Delta J_m)^2}{2G}\right\}$$

<u>If $I > I_l$ and $I_0 \leq I_l$</u> **C-2**

$$I_{0_m} = I_{0_{m-1}} + a$$

$$S_m = \left[S_{m-1} + \frac{c}{d}\right] exp(d) - \frac{c}{d}$$

$$a = \frac{-\lambda_u(1+e_{in})}{\lambda_u-\kappa_s}\Bigg\{\delta I_{m-1}\Delta\varepsilon_{v_m} - \frac{\delta(\Delta I_m)^2}{12}\left(\frac{1}{K_{m-1}}+\frac{1}{K_m}\right) + 3\sqrt{3}\pi J_{m-1}\Delta\varepsilon_{s_m} - \frac{3}{2}\frac{\pi(\Delta J_m)^2}{G} -$$

$$\sqrt{\begin{matrix}\left[\frac{\delta I_{m-1}\Delta\varepsilon_{v_m}}{2}\left(\frac{1}{S_{m-1}}+\frac{1}{S_m}\right) - \frac{\delta(\Delta I_m)^2}{12S_{m-1}}\left(\frac{1}{K_{m-1}}+\frac{1}{K_m}\right)\right]^2 + \\ \left[\frac{3\sqrt{3}\pi N I_{m-1}\Delta\varepsilon_{s_m}}{2}\left(\frac{1}{S_{m-1}}+\frac{1}{S_m}\right) - \frac{3\pi N I_{m-1}}{GS_{m-1}}\Delta J_m\right]^2\end{matrix}}\Bigg\} + \frac{(1+e_{in})}{\lambda_u-\kappa_s}\left[\Delta\varepsilon_{v_m} - \frac{1}{6}\left(\frac{1}{K_{m-1}}+\frac{1}{K_m}\right)\Delta I_m\right] \times I_l$$

$$c = \frac{(1+e_{in})}{I_l}\left\{\sqrt{\begin{matrix}\left[\delta I_{m-1}\Delta\varepsilon_{v_m} - \frac{\delta(\Delta I_m)^2}{12}\left(\frac{1}{K_{m-1}}+\frac{1}{K_m}\right)\right]^2 + \\ \left[3\sqrt{3}\pi N I_{m-1}\Delta\varepsilon_{s_m} - \frac{3\pi N I_{m-1}}{G}\Delta J_m\right]^2\end{matrix}}\right\}$$

$$d = \frac{-(1+e_{in})}{I_l}\left\{\delta I_{m-1}\Delta\varepsilon_{v_m} - \frac{\delta(\Delta I_m)^2}{12}\left(\frac{1}{K_{m-1}}+\frac{1}{K_m}\right) + 3\sqrt{3}\pi J_{m-1}\Delta\varepsilon_{s_m} - \frac{3\pi(\Delta J_m)^2}{2G}\right\}$$

<u>If $I \le I_l$ and $I_0 > I_l$</u> **C-3**

$$I_{0_m} = \left[I_{0_{m-1}} + \frac{a}{b}\right] exp(b) - \frac{a}{b}$$

$$S_m = \left[S_{m-1} + \frac{c}{d}\right]\ exp(d) - \frac{c}{d}$$

$$a = \frac{-\lambda_u(1+e_{in})}{\lambda_u-\kappa_s}\Bigg\{\delta I_l\Delta\varepsilon_{v_m} - \frac{\delta I_l}{6}\left(\frac{1}{K_{m-1}}+\frac{1}{K_m}\right)\Delta I_m + 3\sqrt{3}\pi J_{m-1}\Delta\varepsilon_{s_m} - \frac{3}{2}\frac{\pi(\Delta J_m)^2}{G} -$$

$$\sqrt{\begin{matrix}\left[\frac{\delta I_l\Delta\varepsilon_{v_m}}{2}\left(\frac{1}{S_{m-1}}+\frac{1}{S_m}\right) - \frac{\delta I_l}{6S_{m-1}}\left(\frac{1}{K_{m-1}}+\frac{1}{K_m}\right)\Delta I_m\right]^2 + \\ \left[\frac{3\sqrt{3}\pi N I_l\Delta\varepsilon_{s_m}}{2}\left(\frac{1}{S_{m-1}}+\frac{1}{S_m}\right) - \frac{3\pi N I_l}{GS_{m-1}}\Delta J_m\right]^2\end{matrix}}\Bigg\}$$

$$b = \left\{\frac{1+e_{in}}{\lambda_u-\kappa_s}\left[\Delta\varepsilon_{v_m} - \frac{1}{6}\left(\frac{1}{K_{m-1}}+\frac{1}{K_m}\right)\Delta I_m\right]\right\}$$

$$c = \frac{-(1+e_{in})}{I_{0_{m-1}}}\left\{\sqrt{\begin{matrix}\left[\delta I_l\Delta\varepsilon_{v_m} - \frac{\delta I_l}{6}\left(\frac{1}{K_{m-1}}+\frac{1}{K_m}\right)\Delta I_m\right]^2 + \\ \left[3\sqrt{3}\pi N I_l\Delta\varepsilon_{s_m} - \frac{3\pi N I_l}{G}\Delta J_m\right]^2\end{matrix}}\right\}$$

$$d = \frac{-(1+e_{in})}{I_{0_{m-1}}}\left\{\delta I_l\Delta\varepsilon_{v_m} - \frac{\delta I_l}{6}\left(\frac{1}{K_{m-1}}+\frac{1}{K_m}\right)\Delta I_m + 3\sqrt{3}\pi J_{m-1}\Delta\varepsilon_{s_m} - \frac{3\pi(\Delta J_m)^2}{2G}\right\}$$

<u>If $I \le I_l$ and $I_0 \le I_l$</u> **C-4**

$$I_{0_m} = I_{0_{m-1}} + a$$

$$S_m = \left[S_{m-1} + \frac{c}{d}\right]\ exp(d) - \frac{c}{d}$$

$$a = \frac{-\lambda_u(1+e_{in})}{\lambda_u - \kappa_s}\left\{\delta I_l \Delta\varepsilon_{v_m} - \frac{\delta I_l}{6}\left(\frac{1}{K_{m-1}} + \frac{1}{K_m}\right)\Delta I_m + 3\sqrt{3}\pi J_{m-1}\Delta\varepsilon_{s_m} - \frac{3}{2}\frac{\pi(\Delta J_m)^2}{G} - \right.$$

$$\left.\sqrt{\begin{matrix}\left[\frac{\delta I_l \Delta\varepsilon_{v_m}}{2}\left(\frac{1}{S_{m-1}} + \frac{1}{S_m}\right) - \frac{\delta I_l}{6S_{m-1}}\left(\frac{1}{K_{m-1}} + \frac{1}{K_m}\right)\Delta I_m\right]^2 + \\ \left[\frac{3\sqrt{3}\pi N I_l \Delta\varepsilon_{s_m}}{2}\left(\frac{1}{S_{m-1}} + \frac{1}{S_m}\right) - \frac{3\pi N I_l}{G S_{m-1}}\Delta J_m\right]^2\end{matrix}}\right\} + \frac{(1+e_{in})}{\lambda_u - \kappa_s}\left[I_l \Delta\varepsilon_{v_m} - \frac{I_l}{6}\left(\frac{1}{K_{m-1}} + \frac{1}{K_m}\right)\Delta I_m\right]$$

$$c = (1+e_{in})\left\{\sqrt{\begin{matrix}\left[\delta\Delta\varepsilon_{v_m} - \frac{\delta\Delta I_m}{6}\left(\frac{1}{K_{m-1}} + \frac{1}{K_m}\right)\right]^2 + \\ \left[3\sqrt{3}\pi N\Delta\varepsilon_{s_m} - \frac{3\pi N}{G}\Delta J_m\right]^2\end{matrix}}\right\}$$

$$d = -(1+e_{in})\left\{\delta\Delta\varepsilon_{v_m} - \frac{\delta\Delta I_m}{6}\left(\frac{1}{K_{m-1}} + \frac{1}{K_m}\right) + \frac{3\sqrt{3}\pi J_{m-1}}{I_l}\Delta\varepsilon_{s_m} - \frac{3\pi(\Delta J_m)^2}{2GI_l}\right\}$$

where the subscripts m and m-1 denote values associated with the current and previous solution steps, respectively. It should be noted that that $(\Delta I_m)^2$ and $(\Delta J_m)^2$ are quick notations for the following equivalencies:

$$(\Delta I_m)^2 = {I_m}^2 - {I_{m-1}}^2 \qquad \textbf{C-5}$$

$$(\Delta J_m)^2 = {J_m}^2 - {J_{m-1}}^2 \qquad \textbf{C-6}$$